UNIVERSITY OF SOUTHAMPTON

FACULTY OF ENGINEERING AND THE ENVIRONMENT

Institute of Sound and Vibration Research

HIGH-FREQUENCY SOUND TRANSMISSION IN FLOW DUCTS

by

Oliviero Olivieri

Thesis for the degree of Master of Philosophy

21 January 2017

UNIVERSITY OF SOUTHAMPTON

ABSTRACT

FACULTY OF ENGINEERING AND THE ENVIRONMENT

Master of Philosophy Thesis

HIGH-FREQUENCY SOUND TRANSMISSION IN FLOW DUCTS

Oliviero Olivieri

This dissertation considers sound transmission in axisymmetric, uniformly-lined ducts of constant cross-section, carrying a high speed, subsonic, parallel mean shear flow. Fast and efficient numerical and analytical methods that can be used with high-frequency sound are developed.

This is fundamentally theoretical work, but with a view to the specific engineering application of acoustic liner optimization in turbofan aero-engine ducts, as cylindrical and annular ducts are approximate models of inlet and bypass ducts, respectively. Focus has been given on applying those methods to problems for which the noise source, mean flow and duct geometry are representative of the turbofan aero-engine application.

A new numerical procedure to calculate the small-amplitude pressure perturbation in the frequency domain with arbitrary mean velocity profiles is developed and a computer code is implemented. The method is a problem-specific finite element solver which, owing to the axisymmetric geometry, enables the rapid computation of a large number of modes at very high frequencies (e.g., several harmonics of the fan's blade passing frequency) at a modest computational cost. Because of its speed and accuracy, it may be suitable for application in practical design optimisation procedures for acoustic linings.

Examples of finite element solutions of the eigenvalue problem in cylindrical and annular ducts are provided and results, which show how the shape of the boundary-layer profile can affect the modal structure of the in-duct pressure perturbation field are presented.

In the special case of uniform core flow and thin boundary layers at duct walls, finite element solutions are compared with those obtained from an approximate perturbation method based on an asymptotic inner expansion valid in the boundary layer.

An investigation of the effect of boundary-layer shielding on high-frequency sound transmission is carried out. A new cost function, which provides a quantifiable measure of an acoustic liner's performance for a multi-mode noise source is proposed.

Contents

List of Tables

List of Figures

UNIVERSITY OF
Southampton

Academic Thesis: Declaration Of Authorship

I, OLIVIERO OLIVIERI, declare that this thesis and the work presented in it are my own and has been generated by me as the result of my own original research.

HIGH-FREQUENCY SOUND TRANSMISSION IN FLOW DUCTS

I confirm that:

1. This work was done wholly or mainly while in candidature for a research degree at this University;
2. Where any part of this thesis has previously been submitted for a degree or any other qualification at this University or any other institution, this has been clearly stated;
3. Where I have consulted the published work of others, this is always clearly attributed;
4. Where I have quoted from the work of others, the source is always given. With the exception of such quotations, this thesis is entirely my own work;
5. I have acknowledged all main sources of help;
6. Where the thesis is based on work done by myself jointly with others, I have made clear exactly what was done by others and what I have contributed myself;
7. Parts of this work have been published as:

Olivieri, O., McAlpine, A., & Astley, R. J. (2009). Numerical calculation of pressure modes at high frequencies in lined ducts with a shear flow. In *EURONOISE 2009* Edinburgh, UK.

Olivieri, O., McAlpine, A., & Astley, R. J. (2010). Determining the pressure modes at high frequencies in lined ducts with a shear flow. In *16th AIAA/CEAS Aeroacoustics Conference* Stockholm, Sweden.

Signed: ………………………………………………………………………….

Date: ………………………………………………………………………….

Acknowledgements

I gratefully acknowledge the financial support from the Engineering and Physical Sciences Research Council (EPSRC), which made possible my studies.

I would like to express my gratitude to my supervisors, Dr. Alan McAlpine and Prof. Jeremy Astley, for their support throughout my studies. The frequent technical discussions we had were insightful and greatly appreciated.

My studies and the writing of this dissertation would not have been possible without the continued support, from start to finish, encouragement, love and understanding of my wife. A huge thank you to her.

Even though my children are still too young to read this, I would like to say thank you to them for their patience and unconditional love. I want them to know that they have been my motivation to complete this work.

List of Symbols

Dimensional quantities

$\tilde{a}$	outer duct radius (m)
$\tilde{C}$	isentropic local speed of sound (m/s), $\tilde{C} = \sqrt{\gamma\, R\, \tilde{T}}$
c_0	reference speed of sound (m/s)
c_p	specific heat at constant pressure (J / kg K)
c_v	specific heat at constant volume (J / kg K)
$\tilde{d}$	lining thickness (m)
$\tilde{e}$	specific internal energy (m^2/s^2)
$\tilde{f}$	frequency (s^{-1}), $\tilde{f} = \tilde{\omega}/2\pi$
$\tilde{k}$	free field acoustic wave number (rad m^{-1})
k_B	Boltzmann constant, $k_B = 1.380\,648 \cdot 10^{-23}$ (J / K)
$\tilde{M}$	molar mass, (kg/mol)
N_A	Avogadro number, $N_A = 6.022\,140 \cdot 10^{23}$ (mol^{-1})
$\tilde{p}$	pressure field (N/m^2)
p_0	reference pressure (N/m^2), $p_0 = \rho_0\, c_0^2/\gamma$
$\tilde{R}(\tilde{\omega})$	surface specific acoustic resistance ((kg/m^3) (m/s)), $\tilde{R} = \mathrm{Re}(\,\tilde{Z}\,)$
$\tilde{b}$	inner duct radius (m)
$\tilde{s}$	specific entropy (m^2/s^{2}K)
$\tilde{T}$	absolute temperature (K)

$\tilde{t}$	time (s)
R	specific gas constant, $R = k_B N_A / \tilde{M}$
$\tilde{\boldsymbol{u}}$	fluid velocity vector field (m/s)
$\tilde{Z}(\tilde{\omega})$	surface specific acoustic impedance ((kg/m^3) (m/s)), $\tilde{Z} = \tilde{R} + \mathrm{j}\,\tilde{X}$

Greek symbols

$\tilde{\rho}$	density field (kg/m^3)
ρ_0	reference density (kg/m^3)
$\tilde{X}(\tilde{\omega})$	surface specific acoustic reactance ((kg/m^3) (m/s)), $\tilde{X} = \mathrm{Im}(\,\tilde{Z}\,)$
$\tilde{\omega}$	angular frequency (rad s^{-1}), $\tilde{\omega} = 2\pi \tilde{f}$

Dimensionless quantities

$A(\eta)$	surface specific acoustic admittance, $A = \dfrac{1}{Z}$
B	number of rotor blades
C	isentropic local speed of sound, $C = \dfrac{\tilde{C}}{c_0}$
$D(\boldsymbol{x})$	mean density field, density field of steady background flow
d	lining thickness, $d = \dfrac{\tilde{d}}{\tilde{a}}$
h	hub-to-tip ratio, $h = \dfrac{\tilde{b}}{\tilde{a}}$
I	sound intensity
k_z	(complex-valued) axial wave number, $k_z = \lambda\,\eta$
L	distance between two axial points in units of duct radius
$\boldsymbol{M}(\boldsymbol{x})$	mean flow velocity vector field
M	axial mean velocity
M_0	(constant) axial mean velocity (case of uniform mean flows)
$P(\boldsymbol{x})$	mean pressure field, pressure field of steady background flow
$p(\boldsymbol{x}, t)$	(unsteady) pressure field, $p = \dfrac{\tilde{p}}{\rho_0 c_0^2}$
$p'(\boldsymbol{x}, t)$	pressure perturbation field, $p' = p - P$

$\hat{p}(\boldsymbol{x};\eta)$	complex amplitude of pressure perturbation, Fourier transform of $p^{'}(\boldsymbol{x},t)$
θ	azimuthal angle in a circular cylindrical coordinate system
r	radial coordinate in a circular cylindrical coordinate system, or transverse coordinate in a general cylindrical coordinate system
$R(\eta)$	ratio of the specific acoustic resistance of the surface to the characteristic impedance of the medium, $R = \tilde{R}/\rho_0\, c_0$
t	time, $t = \dfrac{\tilde{t}}{\tilde{a}/c_0}$
$\boldsymbol{u}$	fluid velocity vector field, $\boldsymbol{u} = \dfrac{\tilde{\boldsymbol{u}}}{c_0}$
$\boldsymbol{u}'$	fluid velocity perturbation, $\boldsymbol{u}' = \boldsymbol{u} - \boldsymbol{M}$
$\hat{\boldsymbol{u}}(\boldsymbol{x};\eta)$	complex amplitude of velocity perturbation, Fourier transform of $\boldsymbol{u}^{'}(\boldsymbol{x},t)$
V	number of stator vanes
(x,y,z)	Cartesian coordinate system
$\boldsymbol{x}_\perp$	position vector in the transverse plane
$\boldsymbol{e}_z$	unit vector in the axial direction
$Z(\eta)$	ratio of the specific acoustic impedance of the surface to the characteristic impedance of the medium, $Z = \tilde{Z}/\rho_0\, c_0$

Greek symbols

γ	ratio of specific heats (constant), $\gamma = c_p/c_v$
δ	boundary layer thickness
η	Helmholtz number (dimensionless frequency), $\eta = \tilde{k}\,\tilde{a} = \dfrac{\tilde{\omega}\tilde{a}}{c_0}$
κ	(complex-valued) radial wave number, $\kappa = \lvert\kappa\rvert e^{\mathrm{j}\,\varphi}$
λ	eigenvalue, $\lambda = \dfrac{k_z}{\eta}$
λ_{aco}	acoustic wavelength, $\lambda = \dfrac{2\pi}{\eta}$
$\rho(\boldsymbol{x},t)$	density field, $\rho = \dfrac{\tilde{\rho}}{\rho_0}$
$\rho'(\boldsymbol{x},t)$	density perturbation field, $\rho' = \rho - D$

$X(\eta)$	ratio of the specific acoustic reactance of the surface to the characteristic impedance of the medium, $X = \tilde{X}/\rho_0\, c_0$
$\psi(r)$	radial pressure perturbation mode shape
$\Psi(r, \theta)$	transverse pressure perturbation mode shape

Subscripts

I	indicates an interpolant function
(m, n)	mode (m, n)
m	azimuthal mode number
n	radial mode number

Superscripts

$^+$	denotes a mode propagating in the positive direction, which, in this study, corresponds to downstream direction
$^-$	denotes a mode propagating in the direction of decreasing z, which, in this study, corresponds to upstream direction
(aco)	refers to the component of a perturbation variable carried by the acoustic mode
(ent)	refers to the component of a perturbation variable carried by the entropic mode
(vor)	refers to the component of a perturbation variable carried by the vortical mode

Finite element method notation

ϕ_i	global basis functions or one-dimensional global basis functions
ϕ_i^e	local basis functions
Φ_i	two-dimensional global basis functions
h	mesh size
$\mathbf{K}$	stiffness matrix
$\mathbf{K}^{(m)}$	Mach-weighted stiffness matrix
$\mathbf{M}$	mass matrix
$\mathbf{M}^{(m)}$	Mach-weighted mass matrix

$n(e,j)$	global-to-local index (that is, global label of the j-th node of the e-th element)
N_e	number of elements
N_{en}	number of element nodes
N_{glob}	number of global degrees of freedom (that is, total number of nodes)
p	polynomial degree
$\mathbf{S}$	shear coupling matrix
$\mathcal{T}$	mesh
$\mathbf{Z}$	boundary impedance matrix
$\mathbf{Z}^{(m)}$	Mach-weighted boundary impedance matrix

Mathematical symbols

*	complex conjugation
δ_{ij}	the Kronecker symbol: $\delta_{ij} = 0$ for $i \neq j$ and $\delta_{ii} = 1$
$(\boldsymbol{a} \cdot \nabla)$	Rate of change in the direction of $\boldsymbol{a}$. $\boldsymbol{a} \cdot \nabla = a_x \frac{\partial}{\partial x} + a_y \frac{\partial}{\partial y} + a_z \frac{\partial}{\partial z}$
$\mathbb{C}$	the complex numbers
$\mathcal{C}^2$	the space of twice continuously differentiable functions
$\frac{D}{Dt}$	Convective differentiation operator
H^1	Sobolev space H^1 of L^2-functions whose first derivatives in the sense of distributions are also in L^2.
j	imaginary number, $\sqrt{-1}$
J_m	Bessel function of the first kind, order m
L^2	the space of square integrable functions
$\mathbb{N}$	the set of positive integers
∇^2	Laplacian operator
$\nabla^2_\perp$	Laplacian operator in the transverse plane
$\nabla\cdot$	Divergence operator

$\nabla_\perp$	gradient operator in the transverse plane
$\mathcal{P}_p^d$	the space of d-dimensional polynomial functions of order p
S_h^p	the space of d-dimensional polynomial functions of order p
$\mathbb{R}$	the real numbers
Y_m	Bessel function of the second kind, order m

Other symbols

$\hat{}$	indicates Fourier transform of a variable
$'$	indicates a perturbation variable. It denotes a derivative in chapter 4.
$\tilde{}$	indicates a dimensional variable (with the exception of reference constants such as ρ_0, p_0 and c_0 in order not to make the notation too heavy)

Abbreviations and acronyms

ACARE	Advisory Council for Aviation Research and innovation in Europe
BPF	blade passing frequency
DNS	direct numerical simulation
FEM	finite element method
EPNdB	Effective Perceived Noise level in decibels
ICAO	International Civil Aviation Organisation

Chapter 1

Introduction

1.1 Background

This dissertation considers sound transmission in axisymmetric, uniformly-lined ducts of constant cross-section, carrying a high speed, subsonic, parallel mean shear flow.

This is fundamentally theoretical work, but with a view to the specific engineering application of acoustic liner optimization in turbofan aero-engine ducts, as cylindrical and annular ducts are approximate models of inlet and bypass ducts, respectively. Focus has been given on applying numerical and analytical methods to problems for which the noise source, mean flow and duct geometry are representative of the turbofan aero-engine application.

This field of study has received much attention over the course of last 50 years or so. Since early years, new theoretical findings and the development of both analytical and numerical methodologies has progressed steadily and remarkable advances have been made. Many novel contributions continue to appear annually in scientific and technical journal papers and conference proceedings.

1.1.1 Practical applications

Historically, a great deal of research efforts has been focused on the practical application of noise prediction and control of aircraft turbo-jet and turbo-fan engines. That is clearly demonstrated by the vast amount of scientific and technical literature, which has been published in the 70's and 80's on the subject [1]. However, the study pertains to a very wide range of engineering applications. In addition to ducted turbo-machinery, of which aircraft turbo engines are a particular case, other prominent applications are, ventilation & air-conditioning (HVAC) systems and automotive intake and exhaust systems [83, 44, 15, 59].

For all these applications, a moving air flow is constrained in ducts, whose surfaces in contact with the fluid can be lined with appropriate acoustic absorbing materials to reduce the noise. The passive acoustic treatment of the internal noise path is, in fact, a standard technique to achieve noise reduction objectives. Predicting reliably the efficiency of acoustic treatments depend on the understanding of the interaction of the sound field with the lining material and a non-uniform mean velocity profile.

Furthermore, applications extend to the analysis and control of aerodynamically induced blade vibrations (both flutter and forced vibrations) in ducted turbo-machinery used as propulsion such as aero-engines or for electricity generation such as steam turbines. Periodic fluctuating forces on cascade blades with frequencies close to the structural natural frequencies of the system can lead to stability problems, create durability issues or even cause fatigue failure [121, 122, 50, 78, 97].

1.1.2 Numerical simulation

With the incredible progress of computer memory and calculation capability, numerical simulations now make it possible to find approximate solutions to mathematical models that cannot be solved analytically. It has become an irreplaceable tool in science and

---

[1] Review articles by Nayfeh et al. [91] and Eversman [38] offer a comprehensive and systematic review on aero-engine duct acoustics, updated to 1975 and 1991, respectively.

engineering, creating a bridge between theoretical and experimental work. Calculations through numerical models are often referred to as *numerical experiments*.

Some of the main advantages of adopting simulation in engineering are:

- reducing to a minimum the need for running expensive tests on physical prototypes;
- quickly focussing on promising product design alternatives at the very start of the development process through numerical experiments, which can easily be modified with a large number of parameter variations.

The aerospace industry has been adopting computational tools for quite some time throughout the entire product life cycle from design and validation process to manufacturing and product support. Testing has become an aid to the development and validation of the models, which are applied at the very early stage of the design of new products or product variants.

More recently, other industries, i.e., the automotive and the energy sectors, under legislative and competitive pressures to develop innovative designs faster are also turning to computational simulations to implement rapid, high-quality and cost-effective product development processes.

Defining a correct mathematical model is critical. As the initial product design relies on simulations and later design modification at a late stage of development may not be done or can be prohibitively expensive, it is evident how crucial the choice of a suitable model is.

1.1.3 Underlying theoretical models

In the case of the subject of interest of this dissertation, numerical simulations open new possibilities in the understanding of sound propagation and its interaction with mean flow and surfaces lined with acoustically-absorbent material. Clearly, the quality of a computer simulation can only be as good as the quality of the model, and simulations must be validated against experimental data.

A direct numerical simulation (DNS) approach could potentially solve the problem from first-principles with little need of developing underlying theoretical models, but it is a technique still prohibitively expensive in terms of computational cost. Also, often numerical simulations based on theoretical models (when appropriately validated) may provide a better insight of the physical phenomenon.

The general purpose of this work was to develop fast and efficient numerical and analytical methods that could be practical for use, for example, by the aerospace industry. This requires specific choices on the underlying model to be made, which will be discussed in this dissertation.

1.1.4 Aircraft noise

Aircraft noise control is a very critical technical issue for the aerospace industry. Because of the incredible expansion of civil aviation, noise at take-off and landing is a major cause of adverse community reaction to the operation and further expansion of airport capacity, and it is potentially a limiting factor in the growth of future air traffic.

Designing significantly quieter aircraft is necessary if the aerospace industry is to enable sustained growth while limiting the environmental impact, and respond to strong environmental opposition to building new airports and runways. As a matter of fact, tougher noise legislations and self-imposed goals by the industry are on the way (see paragraph below).

Historically, jet noise was the dominant source of noise in older engine designs (turbojets and low bypass ratio turbofan engines) due to the high jet velocities. One of the results of the continuing search for higher performance propulsion systems was the development of ultra high bypass turbofan engines.

In modern high-bypass and ultra high-bypass ratio aero-engines[2], most of the thrust is produced by the air bypassed around the core. This has allowed significantly lower jet velocities for the same thrust, resulting in much less jet exhaust noise, thus leaving the fan stage and first compressor stage as the primary engine noise source and hence as the primary target for noise control. Noise, which has high-frequency content, propagates in the intake and bypass ducts. The use of appropriate acoustic linings can effectively attenuate noise inside a duct before it reaches a termination and radiates into the free field.

Passive noise control by using acoustic liners is one of the main strategies to reduce fan noise emissions from a turbofan engine. In general, sound absorption depends on the properties of the acoustic liners, but at high frequencies, sound can be refracted towards or away from the lined duct walls: this depends on the direction of propagation of the sound relative to the mean flow.

In order to have an effective noise control in duct systems, it is crucial to gain a thorough understanding of the physics, in particular the interaction of the perturbed flow with the mean flow and the acoustic liners in order to build effectively models which can guide the design of liners.

A note on key noise regulations It should be said at the outset that this brief paragraph is not meant to give a comprehensive overview of complex legislation matters in regards to aircraft noise, but it aims simply to highlight some of the key regulations that have been leading the aerospace industry to large research investments and efforts to mitigate the effects of aircraft noise.

The International Civil Aviation Organisation (ICAO), a specialized agency of the United Nations which provides standards, recommended practices and policies for civil aviation [3], introduced its first aircraft noise regulations back in 1971. Following that, the

---

[2] These large engines have bypass ratios in the range of 10:1 to 15:1, compared to 4:1 to 6:1 for the earlier turbofan engine [118].

[3] The 191 members of ICAO are representatives of the government and industries of all states of the United Nations. ICAO regulations are done by consensus and become binding on the member states.

aircraft industry embraced major research in a number of technologies for noise mitigation. The optimisation of duct acoustic liners was recognised as one of the key research areas. It was realised the importance of developing theoretically-based models not only to interpret and correlate test data, but also to assess the potential of hypothetical design features and to guide the design of liners. [116]

Noise regulations are embedded into the Annex 16, vol. 1 of the Convention on International Civil Aviation [96], a document which established the organisation. Aircrafts are classified in 13 Chapters according to their year of design, type and weight. For each type and for each corresponding weight, a maximum EPNdB noise emission level is defined. Currently, Chapter 3 requirements are imposed to any fleet, and more restrictive noise limits, which took effect from 2006, are imposed to aircrafts with high-bypass ratio engines through Chapter 4. In 2001, the organisation endorsed the balanced approach principle to aircraft noise management[4] [], which includes, among others, operating restrictions and reduction of aircraft noise at source, however, favouring the latter to encourage the operation of the quietest fleet possible.

In March 2014, the ICAO Council meeting has adopted the amendments to Annex 16. The amendments include a new noise standard for jet and propeller-driven aircrafts (Chapter 14) and impose further 7 EPNdB below the previous limit [53]. Requirements applies to newly-designed high-weight aircraft entering service from 2017 and for lower weight aircraft entering service from 2020.

Moreover, in 2000 The Advisory Council for Aviation Research and innovation in Europe (ACARE), an initiative aiming to provide a network for strategic research in aeronautics and air transport in the European Union, set a goal for EU research to reduce the EPNdB of new aircrafts by 10 dB by 2020 relative to best practice in 2000. A similar goal was declared by NASA [101].

---

[4] Appendix C of Assembly Resolution A36-22

1.2 Literature review

This section is intended to provide general background to this study. The advancements of research made in the development of both theoretical models of small-amplitude perturbation [5] propagation in flow ducts and appropriate methods to solve their mathematical equations are reviewed here. In particular, areas of incomplete understanding, which have motivated this work will be highlighted in subsection 1.2.1.7.

Since the introduction of the first aircraft noise regulations, research in this field has been driven by the aerospace industry. It has largely focused on aero-engine duct applications, aiming to develop mathematical models which could be suitable for use in liner optimization studies. It may not be surprising to the reader that most of the literature reviewed here, although of fundamental theoretical nature, considers mean flow approximations and boundary conditions which are typical of aero-engine duct systems.

Although aiming to offer an account of the progress of the investigations in a chronological order, this has not been the primary criterion for the organization of the material. It has been recognized that organizing material in paragraphs, each of which addresses a particular aspect or reflects on the implications of certain model assumptions, could provide a more systematic review.

1.2.1 Small disturbance propagation theory

1.2.1.1 Basic equations

An appropriate starting point to describe the dynamics and thermodynamics of a general viscous, heat-conducting compressible Newtonian fluid would be the following set of equations (cf. [98]).

- The conservation of mass equation

---

[5] In what follows, the term 'small-amplitude perturbation' instead of 'acoustic' is preferred. As it will been explained later, the acoustic, vortical and entropic perturbation modes become coupled in an inhomogeneous mean flow.

- The Navier-Stokes momentum balance[6] equation at thermodynamic quasi- equilibrium[7]
- The energy (per unit mass) balance equation, where the thermodynamic pressure, p, and the absolute temperature, T, may be chosen as independent thermodynamic variables, and the heat flux vector is assumed to obey the *Fourier's law*.

Alternatively, entropy could be used in place of the internal energy applying the fundamental thermodynamic relation

$$\tilde{T}\,\mathrm{d}\tilde{s} = \mathrm{d}\tilde{e} + \tilde{p}\,\mathrm{d}\,(1/\tilde{\rho}) \tag{1.2.1}$$

where s is the entropy per unit mass, e is the internal energy per unit mass and ρ is the fluid density.

In the remainder of this paper, for the sake of simplicity of exposition, we will refer to the set of equations above as the *Navier-Stokes equations,* and to the second equation above as the equation of motion, since it represents the Newton's second law for Newtonian fluids.

From a theoretical point of view, such set of equations, when matched with appropriate source terms and initial and boundary conditions, would describe completely the fluid motion, from its smallest scales (e.g., smallest turbulent eddies) to its largest scales. However, it is very hard to solve these equations under given conditions. No solution to these equations subject to general conditions has been found and the application of the direct numerical simulation (DNS) method, which aims to resolve all scales, including the very smallest ones, has an extremely large computational cost [28].

---

[6] The *Cauchy-Poisson's law* holds as constitutive equation.

[7] The mean of the three normal stresses at a point (often referred to as *mechanical pressure*, [Acheson]) is assumed equivalent to the negative of the thermodynamic pressure, that is pressure maintained by molecular collisions.

1.2.1.2 Linear theory

In order to solve the problem of small amplitude motion, which is of interest in linear acoustics [98], aeroacoustics and computational aeroacoustics (CAA) [115], linear unsteady aerodynamics [121] and here, the so-called *linear theory* is adopted. It is well known that it consists of decomposing the flow field into two different scales: a steady base flow, which can be a steady-state or time-averaged condition, and an unsteady perturbed compressible motion. The key condition is that the amplitude of the perturbed quantities is small enough compared to the corresponding mean flow quantities, so that a linearization procedure to the equations of fluid motion and thermodynamics about an arbitrary steady solution to those equations can be applied.

Any flow quantity $q(\boldsymbol{x}, t)$ is expressed as linear (first-order) perturbation series in a dimensionless parameter$\epsilon \ll 1$

$$q(\boldsymbol{x}, t) = Q(\boldsymbol{x}) \left(1 + \epsilon q'(\boldsymbol{x}, t) + ...\right) \tag{1.2.2}$$

where $\boldsymbol{x}$ is the space coordinate vector, t is time and q' is a dimensionless variable.

Substituting the expressions into the governing equations, subtracting the equations for the steady flow and neglecting the products of fluctuating components, the equations in the perturbed quantities are then obtained. Some of the steady-state quantities $Q(\boldsymbol{x})$ would appear in the linearized equations and must be provided in order to solve them.

1.2.1.3 Splitting the noise problem

Any in-duct propagation of small-amplitude disturbances implies a generation process and eventually radiation from duct terminations. In principle, a complete aero-engine noise prediction strategy would consider all the three main processes, i.e., generation, propagation and radiation to the far field, as a single noise problem, since there would be a certain degree of coupling between the three processes.

With regards to an aero-engine duct system,there are two types of mean flow of interest [97].

1. Flow where the swirl is negligible but the axial flow is radially sheared, as found inside the inlet duct or bypass duct downstream of the guide vanes,
2. Flow which is both radially sheared and contains a significant swirling component, as found in compressor and turbine stages or between the fan and stator.

Typically, due to the variety and complexity of the mechanisms involved, the noise problem has been tackled by dividing it into those three, more manageable parts, both in the case of sheared and swirling mean flow. Once the solutions for the generation, propagation and radiation are obtained, they can be coupled in a sensible manner to produce a complete solution. In this way, the control of noise at the receiver may become an easier task. For example, if the sound power that radiates within a particular sector of the far field has to be reduced and the characteristics of the radiation are understood, the modes that predominantly radiate within that sector can be targeted for control.

However, Atassi [9], investigating the acoustic and unsteady aerodynamic loading of a cascade of loaded blades (a physical phenomenon found, for example, between fan and stator of an aero-engine, where a strong swirling mean flow is present), showed strong interference between the two, which led him to conclude that it was not possible to separate the process of generation from that of propagation.

1.2.1.4 Modal decomposition of the flow field perturbations

If the duct geometry can be approximated by a prismatic shape and the flow field can be considered invariant in the duct axial direction, the study of perturbation propagation can then be reduced to the analysis of *normal modes* of the linearized equations. The small-amplitude disturbances are written as an infinite sum of normal modes.

In order to take advantage of the simplicity and power of normal mode analysis, aeroengine intake and bypass ducts have been commonly simplified to cylindrical and annular shapes, respectively, with uniform cross-section in the axial direction. Moreover, a flow condition, referred to as *fully-developed* flow is typically assumed, which consists of invariant mean flow in the axial direction.

The mathematical problem of perturbation propagation is then that of identifying pattern and propagation characteristics (e.g., dispersion relations) of all upstream- and downstream-travelling modes that could potentially be excited inside the duct by a source. The duct is treated as a multi-mode waveguide of infinite length, as for example in the electric transmission theory, and the problem formulation leads to an eigenvalue problem in two dimensions in the frequency domain. In the case of axisymmetrical cross sections or idealized two-dimensional ducts (two parallel infinite planes), this approach leads to one-dimensional problems, that is the governing equations to be solved are ordinary differential equations.

Then, in order to obtain useful predictions in practical applications, the identified modes would be matched to some fluctuating pressure field, which is specified at some reference plane normal to the duct axis, by using the modes' orthogonality property.

In the case of modelling aircraft turbofan duct systems, normal mode analysis has been widely adopted since the first pioneering works. Analytical and semi-analytical methods can provide fast and efficient simulation techniques, which also often give insight into the physics of the sound propagation and radiation. Numerical techniques can simulate more realistic models, including three-dimensional ducts and complex fluid flows, albeit at high-frequencies the computational cost can be prohibitive.

In a classic paper, Tyler & Sofrin [119] laid the foundation for the contemporary study of duct acoustics based on modal decomposition. They first introduced the concept of spinning pressure patterns in ducts which are generated by rotating sources normal to the duct's axis (e.g., axial flow compressor stage or ducted fan) and provided a mathematical formulation in the case of hard-walled annular ducts without flow. They carried out extensive experimental investigations on the structure of the near sound field generated on a reference plane adjacent to a ducted axial flow compressor and then built a theoretical model. They considered first the case of rotor alone, then a compressor stage. They recognised that two different noise generation mechanisms were in place. In the former case, they observed spinning pressure patterns of azimuthal order either the same or multiples of the number of rotor blades (B), turning with rotor speed and propagating at frequencies of harmonics of the blade passing frequency (BPF). In the latter case, a plurality of spinning pressure patterns was identified corresponding to the BPF and any of its harmonics according to the formula

$$m = nB \pm kV \tag{1.2.3}$$

where B is the number of rotor blades, V the number of stator vanes, n is the n-th harmonics of BPF and k is any positive integer. This is known as rotor-stator interaction noise.

The idea of using Tyler and Sofrin's model of discrete tone noise generation and coupling it with duct modal decomposition in order to estimating sound attenuations was first suggested by Rice [105]. The work proved the usefulness of the modal decomposition approach.

Some years later Rice et al. [107] also presented an interesting way to physically interpreting the modes as the result of the interference of plane waves propagating at an angle to the duct axis and subsequently reflecting from the duct walls.

Matching spinning pressure patterns determined from the formula (above) and an analysis of duct modes, aero engine designers could carefully select the appropriate number of rotor blades and stator vanes such that the discrete tone interaction noise at blade-passing frequencies and higher harmonics could be cut-off (that is, not propagate). A whole family of engines benefited from Tyler and Sofrin's work: the Pratt & Whitney

JT9D [8], the General Electric CF-6 [9], and the Rolls-Royce RB.211 EPA[10][2].”

1.2.1.5 Viscosity

Large Reynolds numbers are encountered in aero-engine duct applications. However, the question of whether viscosity is small enough to be neglected can only be settled in relation to a specific problem. A notorious example of this statement is the *boundary layer*, which is briefly explained here below.

It is an experimental fact that a Newtonian fluid adheres to a wall - this is the so-called *no-slip* boundary condition. If it is imposed at a solid surface, in a thin region near the wall, the fluid velocity changes rapidly from zero at the wall to its value in the free stream which leads to significant velocity gradients. In that region, referred to as the boundary layer[11], however small is the coefficient of viscosity of the fluid, the flow velocity develops such strong gradients that the effect of the viscous term in the motion equation becomes important and cannot be neglected.

Implications on the equations of motion In an early study on the effect of nonuniform flow in ducts on the acoustic wave propagation Nayfeh [89], introduced the following distinctions with respect to the way the effects of viscosity could be take into account to carry out the analysis.

1. Neglect viscosity in both the mean flow equations and the equations in the perturbed quantities;
2. Include viscosity in the mean flow equations only;
3. Include viscosity in both sets of equations.

---

[8] Pratt & Whitney’s first high-bypass-ratio turbofan.

[9] The high bypass of the General Electric CF6 represented a historic breakthrough in fuel efficiency

[10] High bypass engine subsequently developed into the Rolls-Royce Trent family of engines

[11] The role of viscosity in the boundary layer and the definition of the boundary layer concept, is attributed primarily to Prandtl [93].

We recover these distinctions because they are useful to organise the material in the remainder of this subsection.

Case 1: inviscid mean flow and disturbances If neglecting viscosity and heat conduction at the outset, the Navier-Stokes equations reduce to the Euler equations. Moreover, the mass conservation equation and the Euler momentum equation become decoupled from the energy (or entropy) equation, which in turn can be omitted from the coupled system of equations.

Moreover, if non-equilibrium processes (e.g., combustion) are not taking place, the entropy of a material particle remains constant in time, i.e.,

$$\frac{D\tilde{s}}{D\tilde{t}} = 0 \tag{1.2.4}$$

When $\tilde{s}$ = const. or $\frac{\partial \tilde{p}}{\partial \tilde{s}} = 0$ the isentropic thermodynamic constitutive relation, which relates pressure with density

$$\tilde{p} = \tilde{p}(\tilde{\rho}) \tag{1.2.5}$$

can be used instead of the energy (or entropy) equation.

Assuming a unidirectional uniform mean velocity field parallel to the duct axis and applying the linearization process mentioned above yields the *convective wave equation* (see, for example, [111]). In a similar way, assuming a unidirectional shear mean velocity field of arbitrary profile, after some manipulations (see section 2.4), yields the *Pridmore-Brown equation*[12] (cf. [45]).

The assumption of zero viscosity used in this derivation of the Pridmore-Brown equation may seem inconsistent with the fact that, in a duct, the Pridmore-Brown equation is used in conjunction with a mean flow profile exhibiting shear layers at the duct walls. This issue will be addressed in the next paragraph.

---

[12] The equation has been named after Pridmore-Brown, who obtained it first in a seminal paper [104] for the particular case of a two-dimensional duct (that is, parallel planes). The equation in cylindrical coordinates was obtained by [81].

The convective wave equation is essentially a wave equation in new coordinates (cf. [12]). The Pridmore-Brown equation has variable coefficients that depend upon the underlying mean flow. A closed-form, exact solution has not yet been found.

Goldstein [45]showed that the Pridmore-Brown equation is a special form of the Landahl-Lilley's third-order wave equation [13] when it is linearized about a unidirectional transversely sheared mean flow, rearranged to exhibit a source term on the right-hand side and then removed, and considering pressure fluctuations $p' \ll p_0$ small relative to the mean pressure p_0 so that the term ln $\left(\frac{p'}{p_0}+1\right)$ can be approximated by$\frac{p'}{p_0}$.

Case 2: viscous mean flow and inviscid disturbances This assumption was adopted both by Mungur & Gladwell [81] and Nayfeh et al. [91] in their derivation of the Pridmore-Brown equation. Starting from the Navier-Stokes equations, they applied a linearization procedure around the mean flow, in which viscosity and thermal conductivity, among the other flow quantities, were decomposed in first-order perturbation series (steady mean flow quantity and small unsteady perturbation).

After those expressions had been substituted into the governing equations, the equations for the steady flow were subtracted. Those equations exhibited the steady coefficients of viscosity and thermal conductivity. On the contrary, in the resulting equations in the perturbed quantities, the steady and unsteady coefficients of viscosity and thermal conductivity were set to zero.

What this assumptions' choice tells us is that, even though the perturbed quantities obey inviscid and non-heat conducting equations and, therefore, the inviscid and non-heat conducting boundary conditions are to be used, the underlying mean flow, which has been modelled as viscous and heat conducting, can sustain a shear flow, giving rise to boundary layers.

---

[13] Lilley's third-order wave equation is obtained rearranging the Navier-Stokes equations into the form of an inhomogeneous convective, or moving medium, wave equation rather than the inhomogeneous stationary medium wave equation originally proposed by Lighthill.

The action of viscosity on the perturbation propagation can, in this case, be considered "indirect": the viscosity-generated shear flow has refractive effects on the perturbation propagation.

These assumptions are made, more or less implicitly, in numerous papers from early works to recent (for example, [39], [117], [125]),

Case 3: viscous mean flow and disturbances Starting from the exact equations described in subsection 1.2.1.1 (two-dimensional case), [81] derived a wave equation for sheared flow in a two-dimensional duct retaining viscosity terms in both the mean flow equation and the equation in the perturbed quantities. However, due to the difficulty of solving the equation, they numerically solved for the inviscid flow case only. To the author's knowledge, this result has not been better explored or developed further in any other subsequent works.

In order to overcome issues related to the simplification of the Navier-Stokes equations by neglecting viscous and thermal effects, with the possibilities offered by the continuing rapid technological advancement of computational capability, there is new interest in numerical approaches to solve the linearized Navier-Stokes equations methodologies for efficient simulations of acoustic wave propagation in ducts retaining the coefficients of viscosity and thermal conductivity in the perturbed equations.

Implications on boundary conditions; Ingard-Myers boundary condition The assumption of inviscid flow has important implications on the modelling of the boundary conditions which have to be provided for both the mean flow equation and the equation in the perturbed quantities.

Within the viscous flow theory, the no-slip boundary condition is customarily employed at any fluid-solid interfaces, imposing that the fluid adheres to the wall (in other words, the flow velocity is zero on a boundary at rest). Although it is an assumption that cannot be derived from any conservation law, it is amply confirmed by experimental observations (cf., for example,Batchelor [11]). That condition is responsible for giving rise to shear stresses and therefore to a shear layer.

Conversely, under a ‘slip’ boundary condition there are no shear stresses to prevent a fluid from moving along the boundary: the only direction an impermeable[14] and rigid[15] boundary can apply a force to the fluid is along the normal to the boundary surface, and a discontinuity in the velocity component tangential to the surface occurs at the surface, from zero at the wall to a non-zero value at the ‘edge’ of the flow region.

Within the inviscid flow theory, such a surface of discontinuity is modelled by a vortex sheet, a concept adopted in aerodynamic studies since its introduction by Helmholtz. A vortex sheet is a surface obtained in the asymptotic limit of a vanishingly-thin (inviscid) boundary layer. In other words, its thickness, $\delta \to 0$, as $Re \to \infty$.

For an acoustically ‘hard’ wall, by definition, the normal component of the fluctuating acoustic particle velocity vanishes.

Surfaces that react elastically to a perturbed field[16] with a response which is independent of the detailed nature of the field and acts only in the direction normal to the wall are named *locally-reacting*. This is the surface type which will be considered in this dissertation (see 1.2.1.6).

In the absence of mean flow or in the case of vanishing mean flow velocity at the wall (i.e., ‘no-slip’ condition), the effect of such liners on the acoustic field is completely characterized by the so-called *surface specific acoustic impedance*, Z, which is defined as the complex ratio of the local Fourier-transformed pressure $\hat{p}\left(\eta\right)$ and normal velocity component $\hat{\boldsymbol{u}}\left(\eta\right) \cdot \boldsymbol{n}$ as follows

$$Z\left(\eta\right) = \frac{\hat{p}\left(\eta\right)}{\hat{\boldsymbol{u}}\left(\eta\right) \cdot \boldsymbol{n}} \tag{1.2.6}$$

---

[14] A wall is impermeable if it does not allow flow through it.

[15] A wall is rigid if it does not move with the pressure exerted on the wall.

[16] Walls which are compliant to acoustic perturbations are commonly referred to as acoustically ’soft’ walls.

where normal vector n points into the wall. In other words, effects of sound propagation inside the liner is not considered.

In the presence of inviscid mean flow (i.e., 'slip' condition), the formulation of a suitable boundary condition for the inviscid equation in the perturbed quantities is more 'subtle' (cf. Rienstra & Hirschberg [111]). In this case, the so-called *Ingard-Myers boundary condition* has been defined by Ingard [58] for the particular case of a plane boundary and reformulated later, in its most general formulation, by Myers [85].

Following Myers' formulation, the surface of discontinuity of the axial mean velocity, which is located in the proximity of the wall can be modelled as an unsteady vortex sheet. On the wall side mean velocity is zero and on the other side it has the value corresponding to that at the 'edge' of mean flow region close to the wall.

The wall can mathematically be described by an (arbitrary curved) steady surface S_0. The unsteady vortex sheet can be represented by a time-dependent surface, $S(t)$, oriented locally parallel to S_0 and expressed mathematically as a perturbation of S_0.

The vortex sheet cannot sustain transverse force [45], so it is assumed to follow the local fluid motion. Moreover, no jumps in the acoustic pressure across the vortex sheet are allowed. Continuity of normal particle displacement is imposed, and after a linearization in the acoustic order and some manipulation, an expression for the acoustic boundary condition is then obtained.

An implication of the boundary condition expression is the requirement of continuity of acoustic particle displacement in the direction normal to the surface across the vortex sheet, irrespective of the thickness of the real boundary layer. Moreover, it has to be noted that this approach assumes that the effects of a finite boundary layer and a vortex sheet on the perturbed field are the same; a point which has generated a good deal of debate.

Before the publication of Myers' work, a number of investigators compared theoretical predictions based on continuity of normal particle velocity and normal particle displacement at the interface to experimental data. Conclusions were mixed [91]. In a paper by

Mungur & Plumblee [82], theoretical results obtained using the two boundary conditions and compared with those of a progressively smaller shear profile suggested a trend toward the particle-displacement results, which seems more favored since there has been widespread adoption of the model within the aeroacoustics community in most theoretical studies and duct acoustic codes where sound attenuation in a moving fluid is of concern.

1.2.1.6 On the disturbance propagation models for aero-engine duct applications

Where swirling flow is negligible[17] (see Sec. 1.2.1.3) typical flows in aero-engine ducts can be divided into two main regions.

- The core of the flow, occupying $s + \delta_{\text{in}} \leqslant r < 1 - \delta_{\text{out}}$, where s and $r = 1$ are the non-dimensional inner and outer wall duct radii, and δ_{in} and δ_{out} are the non-dimensional boundary layer thicknesses at the outer and inner walls, respectively. In this region, the flow moves close to uniform velocity and no temperature gradients are present.
- Thin (but finite) boundary layers of arbitrary profile, where the effects of viscosity and thermal conduction cause strong shear and temperature/density gradients.

Acoustic liners in inlet and bypass ducts are typically characterized as locally-reacting absorbers [60] [84] . They consist of one or more composite sandwich panels consisting of some type of resistive sheets, which may be either perforated materials or resistive meshes, and a hard wall backing sheet bonded to a small honeycomb array of air-filled cavities. Those cavities are directed perpendicular to the wall, and act as Helmholtz resonators meant to dissipate the incident acoustic energy.

Due to the complexities inherent in solving the Pridmore-Brown equation, and the fact that the boundary layer regions are very small compared to the core flow region, early

---

[17] This assumptions is the basis of the present study.

theoretical investigations, typically aiming to identify an optimum acoustic liner impedance for aero-engine ducts, adopted the convective wave equation coupled with the Ingard-Myers boundary conditions [30] [33] [66] [116] [106]. Tester [116] referred to this as the first stage of aero-engine propagation noise modelling.

However, it was expected that the mean velocity profile within the shear layers modifies the propagation of sound and that the prediction of the performance of acoustic treatment based on solving the convective wave equation was most certainly inaccurate. In the inlet duct, the acoustic perturbation propagates upstream and the boundary layer tends to refract waves toward the duct's axis. According to Rice's acoustic mode interpretation [107], waves' propagation angle decreases and converts them into lower-order radial modes. On the other end, in the bypass duct, perturbation propagates downstream and the boundary layer refracts waves toward the wall, increasing the waves' propagation angle.

Therefore, since those early investigations, the question of how modal solutions obtained for an uniform flow would differ from those that are obtained for a non-uniform flow was repeatedly addressed (cf., for example,[113] [81] [82] [65] [66] [34] [35][117] [89]). The experimental results of Tack & Lambert [113] and Plumblee & Dean [100], among others, provided evidence of good agreement between theoretically predicted attenuation spectra using the Pridmore-Brown equation and experiments for a wide range of acoustical lining materials.

However, even if performing a Runge–Kutta integration–iteration method – a computationally low-demanding integration method, only a few modes (the least attenuated) could be extracted because of the low computational capabilities at that time.

For the particular case of aero-engine duct flow where the region of nonuniform flow is very thin, Eversman & Beckemeyer [39] proposed an attractive approach. Taking the cue from the definition of acoustic impedance of a lined wall (1.2.6), they developed a 'lumped' acoustic impedance, which characterises the combined effect of the liner and the boundary layer. Later it will be referred to as effective acoustic impedance Z_{eff}.

It was obtained using an approximation for the Fourier-transformed acoustic pressure and its derivative with respect to the radial direction (proportional to the radial component of the Fourier-transformed acoustic velocity) at the ‘edge’ of the boundary layer based on an inner expansion (cf. [13]) of a solution to the Pridmore-Brown equation.

In essence, their work showed that approximate wavenumbers and mode shapes for acoustic propagation (in a duct containing thin sheared layers only) could be obtained by solving the simpler convected wave equation coupled to an effective acoustic impedance as the boundary condition.

They also showed that, in the limit of vanishing boundary layer thickness (that is, a uniform flow profile), the boundary condition reduces to that of continuity of particle displacement at the wall (that is, the Ingard-Myers’ boundary condition). In other words, the work suggests that, with a thin boundary layer, it seems reasonable to neglect the boundary layer and assume that the mean flow is uniform.

1.2.1.7 Ongoing theoretical work: current outstanding issues

Several limitations have become apparent for both the flow assumptions.

Mode instabilities In the context of hydrodynamic stability, a laminar flow is considered unstable when a small disturbance that is introduced into it grows while being convected, or spread out and contaminate the whole flow. In the former case the perturbation is referred to as convected instability, in the latter case, absolute instability.

The approach used in hydrodynamic stability analysis is very similar to that used in the context of normal mode waveguide theory, which is used in this work. Both methods assume at the outset that the governing equations may be linearized for small disturbances around a steady flow, and that their spatial patterns may be resolved into normal modes. The point of difference is that the normal mode waveguide theory assumes a harmonic time dependence (steady-state analysis of all modes that could potentially be excited) so that a Fourier transform is applied to the linearized Euler equations. Instead, hydrodynamic stability considers an initial-value problem to evaluate the evolution of an initial perturbation in time and, therefore, a Laplace transform is used. Assuming that modes vary with time like exp $(s\,t)$ for some complex number s, the flow is unstable if, at least, for one mode Re(s)>0 : the mode is said to grow in time.

General mathematical criteria based on the properties of the dispersion relation in the complex k- and ω-plane have been formulated to identify an instability and determine its convective or absolute nature. A widely applied method in fluid dynamics [52] and aeroacoustics [17] is the so-called *Briggs–Bers stability analysis,* originally developed by Briggs [22] and Bers [14]. In essence, the method determines the long-time (i.e., $t \to \infty$) behavior of the solution of an initial-value problem.

The debate about whether or not the uniform flow model associated with the Ingard–Myers condition may provide realistic predictions for aero-engine duct applications was mentioned above. In addition to that, one more point of discussion has recurrently been raised over the years: the appearance of anomalous modes. Tester first noted "modes with phase velocities in the opposite direction to that of decay"[116] and he named them 'strange' modes. As it was not confusing enough, their appearance was limited to specific configurations of mean flow velocity, frequency and wall impedance. He speculated that what he believed was an upstream-running mode was, in fact, to be interpreted as a downstream-running instability related to a type of Kelvin-Helmholtz instability inherent to the introduction of a vortex sheet.

It is to be noted that a correct identification of such a mode is of significant practical importance, for example, when applying a mode-matching procedure in order to select and match all appropriate modes.

In a widely referenced paper, Rienstra [108] inspects the behavior of acoustic modes in a lined cylindrical duct with no mean flow and uniform mean flow with the Ingard–Myers condition in the case of large dimensionless angular frequency. In the case of no mean flow, he analytically derived that, for each azimuthal order, there may exist two modes spatially confined in the proximity of the wall, which he named *acoustic surface modes*.

Their steep decay away from the wall is associated with their large imaginary part of the radial wave number.

Their existence depends whether or not the wall acoustic impedance Z lies in particular regions of the complex Z-plane. They do not have an equivalent in the hard-wall duct case.

In the presence of uniform flow only, he found that there may be two more with the same radial decay, which he then named *hydrodynamic surface modes*. Through the application of a stability analysis criterion, he concluded that one of those must be unstable.

Recently, in a series of papers by Brambley & Peake [20] Brambley [17] and Rienstra & Darau [110] it was definitely shown that the combination of the Ingard–Myers condition with some values of impedance (e.g., calculated using the impedance model) forms an ill-posed problem in the time domain.

The conclusion was that the model of a uniform flow with the Ingard-Myers may not be appropriate for practical applications.

Vilenski & Rienstra [125] provided an extended analysis in the case of a mean flow with a boundary layer of finite thickness and showed that the instability was removed.

Recently Rienstra & Darau [110] and Brambley [18] proposed modified Myers conditions – they both include a small but finite boundary layer above the impedance surface, which removes the instability while still allowing a slipping flow above the boundary layer. A comparison between the three conditions has been very recently carried out by Gabard [42].

Mode coupling A significant theoretical progress in the understanding of the structure of the modal disturbances to a steady uniform flow was the work of Kovasznay [68] and Chu & Kovásznay [27], in which the linearized Navier-Stokes equations around a uniform mean flow were re-written in a way that three distinct, first-order, uncoupled solutions of fluctuations could be readily obtained. Solutions were then named acoustic, vortical and entropic modes.

The finding of the co-existence, in small-amplitude disturbances on a uniform mean flow, of those three different types of perturbations was first reported by Rayleigh [29]. Kovasznay [68] and Chu & Kovásznay [27] first provided a formal derivation.

The underlying idea was the Helmholtz' decomposition theorem, which states that any vector velocity field can be decomposed into the sum of a solenoidal (i.e., zero divergence) component and an irrotational (i.e., zero curl) component.

The linearized Navier-Stokes equations were then rewritten replacing the unsteady flow velocity $\boldsymbol{u}'\,(t - z/M_0,\, \mathbf{x}_\perp)$ expressed in a coordinate system which moves with the mean velocity, with two new independent perturbation variables convected with the flow:

$$\boldsymbol{\omega}'\,(t - z/M_0,\, \mathbf{x}_\perp) \equiv \nabla \times \boldsymbol{u}' \tag{1.2.7}$$

$$\vartheta'\,(t - z/M_0,\, \mathbf{x}_\perp) \equiv \nabla \cdot \boldsymbol{u}' \tag{1.2.8}$$

where t is time, z is the axial coordinate, M_0 is the constant mean velocity and $\boldsymbol{x}_\perp$ position vector in the transverse plane. The former is the well known definition of vorticity. The latter is the specific dilatation rate, which represents the rate of volume increase per unit volume of the fluid.

Then, any fluid perturbation variable, q', (i.e., pressure, density and entropy perturbations plus $\boldsymbol{\omega}'$ and ϑ') were decomposed into the sum of three components

$$q' = q^{(\mathrm{aco})} + q^{(\mathrm{vor})} + q^{(\mathrm{ent})}, \tag{1.2.9}$$

where the superscripts (aco), (vor) and (ent) refer to the acoustic, vortical and entropic modes, respectively.

Substituting the sums into the rewritten equations yields three uncoupled subsystems of equations, from which three different uncoupled solutions, one for each component, can be obtained.

The vortical solution is characterized by viscous, incompressible, vorticity fluctuations (i.e.,$\nabla \cdot \boldsymbol{u}^{(\mathrm{vor})} = 0$), which are convected by the mean flow and it has no pressure nor entropy fluctuations.

On the other hand, the acoustic and entropy modes are related to irrotational velocity fluctuations. Moreover, the acoustic mode is associated with the propagation of pressure waves in a compressible medium travelling with the speed of sound (altered by the mean flow velocity). The entropy mode is associated with heat exchanges and it does not generate pressure fluctuations.

In the limit of zero viscosity and zero thermal conductivity (Euler equations), the acoustic mode is then characterized by having zero acoustic component of entropy, $s^{(\mathrm{aco})} = 0$ and the acoustic pressure is directly related to irrotational acoustic velocity fluctuation by the well-known relation:

$$p^{(\mathrm{aco})} = -\frac{D\phi}{Dt}, \tag{1.2.10}$$

where ϕ is the commonly referred (acoustic) velocity potential. Moreover, the entropic mode becomes a time-independent entropy perturbation convected by the mean flow.

When the base flow is non-uniform the analysis becomes much more involved because it is not any more possible to split the flow disturbances into distinct modes obeying separate equations.

Goldstein [46][47] carried out a natural generalization of the theory of Kovasznay to mean flows that could be expressed in terms of a potential. He proposed a convenient method for the determination of the normal modes by starting from the same idea of splitting the perturbation velocity field into potential and vortical components. He showed that vortical disturbances are independent of acoustic disturbances, while acoustic disturbances are produced by vortical ones.

Kousen [67] and Golubev & Atassi [49] studied small-amplitude disturbances in the case of ducted, inviscid, swirling mean flows. The normal mode approach was used to define an eigenvalue problem, which was solved numerically. Kousen [67] suggested that there are three families of perturbation modes. The first family encompasses spinning 'nearly-acoustic' waves, suggesting that the acoustic solutions have a vortical component within them. The second family comprises vortical modes related to the swirl of the mean flow, which have a pressure perturbation and, therefore, he named them 'nearly convected modes'. The third family consists a continuum of modes, which Kousen called 'purely convected modes' because the convective derivative, $\frac{D}{Dt}$, of these modes is zero. Later, Tam & Auriault [114] confirmed the existence of the first two families, but denied the existence of the so-called 'purely convected modes' as they are simply a mathematical artifact.

In the presence of transversely sheared mean flows, the situation is even more complicated. In a recent paper, Goldstein et al. [48] extended further his generalization of the theory of Kovasznay mentioned above to the case of transversely sheared mean flows. His theoretical findings are that the unsteady hydrodynamic mode carries pressure fluctuations and the acoustic mode is no longer irrotational. Moreover, he shows that there is a linear combination of the convected quantities that is equal to a linear combination of the pressure and vorticity.

1.2.2 Methods of solution

The approximation methods used can be roughly divided into two main types: numerical methods and analytical methods.

Numerical methods

For the case of ducts with uniform cross-section, [81] and Mungur & Plumblee [82] were the first to tackle the eigenvalue problem numerically for a number of different velocity profiles using the fourth-order Runge–Kutta method. Recently, the same technique was adopted by Fisher et al. [40]. It has been demonstrated that results are accurate, but for the determination of a large number of eigenvalues more calculation-efficient methods need to be used.

Since the advent of computers in the early 1970s, there has been a continuing interest in developing and improving computational technique for tackling this problem for general non-uniform flow conditions and geometries. After some initial interest in applying the method of weighted residuals, [120, 126], the attention of investigators focused on the finite element method as a viable solution technique to this problem. The finite element method makes use of test functions which are the same subset of complete functions used as basis functions, and contrary to the method of weighted residuals, basis functions have small support. It leads to algebraic systems of sparse matrices, which can be solved efficiently, which substantially reduces the computing efforts while maintaining the same accuracy of the method of weighted residuals [4].

There has been several pioneering works investigating the applicability and accuracy of the finite element method to different duct geometries, which proved from the start the flexibility of its application in duct acoustics. Some of these pioneering works deals with a duct segment of non-uniform cross-section joining two semi-infinite cylindrical ducts of uniform cross-section, where upstream and downstream propagating modes are assumed. The no-flow case is considered in [4], while the case of a subsonic flow with general profile is examined in [6]. The transition region is divided into elements and a weak form finite element formulation for the appropriate governing equations is derived. At the bounding surfaces with the terminating ducts the solution is matched to modal expansions for the uniform sections.

In another group of pioneering papers [5, 6] the case of an infinite duct with constant cross-section is considered. It is shown how the approach of decomposing the acoustic field into duct modes (eigenfunctions) can be particularly convenient. The set of eigenvectors obtained with the finite element method is the discrete analogs of the eigenfunctions which are solutions to the boundary value problem. It was also demonstrated with numerical experiments that the accuracy of the solution set of eigenvalues degenerates rapidly as the modal order increases.

Since the late 1970s, a vast amount of literature on this subject has been published. Following the progresses in the consolidation of the mathematical theory supporting the finite element theory [57], especially in relation to convergence and error estimation [56, 55, 57], a number of papers address the problem of the dispersion properties of finite element models for the convected Helmholtz equation, which describes the acoustic propagation in ducts with uniform mean flows. To the author's knowledge, there is no paper of this sort dealing with the much more complex case of acoustic propagation in ducts with general mean flows.

Recently [43], a new finite element formulation of the two-dimensional eigenvalue problem associated with the Pridmore-Brown equation has been proposed. It can be used to approximate solutions to various classes of problems (ducts with cross section of arbitrary shape and with azimuthally varying liners). The implementation of the finite element method presented in this work will follow that approach.

Analytical methods

Few analytical solutions exists in the literature (see, for example, [71, pag. 87]) and they mostly refer to the two-dimensional model. On assuming that the mean flow uniform except in a thin boundary layer near the duct walls, asymptotic methods can be used.Eversman & Beckemeyer [39] found a first-order asymptotic expansion for the acoustic pressure in a boundary layer with general shape. From this, they introduced an equivalent boundary condition applicable at the outer edge of the boundary layer. This enables the formulation of an eigenvalue problem consisting of the convected Helmholtz equation in the region of uniform core flow with an equivalent boundary condition. They solved the problem numerically using the fourth-order Runge–Kutta method. They proved that in this way they could reduce dramatically the computation time. However, this method assumes that the region of nonuniform flow is very thin, which does not always correspond to real cases. An alternate asymptotic analysis of the sound field in the thin shear layer by the application of the method of matched asymptotic expansions was performed by Myers & Chuang [88].

What Eversman & Beckemeyer [39] showed was the correctness of the condition of the continuity of normal acoustic particle displacement at the duct walls where there is strong near-wall shear. Using a slightly different formulation, Tester [117] came to the same conclusion.

1.3 Motivation for this work

In summary, impressive aircraft engine noise reduction has been achieved thanks to significant advances in *the the theory of small amplitude motions in a compressible fluid confined in a duct.* With the introduction of the more fuel efficient high-pass ratio turbofan engines, jet noise was significantly reduced but fan noise became the predominant noise source [97]. Passive noise control by using acoustic liners inside the nacelle's inlet and bypass ducts is still a valid strategy to further reduce engine noise emissions [63].

The design of an optimal acoustic liner is a challenging task because it has to provide an appreciable benefit over a wide range of frequencies, both those related to steady prominent tones and those included in a wide broadband noise spectrum, and at various flow conditions.

The mean flow field in a nacelle of a turbofan engine is a complex flow: (i) there is a shear flow in the air inlet leading to coupling between vortical perturbations and acoustic waves; (ii) flow between fan and stator and downstream of the turbine stages contains a significant swirling component leading to coupling between vortical perturbations and acoustic waves; (iii) the heat exchanges in the combustion process lead to acoustic-vortical-entropy waves [97].

The numerical computation of small-amplitude perturbations in such complex flow fields can, in principle, be accomplished using direct numerical simulations (DNS), where the full Navier-Stokes equations for three-dimensional, unsteady, compressible flows are solved directly for both mean flow and acoustic and vortical perturbations simultaneously, with no or little assumptions or turbulence modeling involved. In practice, they are not typically used for engineering applications because it requires computationally very expensive simulations to obtain an accurate representation of the solutions, as a wide disparity exists between unsteadiness length scales and flow quantity amplitudes.

Hybrid methods have been developed instead, where the computation of the mean flow field is decoupled from the computation of the small perturbation field. The mean flow field, which is typically assumed steady, viscous and incompressible is solved using classical CFD methods. The small perturbation field is calculated from linearized equations (i.e., linearized Euler equations) about the incompressible mean flow solution using a variety of numerical schemes. Commonly used time-domain numerical schemes that solve the linearized Euler equations are the dispersion relation preserving (DRP) algorithm originally proposed by [115] and the discontinuous Galerkin method (DGM).

When the geometry of the problem can be reasonably approximated by a simple symmetrical shape (e.g., a cylinder) the normal mode (eigenmode) analysis can provide valuable insights into the physics of small-disturbance propagation and its interaction with the main flow and the acoustic surfaces. The behavior of the modal solutions can be thoroughly investigated in relation to different factors, such as mean flow quantities, duct geometry, liner acoustic response, and a detailed analysis of the response of the complete lined duct system to an arbitrary unsteady excitation can be carried out. As a consequence, through an appropriate selection of the above quantities, the theoretical modal structure can be altered in a way that undesired acoustic modes decay exponentially as they move in the axial direction (i.e., modes become ’cut-off’). Therefore, a precise modelling of the structure of the modal solutions is of paramount importance.

A wealth of literature has been devoted to the development of methods and techniques to obtain solutions to the mathematical problem and a critical analysis of theoretical results (see section 1.2). As theoretical results and experimental data have been becoming more and more available, models and solution techniques has evolved into higher levels of sophistication [117]. For practical applications, there are methods, which aim for example to simply identify the least attenuated acoustic modes, or those which implement a mode matching scheme. It is very important to find the optimal balance between computational efficiency and accuracy of results.

Researchers currently debate on the appropriateness and accuracy of current mathematical models of small perturbations in aero-engine ducts. The concern is whether key features of the perturbation spectral structure are sufficiently well captured and characterized. The model based on the convected wave equation and Ingard-Myers boundary conditions offers the simplicity of determining solution using semi-numerical methods, but it raises doubts about the accuracy of the mode spectrum. A number of theoretical studies from the early 1960's and late 1970's ([113] [81] [82] [65] [66] [34] [35][117] [89] have revealed how different boundary layer profiles affect sound attenuation. Moreover, it introduces the issue of ill-posedness associated with the introduction of a vortex-sheet boundary layer, which results in the appearance of spurious modes. Considerations that models based on the Ingard-Myers boundary conditions may not be not sufficiently accurate to foster the development of the next generation of acoustic liner configurations seems to increasingly take hold among academics and nacelle and acoustic liner manufacturers.

On the other hand, adopting the model based on the Pridmore-Brown equation introduces a new kind of problems. First of all, the equation is difficult to solve. Few analytical solutions exists in the literature (see, for example, [71, pag. 87]) and they mostly refer to the two-dimensional model (infinite plane duct model). The complexity of deriving wave propagation solutions in mean shear flow ducts arises from having a wave equation with singularities which occur where the Doppler shifted frequency vanishes.

Rotor-alone and rotor-stator interaction tones, which are the prevailing distinct prominent tonal noise components, are related to the fan's blade passing frequency, which is particularly high in the latest high-bypass-ratio engine designs. Although high Helmholtz numbers (ranging from, say , approx. 20 for the first harmonic to 70 for the third harmonic) and high circumferential wavenumbers (relevant periodicities range between, say, 4 to 30) are of great interest for this application, little attention has been given to high frequencies. A quantification of the effect of refraction of the boundary-layer has not been systematically investigated yet. Studies have so far dealt with frequencies corresponding to Helmholtz number up to 10. Only a series of papers by Vilenski et al. [123][124][125] provide results at high frequencies. At high frequencies this effect is expected to be quite substantial because the acoustic wavelength is comparable to the boundary-layer thickness, and hence will significantly affect the overall noise attenuation.

Finally, the methodologies to obtain solutions to the mathematical problem need to deal with relatively high frequencies. Current numerical methods for solving 3D differential equations are computationally very expensive at such high frequencies.

1.4 Aim and objectives

The aim of this work, as outlined in the initial programme of the study, was to develop fast and efficient analytical and numerical methods to calculate the pressure perturbation modes in acoustically-lined annular ducts containing sheared mean flow.

The key objectives initially set out were:

- Enable numerical simulation at frequencies corresponding to Helmholtz number up to 100;
- Testing the method for its convergence with respect to spatial meshes and validating it on test cases for which an exact solution is available;
- Comparing solutions with recent results obtained with other methods;
- Supplementing the computational approach with analysis based on the perturbation method;

- Carrying out simulations to provide evidence of the influence of different shear mean flow and acoustic linings configurations on the structure of the modal solutions;
- Investigating whether boundary layers with similar shape factor are predicted to have similar pressure modes at high frequencies;
- Carrying out multi-mode simulations to predict noise transmission losses in lined flow ducts.

Although of fundamental theoretical nature on the general subject of small-amplitude unsteady motion of a fluid in a duct, the work was carried out with a view to the specific engineering application of acoustic liner optimization in intake and bypass turbofan aero-engine ducts.

Chapter 2

Formulation of The Problem

As outlined in the initial programme of this study, the basis for all the work is solving the Pridmore-Brown equation. The purpose of this chapter is to introduce the equation together with its appropriate boundary conditions. A derivation from the general governing equations of motion, thermodynamics and continuity of a fluid is provided. This provides an opportunity to review the assumptions and to introduce the notation used throughout this work.

It is assumed that the fluid is compressible and obeying the ideal gas law. The flow is subject to small-amplitude perturbations, such that a linearisation of the governing equations around a background mean flow is justifiable. A parallel shear flow, whose velocity profile is supposed to be known, uniform along its direction, is assumed to be the background mean flow. Mean flow perturbations are assumed to be inviscid and adiabatic.

Nayfeh et al. [91] have demonstrated that the Pridmore-Brown equation can be obtained from a linearisation process of the Navier-Stokes equations (see Chapter 1 for a definition of the equation set). It is noted that the assumption of inviscid and adiabatic process for the flow perturbations was introduced only at the very end of the derivation procedure. Therefore, one of the merits of the approach is to demonstrate that the mean flow can be viscous and heat conducting. However, since the derivation is laborious, it is preferred here, for the sake of brevity (without affecting the final result) to adopt the approach used, for example, by Goldstein [45].

Before proceeding with the derivation of the Pridmore-Brown equation, it is worth stating clearly a fundamental difference in the propagation characteristics of disturbances in the presence of uniform mean flow (convected wave equation) and parallel shear flow (Pridmore-Brown equation). In the former case, any fluid perturbation variable (i.e., pressure, density and entropy perturbations) can be decomposed into the sum of three components: acoustic, vortical and entropic perturbations. Since they are decoupled from each other, acoustic perturbations, vortical perturbations (velocity fluctuations alone) and entropic perturbations (density fluctuations alone) are generally considered separately. On the other hand, in the latter case, the above decoupling do not occur. Acoustic-flow interaction processes, in principle, need to be taken into account: energy can be transferred between an acoustic and a vortical field (thus the difficulty in formulating an expression for sound intensity, as it will be discussed in chapter 6). However, for the types of flow considered in this work, it is reasonable to assume that any acoustic/flow interaction will be small compared to the attenuation losses predicted for the acoustic modes in a lined duct.

2.1 Governing equations

At the outset, it is assumed that the total flow is inviscid and non-heat conducting. This implies that the flow is isentropic along streamlines. The energy balance equation is then uncoupled from the equations of motion and conservation of mass and it can be replaced by the isentropic thermodynamic relation, which relates pressure with density. It is useful to define the local speed of sound as

$$\tilde{C} \triangleq \sqrt{\gamma R \tilde{T}} \,, \tag{2.1.1}$$

where $\gamma = c_P/c_V$ is the ratio of specific heats, R is the specific gas constant and $\tilde{T}$ is the absolute temperature. Pressure can then be determined from density and speed of sound according to the relation

$$\tilde{p} = \frac{\tilde{\rho}\tilde{C}^2}{\gamma} \ . \tag{2.1.2}$$

The starting point here is to present a summary of the governing equations. It is helpful to make use of dimensionless variables. The equations that govern the flow of interest here, written in dimensionless form, are[1]

$$\frac{\partial \rho}{\partial t} + \nabla \cdot (\rho \boldsymbol{u}) = 0 \qquad (\textit{conservation of mass}) \tag{2.1.3}$$

$$\rho\left[\frac{\partial \boldsymbol{u}}{\partial t} + (\boldsymbol{u}\cdot\nabla)\boldsymbol{u}\right] + \nabla p = 0 \qquad (\textit{conservation of momentum}) \tag{2.1.4}$$

$$\gamma p = \rho^{\gamma} \qquad (\textit{isentropic equation of state}) \tag{2.1.5}$$

Here ρ represents the fluid density, $\boldsymbol{u}$ the fluid velocity and p the fluid pressure (all dimensionless). Velocities has been scaled by a reference velocity c_0, lengths has been scaled by a suitable reference length $\tilde{a}$ (e.g., the outer duct radius), and the fluid density has been scaled by a reference density ρ_0. The acoustic pressure has been scaled by $\rho_0 c_0^2$ and time by $\tilde{a}/c_0$. Following the approach to the modeling outlined in Chapter 1, here any source of excitation is excluded.

The flow can be split up into a stationary (mean) flow and small perturbations.

---

[1] Equations (2.1.3) and (2.1.4) can be written, in index notation, as

$$\frac{\partial \rho}{\partial t} + \frac{\partial}{\partial x_i}\rho u_i = 0; \qquad \rho\left[\frac{\partial u_i}{\partial t} + u_j\frac{\partial u_i}{\partial x_j}\right] + \frac{\partial p}{\partial x_i} = 0.$$

where the convention that the repetition of an index denotes a sum over that index (*Einstein summation convention*) is adopted here.

2.2 The mean flow field

The mean flow field is assumed to have density $D(\boldsymbol{x})$, pressure $P(\boldsymbol{x})$, and velocity $\boldsymbol{M}(\boldsymbol{x})$, which are all steady quantities. As before, these quantities are also dimensionless. Equations (2.1.3) to (2.1.5) become

$$\nabla \cdot (D\,\boldsymbol{M}) = 0 \tag{2.2.1}$$

$$D\,(\boldsymbol{M} \cdot \nabla)\,\boldsymbol{M} + \nabla P = 0 \tag{2.2.2}$$

$$\gamma P = D^{\gamma} \tag{2.2.3}$$

The local speed of sound is nondimensionalised based on the reference velocity c_0 and the following relation holds:

$$C^2 = \gamma \frac{P}{D} \tag{2.2.4}$$

2.3 The acoustic field

Now define the acoustic particle velocity, acoustic pressure and acoustic density as the unsteady perturbations superimposed on a steady base flow, i.e.

$$\boldsymbol{u}' = \boldsymbol{u} - \boldsymbol{M} \tag{2.3.1a}$$

$$p' = p - p_0 \tag{2.3.1b}$$

$$\rho' = \rho - \rho_0 \tag{2.3.1c}$$

Substituting these expressions into Equations (2.1.3) to (2.1.5), utilizing Equations (2.2.1) to (2.2.3) and neglecting second- and higher-order terms in the primed variables, the following general acoustic equations are obtained:

$$\frac{D\rho'}{Dt} + \nabla \cdot (D\boldsymbol{u}') + \rho'(\nabla \cdot \boldsymbol{M}) = 0 \tag{2.3.2}$$

$$D\frac{D\boldsymbol{u}'}{Dt} + D(\boldsymbol{u}' \cdot \nabla)\,\boldsymbol{M} + \rho'(\boldsymbol{M} \cdot \nabla)\,\boldsymbol{M} + \nabla p' = 0 \tag{2.3.3}$$

$$p' = C^2 \rho' \tag{2.3.4}$$

where

$$\frac{D}{Dt} = \frac{\partial}{\partial t} + \boldsymbol{M} \cdot \nabla \tag{2.3.5}$$

2.2.2 is the *convective differentiation operator*[2].

2.4 Case of unidirectional, transversely sheared mean flow

Consider $\boldsymbol{M} = \boldsymbol{e}_z \, M(r)$, where $\boldsymbol{e}_z$ denotes the unit vector in the axial direction and r is the radial coordinate in the polar cylindrical coordinate system $(r,\, \theta,\, z)$ (figure 2.4.1). It represents a unidirectional, axially and circumferentially uniform mean flow, but radially nonuniform. In this case, the term$(\boldsymbol{M} \cdot \nabla) \, \boldsymbol{M}$ in 2.2.2 is zero, which yields the result that P and D are constant. Note that choosing their corresponding dimensional values as scaling factor, $P = 1/\gamma$, $D = 1$ and $C = 1$. The gradient operator in cylindrical coordinates is given by

$$\nabla = \boldsymbol{e}_r \, \frac{\partial}{\partial r} + \boldsymbol{e}_\theta \frac{1}{r} \frac{\partial}{\partial \theta} + \boldsymbol{e}_z \, \frac{\partial}{\partial z} \tag{2.4.1}$$

where $\boldsymbol{e}_r$ and $\boldsymbol{e}_\theta$ denote the unit vectors in the radial and azimuthal direction, respectively.

The second term of the acoustic momentum equation (2.3.3) can be rewritten as

$$(\boldsymbol{u}' \cdot \nabla) \, \boldsymbol{M} = \boldsymbol{e}_z \, (\boldsymbol{u}' \cdot \nabla M) = \boldsymbol{e}_z \, \frac{\mathrm{d}M}{\mathrm{d}r} \, u'_r \, , \tag{2.4.2}$$

where u'_r is the radial component of the acoustic particle velocity.

---

[2] It is also known as the *material derivative*. The operator represents the time rate of change seen by an observer moving with the mean flow.

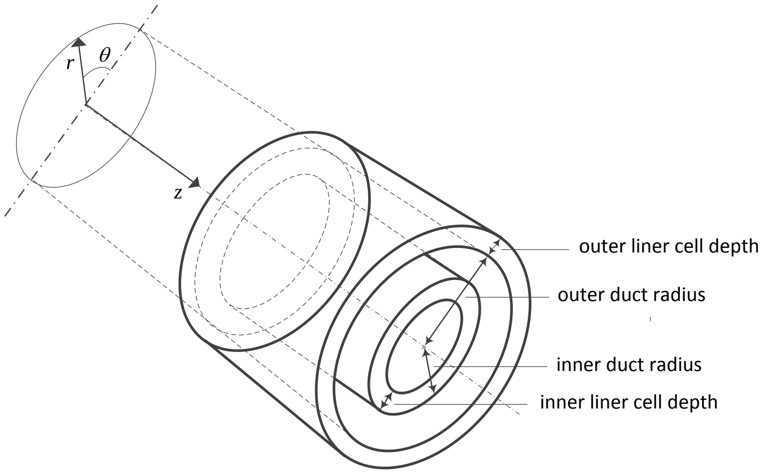

Figure 2.4.1: Geometry of an acoustically lined annular duct, with cylindrical coordinate system used in this work.

The momentum equation (2.3.3) then reduces to

$$\frac{D\boldsymbol{u}'}{Dt} + \boldsymbol{e}_z \frac{\mathrm{d}M}{\mathrm{d}r} u_r' + \nabla p' = 0\,, \tag{2.4.3}$$

where

$$\frac{D}{Dt} = \frac{\partial}{\partial t} + M(r)\frac{\partial}{\partial z}. \tag{2.4.4}$$

The continuity equation (2.3.2) can be combined with equation of state (2.3.4) to yield

$$\frac{Dp'}{Dt} + (\nabla \cdot \boldsymbol{u}') = 0 \tag{2.4.5}$$

Taking the divergence of the momentum equation (2.4.3), operating with the convective differential $\frac{D}{Dt}$ on equation (2.4.5), and subtracting the result yields [3]

---

[3] It can be demonstrated that

$$\nabla\cdot \frac{D\boldsymbol{u}'}{Dt} = \frac{D}{Dt}\,(\nabla\cdot\boldsymbol{u}') + \frac{\mathrm{d}M}{\mathrm{d}r}\,\frac{\partial u_r'}{\partial z}$$

$$\nabla^2 p' - \frac{D^2 p'}{Dt^2} = -2\frac{\mathrm{d}M}{\mathrm{d}r}\frac{\partial u'_r}{\partial z} \tag{2.4.6}$$

where

$$\frac{D^2}{Dt^2} = \frac{\partial^2}{\partial t^2} + 2M\frac{\partial^2}{\partial t \partial z} + M^2\frac{\partial^2}{\partial z^2} \tag{2.4.7}$$

This equation has two dependent variables, p' and u'_r. In the special case where U is constant, it reduces to the homogeneous convected wave equation. When $M = 0$, it reduces to the homogeneous wave equation. To obtain a single differential equation for the acoustic pressure p' only, the following procedure is carried out.

Operating on Eq. (2.4.3) in the following manner

$$\frac{\partial}{\partial z}\left[\boldsymbol{e}_r \cdot \text{Eq. (2.4.3)}\right] = 0$$

leads to the relation

$$\frac{D}{Dt}\frac{\partial u'_r}{\partial z} = -\frac{\partial^2 p'}{\partial r \partial z} \tag{2.4.8}$$

Inserting equation (2.4.8) into $\frac{D}{Dt}\big[\text{Eq. (2.4.6)}\big]$ yields

$$\frac{D}{Dt}\left(\nabla^2 p' - \frac{D^2 p'}{Dt^2}\right) = 2\frac{\mathrm{d}M}{\mathrm{d}r}\frac{\partial^2 p'}{\partial r \partial z}. \tag{2.4.9}$$

2.5 Pridmore-Brown problem

This work considers infinitely-long, uniformly-lined ducts of constant cross-section carrying a high speed, subsonic, unidirectional, transversely sheared mean flow that is uniform in the axial direction (fully developed flow). Since the mean flow properties and boundary conditions do not depend on the time t or the axial coordinate z,, a Fourier

---

.

integral representation of the pressure perturbation in the time and the axial cooordinate exists. Without loss of generality, we can consider a single Fourier component to represent the pressure perturbation, p', and obtain the general result by superposition.

Let us assume

$$p'(t,\, r,\, \theta,\, z) = \Psi(r,\, \theta)\, e^{\mathrm{j}\,(\eta\, t - k_z\, z)}\,, \tag{2.5.1}$$

where the mode shape $\Psi(r,\, \theta)$ is the transverse component of the pressure perturbation (not restricted, at this point, to rotational symmetry in the transverse plane). Substituting this expression in equation (2.4.9) one obtains:

$$(1 - M\,\lambda)\left[\nabla_\perp^2 \Psi + \eta^2 \left[(1 - M\,\lambda)^2 - \lambda^2\right]\, \Psi\right] + 2\lambda\, \nabla_\perp M\, \cdot\, \nabla_\perp \Psi = 0 \text{ in } \Omega\,, \tag{2.5.2}$$

where Ω denotes the acoustic domain,$\nabla_\perp$ denotes the gradient operator in the direction transverse to the z axis and $\lambda = k_z/\eta$.

When the Pridmore-Brown equation (2.5.2) is employed to describe pressure perturbations in aero-engine ducts, the parallel mean flow is typically described as consisting of a uniform core velocity profile and no-slip, small boundary layers (see, for example, figures 2.6.1(b) and 2.6.1(c)). The duct walls are commonly assumed to be locally-reacting impedance surfaces.

In this case, standard locally-reacting impedance boundary conditions to the Pridmore-Brown equation would be sufficient because the mean flow vanishes at the wall (no-slip boundary condition), given by

$$\boldsymbol{n} \cdot \nabla_\perp \Psi = -\frac{\mathrm{j}\,\eta}{Z} \Psi \qquad \text{on } \partial\Omega\,, \tag{2.5.3}$$

where $\partial\Omega$ denotes the surface of the acoustic domain, and Z is the specific acoustic impedance, which is a function of frequency (and possibly a function of the azimuthal angle, θ).

Indeed, that would be the case in the first study of chapter 5, where the linear-without-slip and 1/7th power law boundary-layer flow profiles are compared (see figures 2.6.1(b) and 2.6.1(c) , respectively).

However, in the second study of chapter 5, it is investigated whether it is possible to model any arbitrary boundary layer profile just using a linear-with-slip boundary layer (see figure 2.6.1(d)), whose shape factor can be adjusted by varying the wall velocity.

In order to provide a general problem formulation, the Ingard–Myers boundary conditions are imposed to equation (2.5.2), which, for this problem, take the form

$$\boldsymbol{n} \cdot \nabla_{\perp} \Psi + \frac{\mathrm{j}\,\eta}{Z}(1 - M_{\text{wall}}\lambda)^2 \Psi = 0 \qquad \text{on } \partial\Omega\,, \tag{2.5.4}$$

where M_{wall} denotes the value of the mean-flow velocity at the wall. Note that, in the case of zero mean flow at the wall, standard impedance boundary conditions are recovered.

Equations (2.5.2) and (2.5.4) represent a third-order eigenvalue problem with eigenvalue λ and eigenfunction Ψ. The problem is linear, but has variable coefficients. The eigenvalue appears in the boundary condition.

For simplicity of exposition, the boundary value problem consisting of the partial differential equation (2.5.2) and boundary conditions (2.5.4) will be herein referred to as the *Pridmore-Brown problem.*

2.6 On the Ingard–Myers boundary conditions

A summary of theoretical considerations which lead to the formulation of the Ingard-Myers boundary conditions and a brief description of the fundamental problem found in its modelling are provided in chapter 1.

Here, a few additional considerations are included, with particular respect to the way the Ingard–Myers impedance model may affect the solutions to the problem considered in this work.

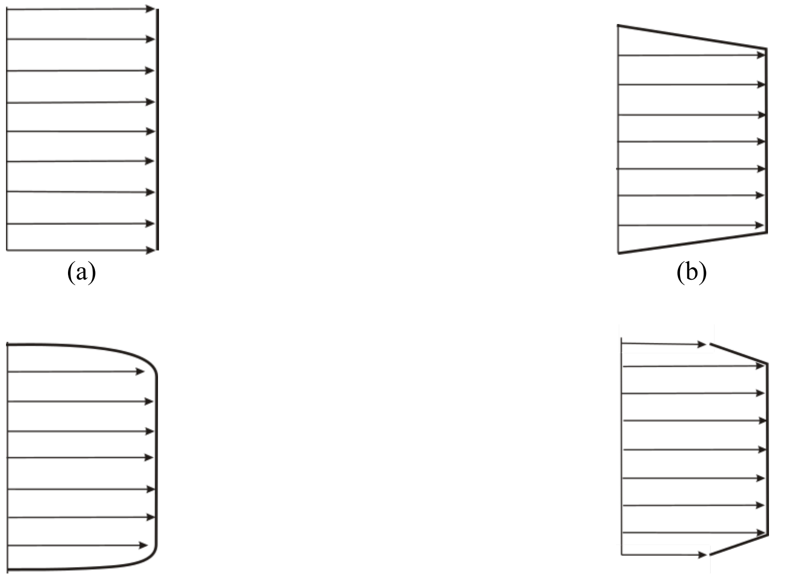

(a) (b)

(c) (d)

Figure 2.6.1: Types of radial mean-flow velocity profiles used in this work: (a) uniform; (b) uniform core and linear-without-slip boundary-layer; (c) uniform core and 1/7th power law boundary-layer (no slip); (d) uniform core and linear-with-slip boundary-layer.

Since early theoretical developments in aero-engine duct acoustics, the Ingard–Myers boundary conditions have been widely adopted to approximating, in a simple mathematical manner, the interaction of a liner's impedance and a thin boundary layer on pressure perturbations. However, considerations that the model is not sufficiently accurate have been made ([113] [81] [82] [65] [66] [34] [35][117] [89]). It has only been quite recently that alternatives to the Ingard–Myers boundary conditions have been put forward (cf., for example, [42]), since mathematical considerations by Brambley [17] had proven that using these conditions in the time domain introduces instabilities with unbounded growth rate. Within the time frame of this work, it has not been possible to consider such alternatives.

It has to be noted that these instabilities are mathematical artefacts and they are different from unstable surface modes which may occur in the presence of a uniform mean flow, as identified by Rienstra [108], or a boundary-layer type mean flow, as identified by Vilenski & Rienstra [125], depending on mean flow properties (Mach number, boundary layer thickness) and liner impedance.

In the frequency domain, as it is the case in the present work, instabilities would reveal themselves as modes whose amplitude grows with distance along the propagation direction, instead of decaying. The problem becomes that of identifying their correct propagation direction.

If it is known for certain that a mode decays, a simple approach to identify its propagation direction consists of inspecting its axial phase velocity, $v_{\mathrm{ph}} = \eta/k_z$. However, according to this, instabilities would be incorrectly classified. In this work, following Moinier & Giles [78], the mode propagation direction is determined by evaluating its axial group velocity, $v_{\mathrm{g}} = \left(\frac{\mathrm{d}}{\mathrm{d}\eta} k_z\right)^{-1}$, which makes the direction identification unequivocally clear, as the mode group velocity defines the propagation of the energy flux.

Chapter 3

The Finite Element Method

3.1 Theory of the FEM

In this section, the finite element method (FEM) is applied to the convected Helmholtz equation and to the Pridmore–Brown equation with Ingard–Myers boundary conditions. We begin with a review of essential facts concerning the mathematical theory of the FEM to give basic definitions and results which will be used in this section and to establish the formalism that will be adopted. The presentation of such background material mainly follows the conceptual approach and the notation found in recent textbooks in Applied Mathematics on FEM [21, 54].

First, a *variational* (also called *weak*) formulation of linear elliptic boundary value problems is given making use of concepts of functional analysis such as Hilbert function spaces, linear and sesquilinear forms. Then, the Galerkin formulation is presented as a restriction of the variational formulation to an approximating finite-dimensional subspace. Finally, the FEM formulation is introduced as a special case of the Galerkin formulation where the problem domain is partitioned in finite elements and the basis functions are constructed implicitly in an element-by-element manner in terms of local interpolating functions (*shape* functions).

Following this approach, according to which we move from a higher level of abstraction to progressively lower levels of abstraction, the FEM is unfolded in a broader perspective as a particular case of a more general framework of approximation methods. This may be useful when relating it to other methods, such as the weighted residual method.

3.1.1 Mathematical preliminaries

Let us first review some basic definitions.

Definition 3.1. Suppose V is a complex vector space. A complex-valued ***linear functional*** l (also called linear form) on V is a linear function $l : V \mapsto \mathbb{C}$, i.e.,

$$l(u_1 + \lambda u_2) = l(u_1) + \lambda l(u_2) \quad \forall\, u_1, u_2 \in V,\ \lambda \in \mathbb{C}$$

Definition 3.2. A ***sesquilinear form*** a on V is a mapping $a : V \times V \mapsto \mathbb{C}$, with the properties:

$$\begin{aligned} a(v, u_1 + \lambda u_2) &= a(v, u_1) + \lambda a(v, u_2) \qquad \text{i.e., is linear form for } v \text{fixed} \\ a(v_1 + \lambda v_2, u) &= a(v_1, u) + \overline{\lambda} a(v_2, u) \qquad \text{i.e., is anti-linear form for } u \text{fixed} \end{aligned}$$

where the overbar denotes the complex conjugate.

Now suppose V is a complex Hilbert space with some complex inner product denoted by $\langle \cdot\,, \cdot \rangle$ and let $\|u\| = \sqrt{\langle u, u \rangle}$ be the norm associated with the inner product.

Definition 3.3. A sesquilinear form a on V is said to be *V-elliptic* (also called *coercive*) if

$$\exists\, \alpha \text{ such that } a\,(u, u) \geq \alpha\, \|u\|^2 \quad \forall u \in V$$

Definition 3.4. A sesquilinear form a on V is said to be *bounded* if

$$\exists\, \beta \text{ such that } |a\,(v, u)| \leq \beta\, \|u\|\, \|v\| \quad \forall u, v \in V$$

3.1.1.1 Variational formulation of linear elliptic BVPs

Suppose V is a complex Hilbert space. Let the expression $a\left(\,\cdot\,,\,\cdot\,\right)$ denote an elliptic, bounded sesquilinear form on V and F denote a complex-valued linear functional on V.

Definition 3.5. A variational problem is the following:

$$\text{Find } u \in V \quad \text{such that} \quad a(v,u) = F(v) \qquad \forall v \in V. \tag{3.1.1}$$

3.1.1.2 Galerkin approximation problem

The Galerkin approximation problem is based on two fundamental ideas:

- the variational formulation of the problem,
- restriction of the spaces.

Definition 3.6. Given an arbitrary finite-dimensional subspace $V_h \subset V$, a *Galerkin approximation problem* is the following:

$$\text{Find } u_h \in V_h(\Omega) \quad \text{such that} \quad a(v,u_h) = F(v) \quad \forall v \in V_h. \tag{3.1.2}$$

A Galerkin solution to the variational problem (3.1.1) is an approximate solution $u_h \approx u$ of the form

$$u_h = \sum_{j=1}^{N_{\text{glob}}} c_j \phi_j \tag{3.1.3}$$

where the functions ϕ_j are preselected and form a basis for a finite-dimensional subspace V_h, and c_j are unknown complex coefficients to be determined.

3.1.2 The general FEM formulation

The FEM is a special implementation of the Galerkin's method where the approximate solution u_h is sought among continuous, piecewise, polynomial functions of degree p

on $\overline{\Omega}$. These are functions that reduce to a polynomial of degree p on each element K into which the domain has been partitioned. The implementation involves the following steps.

1. Discretization of domain
2. Definition of global-to-local index
3. Definition of local basis functions and local interpolation
4. Definition of global basis functions and global interpolation
5. Mapping from reference elements
6. Computation of element matrices
7. Assembly of the linear system
8. Solution of the linear system

Points 1 to 5 will be explained in their general in this sub-section. Points 6 and 7 require a specific problem formulation and therefore will be explained in the sub-sections on convected wave problem and Pridmore-Brown problem.

3.1.2.1 Discretization of the domain

Definition 3.7. A ***mesh*** is a subdivision $\mathcal{T}_h = \{K_i\}$ of the domain $\overline{\Omega}$ into a finite number of open subsets K_i with the following properties:

1. $\bigcup \overline{K_i} = \overline{\Omega}$
2. For $i \neq j$, $K_i \cap K_j = \emptyset$

In other words, the collection of open sets $\{K_i\}$ forms a non-overlapping decomposition of $\overline{\Omega}$. Each subdivision is typically characterized by its *mesh size* h, where

$$h = \max\{\text{diam}\,(K)\ \mid K \in \mathcal{T}_h\}$$

and diam (K) is a suitable criteria to characterise width.

Note that in a space with more than one dimension it is necessary to require an additional property to the mesh , which in this case is called *conforming mesh*. Let us limit in the following to elements having simple shapes, that is they consists of a group of vertices bounded by straight lines (e.g., triangles, quadrilaterals in two dimensions, tetrahedra and hexahedra in three dimensions).

Definition 3.8. A *conforming mesh* has the following additional property:

For $i \neq j$, if $\overline{K_i} \cap \overline{K_j} \neq \emptyset$, then $\overline{K_i} \cap \overline{K_j}$ is a common vertex or a common edge.

We will see later that the global basis functions are constructed in an element-by-element manner. The latter requirement ensures the continuity of the global basis functions. See Figure 3.1.1 for examples of conforming and nonconforming meshes.

From the domain partition a system of points $\{\boldsymbol{a}_i\}$, called *nodes,* is generated. We will denote the total numer of nodes with N_{glob}.

(a)

(c)

Figure 3.1.1: Examples of conforming mesh (a), and nonconforming mesh (b).

3.1.2.2 Global-to-local index

It is convenient to introduce a numbering scheme, $n(e,\, j)$, which associates local node labels to global node labels to simplify the notation and to facilite the assembly methodology, as will be shown later. In the literature, it is sometimes named *global-to-local index* ([21]) or *connectivity matrix* ([102]).

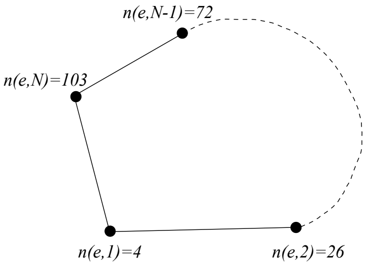

Figure 3.1.2: Graphical representation of the global-to-local index.

Consider a general mesh as defined in the previous paragraph. Each element has a number of interpolating nodes N_{en}. For simplicity, let us assume that this number is the same for each element of the mesh. For each element, a *local* node label is assigned to its interpolating nodes, ranging between 1 and N_{en} following a certain numbering criteria. For example, in the case of one-dimensional mesh over the domain $\left[x_0,\, x_{N_{\text{glob}}}\right]$, for each sub-interval a *local* node label $i = 1$ can be assigned to the the node at the left end of the sub-interval, and progressive integer numbers can be assigned to the other nodes while moving left-to-right towards the last node at the right end.

The global-to-local index is defined such that $n(e,\, j)$ is the global label of the j-th node of the e-th element. Thus, j takes values in the range: $1,\, \dots,\, N_{\text{en}}$. $n(e,\, j)$ takes values in the range: $1,\, \dots,\, N_{\text{glob}}$, where N_{glob} is the total number of global nodes.

3.1.2.3 Local basis functions and local interpolation

Suppose $K_e \in \mathcal{T}_h$ be an element with nodes $\left\{\boldsymbol{a}_{n(e,\,i)}\right\}_{i=1,\,\dots,\,N_{\text{en}}} \subset \mathbb{R}^d$ (see figure 3.1.2). Let $\mathcal{P}_p^d(K_e)$ denote the space of d-dimensional polynomial functions of order p on K_e. This space contains all functions of the form

$$\sum_{l_1+\cdots+l_d \le p} c_{l_1,l_2,\cdots,l_d}\, x_1^{l_1}\, x_2^{l_2} \cdots x_d^{l_d} \tag{3.1.4}$$

Let v be a sufficiently smooth [1] arbitrary function on K_e. A *local interpolation problem* is defined by:

$$\text{Find a local interpolant } v_I \in \mathcal{P}_p^d(K_e) \text{ such that } v(\boldsymbol{a}_{n(e,\,i)}) = v(\boldsymbol{a}_{n(e,\,i)})\ \forall i = 1,\,\ldots,\,N_{\text{en}}. \tag{3.1.5}$$

Let functions $\left\{\phi^e_{n(e,\,i)}\right\}$ be a basis for $\mathcal{P}_p^d(K_e)$. They are so-called ***local basis functions*** or *shape* functions. They fulfil the requirement:

$$\phi^e_{n(e,\,i)}(\boldsymbol{a}_{n(e,\,j)}) = \delta_{ij} \tag{3.1.6}$$

The solution of the local interpolation problem is then given by

$$v_I = \sum_{i=1}^{3} v_i\,\phi^e_{n(e,\,i)} \tag{3.1.7}$$

where $v_i = v(\boldsymbol{a}_{n(e,\,i)})$.

3.1.2.4 Global basis functions and global interpolation

The restriction of the FEM solution u_I to each element is a polynomial of degree up to p in each spatial variable and u_I is continuous across all boundaries between neighboring mesh elements throughout Ω. For

Suppose Ω is a domain with a subdivision $\mathcal{T}_h = \{K_e\}$. The *global interpolant* u_I for u over Ω is defined by:

$$u_I = u_I|_{K_e} \qquad \text{for all } K_e \in \mathcal{T}_h$$

(3

where $u_I|_{K_i}$ denotes the restriction of the function u_I to the element K_i.

We now define the space of all continuous piecewise functions as

$$S_h^p(\overline{\Omega}) := \left\{u_I \in \mathcal{C}(\overline{\Omega}) \quad | \quad u|_{K_e} \in \mathcal{P}_p(K_i) \quad \text{for all } K_e \in \mathcal{T}_h\right\} \tag{3.1.9}$$

---

[1] A more precise requirement on function v will be given later.

where $u|_{K_e}$ indicates the restriction of u to K_e.

A basis $\{\phi_i\}$ for the space $S_h^p(\overline{\Omega})$ defined on $\mathcal{T}_h$ can be easily obtained by combining local basis functions on neighboring elements (see Figure 3.1.3). The functions ϕ_i are called ***global basis functions*** and they fulfil the following requirements:

- $\phi_i(\boldsymbol{a}_j) = \delta_{ij}$;
- ϕ_i vanishes on any element that does not contain the node $\boldsymbol{a}_i$;
- suppϕ_i consists of all elements that contain the node $\boldsymbol{a}_i$ (see Figure 3.1.7)

The approximate solution can therefore be described by the expansion:

$$u_I(\boldsymbol{a}) = \sum_{i=1}^{N_{\text{glob}}} \hat{u}_i\, \phi_i(\boldsymbol{a}) = \left[\phi_1(\boldsymbol{a}),\, \ldots,\, \phi_{N_{\text{glob}}}(\boldsymbol{a})\right] \begin{bmatrix} \hat{u}_1 \\ \ldots \\ \hat{u}_{N_{\text{glob}}} \end{bmatrix} \tag{3.1.10}$$

where N_{glob} is the total number of nodes, also called *degrees of freedom,* and the coefficients $\hat{u}_i$ are the unknown values at the nodes $\hat{u}_i = u(\boldsymbol{a}_i)$.

Example 3.1 (Two-node, one-dimensional element)**.** *Consider a one-dimensional domain* $[x_0,\, x_n]$ *and a sufficiently smooth function* f *on this domain. Let the domain be partitioned by a finite number of points* $x_0 < x_1 < x_2 < \ldots < x_n$*. Consider any interval* $I_e = [x_i,\, x_j]$ *and the restriction* $p = u|_{I_e}$ *of the function* u *to this interval* I_e*.*

An approximation p_I *to* p *on the interval* I_e *is sought in the form of a linear polynomial, that is*

$$p_I = c_0 + c_1 x \tag{3.1.11}$$

The two constants c_0 *and* c_1 *can be determined by solving a set of two equations, which can be obtained by inserting the element nodal coordinates,* x_i *and* x_j*, and the appropriate nodal values of the function* p_I *into Equation* (3.1.11)

$$\begin{cases} p_I(x_i) = p_i = c_0 + c_1 x_i \\ p_I(x_j) = p_j = c_0 + c_1 x_j \end{cases} \tag{3.1.12}$$

where $p_i \equiv p(x_i)$ *and* $p_j \equiv p(x_j)$ *are the unknown values at the nodes* i *and* j*, respectively. Solving for* c_0 *and* c_1 *yields*

$$p_I(x) = p_i\,\phi_i^e + p_j\,\phi_j^e \tag{3.1.13}$$

where

$$\phi_i^e(x) = \frac{x_j - x}{x_j - x_i} \tag{3.1.14a}$$

$$\phi_j^e(x) = \frac{x - x_i}{x_j - x_i} \tag{3.1.14b}$$

are the local basis functions on the element I_e*.*

Global basis functions can be built from the above local basis functions as follows (see Figures 3.1.3 and 3.1.4).

$$\phi_j(x) = \begin{cases} \dfrac{x - x_i}{x_j - x_i} & x \in I_l = [x_i,\, x_j], \\ \\ \dfrac{x_k - x}{x_k - x_j} & x \in I_m = [x_b,\, x_c], \\ \\ 0 & \textit{otherwise}. \end{cases} \tag{3.1.15}$$

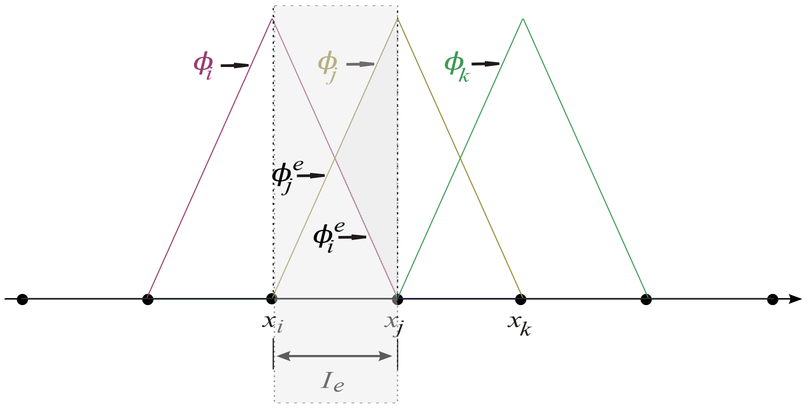

Figure 3.1.3: The two linear local basis functions $\phi_i^e(x)$ and $\phi_j^e(x)$ on the element $I_e = [x_i,\, x_j]$ and piecewise-linear global basis functions for global nodes i, j, and k; finite element mesh with equidistant points.

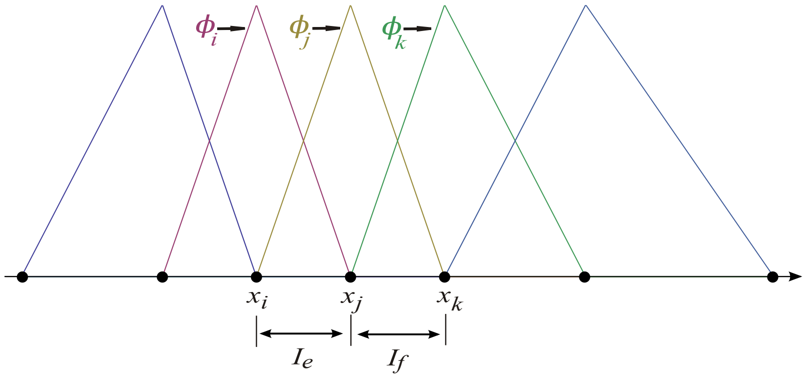

Figure 3.1.4: Piecewise-linear global basis functions defined on a finite element mesh with non-equidistant points.

3.1.2.5 Mapping from reference elements

An affine mapping of a 'reference' or 'master' element $[-1,\ 1]$ to the element $[x_i, x_j]$ is defined

$$x = Q(\xi) = \frac{x_i + x_j}{2} + \frac{x_j - x_i}{2}\xi \tag{3.1.16}$$

The interpolant p_I on the interval I_e of Equation (3.1.11) can be re-written as

$$p_I\left(Q(\xi)\right) \equiv \psi_I(\xi) = \psi_1\, N_1(\xi) + \psi_2\, N_2(\xi) \tag{3.1.17}$$

Here $\psi_1 \equiv p_I\left(Q(\xi = -1)\right)$, $\psi_2 \equiv p_I\left(Q(\xi = 1)\right)$ and

$$N_1(\xi) \equiv \frac{1-\xi}{2} \tag{3.1.18a}$$

$$N_2(\xi) \equiv \frac{1+\xi}{2} \tag{3.1.18b}$$

are linear *local basis functions* on the 'reference' element $[-1,\ 1]$.

Example 3.2 (Three-node, one-dimensional element)**.** *An approximation to p on the interval $I_e = [x_i, x_j]$ is now sought in the form of quadratic polynomial*

$$p_I = c_0 + c_1 x + c_2 x^2. \tag{3.1.19}$$

It is defined by three coefficients and requires three interpolation nodes. Consider the interval having three nodes: one corresponding to the left end of the interval at x_i, one corresponding to the right end at x_j, and one at the interval mid-point $x_m = (x_i + x_j)/2$. It is convenient to introduce the affine mapping of Equation (3.1.16)*. The origin of the local coordinate system ξ is now at the node x_m corresponding the interval mid-point. Then Equation* (3.1.19) *can be rewritten in term of the local coordinate ξ as*

$$\begin{aligned} p_I\left(Q(\xi)\right) \equiv \psi_I(\xi) &= \left(c_0 + c_1\, x_m + c_2\, x_m^2\right) + (c_1 + 2\, c_2\, x_m)\delta\, \xi + c_2\, \delta^2\, \xi^2 \\ &\equiv \alpha' + \beta'\xi + \gamma'\xi^2 \end{aligned}$$

where $\delta = (x_c - x_a)/2$. *The three constants* α', β' *and* γ' *can be evaluated by solving a set of three equations, which can be obtained by inserting the element nodal local coordinates and the appropriate nodal values of the function* ψ *into Equation* (3.1.19)

$$\begin{cases} \psi_1 \equiv p_I\left(Q(\xi=-1)\right) = \alpha' - \beta' + \gamma' \\ \psi_2 \equiv p_I\left(Q(\xi=0)\right) = \alpha' \\ \psi_3 \equiv p_I\left(Q(\xi=1)\right) = \alpha' + \beta' + \gamma' \end{cases} \tag{3.1.20}$$

Solving for α', β' *and* γ' *, this leads to*

$$\psi_I = \psi_1 + \frac{\psi_2 - \psi_0}{2}\,\xi + \frac{\psi_0 + \psi_2 - 2\psi_1}{2}\,\xi^2 = \psi_1\,N_1(\xi) + \psi_2\,N_2(\xi) + \psi_3\,N_3(\xi) \tag{3.1.21}$$

where

$$N_1(\xi) \;\equiv\; \frac{1}{2}\,\xi\,(\xi - 1) \tag{3.1.22a}$$

$$N_2(\xi) \;\equiv\; 1 - \xi^2 \tag{3.1.22b}$$

$$N_3(\xi) \;\equiv\; \frac{1}{2}\,\xi\,(\xi + 1) \tag{3.1.22c}$$

are quadratic local basis functions on the interval $I_e = [-1, 1]$.

Example 3.3. *Let* $d = 2$ *(two-dimensional space) and* $k = 1$ *(linear polynomial case). Consider a triangular element* T_e *with vertices having coordinates* $\{\,(x_1,\, y_1),\; (x_2,\, y_2),\; (x_3,\, y_3)\,\}$ *. A set of linear functions*

$$\phi_i^e\,(x, y) = \alpha_i + \beta_i x + \gamma_i y \qquad i = 1,\, 2,\, 3$$

each associated with the vertex $(x_i,\, y_i)$ *and satisfying*

$$\phi_i^e(x_j,\, y_j) = \delta_{ij}$$

can be found by solving the system

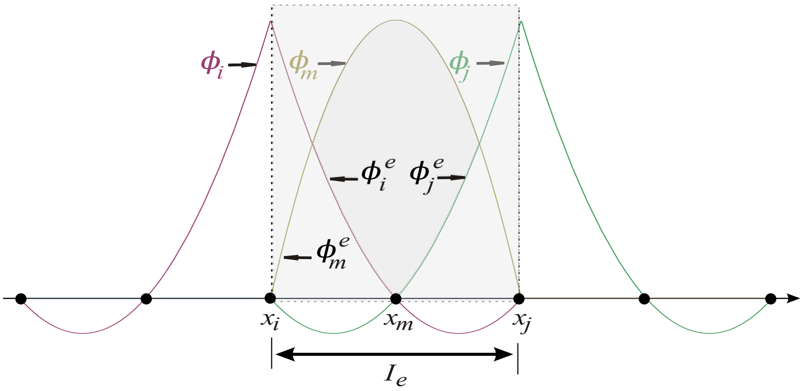

Figure 3.1.5: The three quadratic local basis functions $\phi_i^e(x)$, $\phi_m^e(x)$ and $\phi_j^e(x)$ on the element $I_e = [x_i, x_j]$ and piecewise-linear global basis functions for global nodes i, m, and j; finite element mesh with equidistant points.

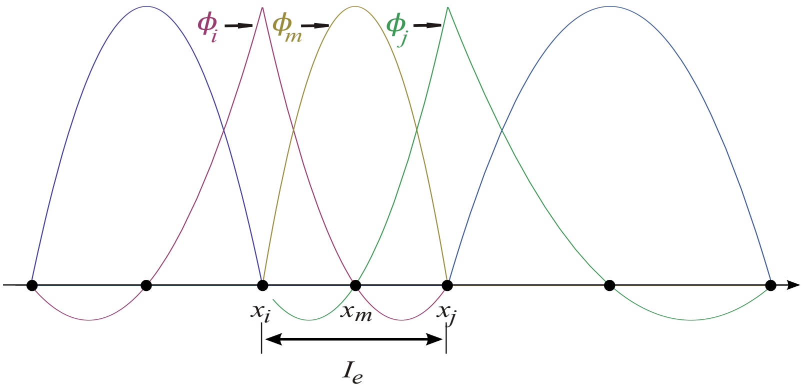

Figure 3.1.6: Piecewise-quadratic global basis functions defined on a finite element mesh with non-equidistant points. Note that the extra nodes such as x_m are added at the midpoint of each element.

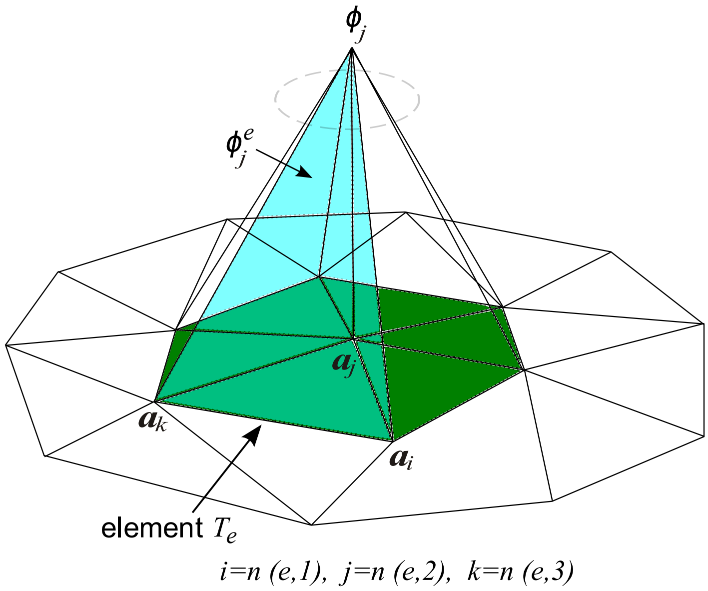

Figure 3.1.7: ’Tent-like’ global basis function ϕ_j associated with the global node j. The contribution of the linear local basis function ϕ_j^e on the element e to the global basis function ϕ_j is highlighted. Note that suppϕ_j (in green colour) consists of all elements that contain the node $\boldsymbol{a}_{,}$.

$$
\begin{bmatrix} 1 & x_1 & y_1 \\ 1 & x_2 & y_2 \\ 1 & x_3 & y_3 \end{bmatrix}
\begin{bmatrix} \alpha_1 & \alpha_2 & \alpha_3 \\ \beta_1 & \beta_2 & \beta_3 \\ \gamma_1 & \gamma_2 & \gamma_3 \end{bmatrix}
=
\begin{bmatrix} 1 & 0 & 0 \\ 0 & 1 & 0 \\ 0 & 0 & 1 \end{bmatrix} .
$$

The solution of the interpolation problem (3.1.5) is then given by

$$
p_I = \sum_{i=1}^{3} p_i \, \phi_i^e \qquad (3.1.23)
$$

where $p_i = p(x_i,\, y_i)$*. The set* $\{\phi_i^e\}_{i=1,\ldots,3}$ *form a basis for* $\mathcal{P}_1^2(T)$*.*

3.1.2.6 Finite element approximation problem

We now give a formal definition of a finite element approximation problem.

Given an arbitrary finite-dimensional subspace $V_h = S_h^p(\overline{\Omega})$, a finite element approximation problem is the following:

$$\text{Find } u_I \in S_h^p(\overline{\Omega}) \quad \text{such that} \quad a(v, u_I) = F(v) \quad \forall v \in S_h^p(\overline{\Omega}) \,. \tag{3.1.24}$$

Note that any $v \in S_h^p(\overline{\Omega})$ can be written in terms of the basis functions $\{\phi_i\}$, that is

$$v(\boldsymbol{a}) = \sum_{j=1}^{N_{\text{glob}}} d_j \, \phi_j(\boldsymbol{a}) = \begin{bmatrix} d_1, \, \ldots, \, d_{N_{\text{glob}}} \end{bmatrix} \begin{bmatrix} \phi_1(\boldsymbol{a}) \\ \ldots \\ \phi(\boldsymbol{a}) \end{bmatrix} \tag{3.1.25}$$

where d_j are complex coefficients. Substituting (3.1.10) and (3.1.25) in (3.1.24), using the properties of the sesquilinear form and the linear functional yields

$$\begin{aligned} \begin{bmatrix} d_1, \, \ldots, \, d_{N_{\text{glob}}} \end{bmatrix} \begin{bmatrix} a(\phi_1, \phi_1) & \ldots & a(\phi_1, \phi_{N_{\text{glob}}}) \\ \ldots & \ldots & \ldots \\ a(\phi_{N_{\text{glob}}}, \phi_1) & \ldots & a(\phi_{N_{\text{glob}}}, \phi_{N_{\text{glob}}}) \end{bmatrix} \begin{bmatrix} u_1 \\ \ldots \\ u_{N_{\text{glob}}} \end{bmatrix} &= \\ = \begin{bmatrix} d_1, \, \ldots, \, d_{N_{\text{glob}}} \end{bmatrix} \begin{bmatrix} F(\phi_1) \\ \ldots \\ F(\phi_{N_{\text{glob}}}) \end{bmatrix} & \end{aligned}$$

The requirement that (3.1.24) be satisfied for all $v \in S_h^p(\overline{\Omega})$ implies that

$$\begin{bmatrix} a(\phi_1, \phi_1) & \ldots & a(\phi_1, \phi_{N_{\text{glob}}}) \\ \ldots & \ldots & \ldots \\ a(\phi_{N_{\text{glob}}}, \phi_1) & \ldots & a(\phi_{N_{\text{glob}}}, \phi_{N_{\text{glob}}}) \end{bmatrix} \begin{bmatrix} u_1 \\ \ldots \\ u_{N_{\text{glob}}} \end{bmatrix} = \begin{bmatrix} F(\phi_1) \\ \ldots \\ F(\phi_{N_{\text{glob}}}) \end{bmatrix} \tag{3.1.26}$$

3.2 The FEM formulation for the Pridmore-Brown problem

3.2.1 Two-dimensional problem

Variational formulation. Let $\Omega \subseteq \mathbb{R}^2$ be an open, bounded and connected set with sufficiently smooth boundary $\partial\Omega$ (see Figure 3.2.1). Consider the problem

$$\begin{cases} (1-M\lambda)\Big[\nabla^2\Psi + \eta^2\big[(1-M\lambda)^2-\lambda^2\big]\,\Psi\Big]+ & \\ \qquad\qquad\qquad\qquad +2\lambda\,\nabla M\,\cdot\,\nabla\Psi = 0 & \text{in}\,\Omega \\ \nabla\Psi\cdot\boldsymbol{n}+\mathrm{j}\,\eta\,A\,(1-M_{\mathrm{wall}}\lambda)^2\Psi & \text{on}\,\partial\Omega \end{cases} \tag{3.2.1a}$$

with $M:\Omega\mapsto\mathbb{R}$ and $\lambda\in\mathbb{C}$. $A = Z^{-1}$ is the specific acoustic admittance and $\boldsymbol{n}$ is the outward-pointing unit normal vector to $\partial\Omega$.

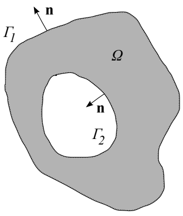

Figure 3.2.1: Two-dimensional region Ω with boundary $\partial\Omega = \mathit{\Gamma}_{1\cup}\mathit{\Gamma}_2$ and normal vector $\boldsymbol{n}$ to $\mathit{\Gamma}_1$ and $\mathit{\Gamma}_2$.

For notation convenience, let us define a linear operator

$$\mathcal{L}\,[\Psi] = \left\{\,(1-M\lambda)\Big[\nabla^2+\eta^2\big[(1-M\lambda)^2-\lambda^2\big]\Big]+2\lambda\,\nabla M\,\cdot\,\nabla\right\}\,\Psi \tag{3.2.2}$$

Let its domain be

$$D\,(\mathcal{L}) = \big\{\,\Psi\in\mathcal{C}^2(\Omega)\,\cap\,\mathcal{C}^1(\overline{\Omega})\mid\nabla\Psi\cdot\boldsymbol{n}+\mathrm{j}\,\eta\,A\,(1-M_0\lambda)^2\Psi = 0\quad\text{on}\,\partial\Omega\big\}\,. \tag{3.2.3}$$

where $\mathcal{C}^2(\Omega)$ is the set of twice continuously differentiable functions on Ω, $\overline{\Omega} = \Omega \cup \partial\Omega$ and $\mathcal{C}^1(\overline{\Omega})$ is the set of functions with bounded and uniformly continuous derivatives on Ω.

Using this notation, the Pridmore-Brown equation with Myers boundary conditions (3.2.1a) in its differential formulation which, from now on, will be referred to as the *strong* formulation in contrast to the weak formulation, can be conveniently written as

$$\mathcal{L}\,[\Psi] = 0\,. \tag{3.2.4}$$

To formulate the variational equivalent of (3.2.4), we multiply both sides by the complex conjugate of an arbitrary function V, called *test* or *weight* function (the properties of which are to be defined) and we integrate the product over Ω. This yields the variational problem

$$a(V,\Psi) = \Big\langle\, V,\, \mathcal{L}\,[\Psi]\, \Big\rangle = 0\,, \tag{3.2.5}$$

where we introduced the familiar notation for the inner product

$$\Big\langle\, V,\, \Psi\, \Big\rangle = \int\limits_{\Omega} V^{*}\Psi \tag{3.2.6}$$

and the asterisk denotes complex conjugation.

Let Ω be a domain such that the Gauss theorem (divergence theorem) is valid, i.e., for any vector field $\boldsymbol{F} : \Omega \mapsto \mathbb{R}^d$ with components in $\mathcal{C}^2(\Omega) \cap \mathcal{C}^1(\overline{\Omega})$ it holds

$$\int\limits_{\Omega} \nabla\cdot\boldsymbol{F} = \int\limits_{\partial\Omega} \boldsymbol{F}\cdot\boldsymbol{n} \tag{3.2.7}$$

where $\boldsymbol{n}$ is the outward-pointing unit normal vector to $\partial\Omega$. Using the product rule for the divergence and gradient operators

$$\nabla\cdot\big[(1-M\lambda)\,V^{*}\,\nabla\Psi\big] = \nabla\big[(1-\lambda M)\,V^{*}\big]\,\cdot\,\nabla\Psi + (1-\lambda M)\,V^{*}\,\nabla^2\Psi \tag{3.2.8}$$

Equation (3.2.5) can be rewritten

$$\int\limits_{\Omega} \nabla\cdot\left[(1-M\lambda)\,V^*\,\nabla\Psi\right]-\int\limits_{\Omega}(1-M\lambda)\,\nabla V^*\cdot\nabla\Psi\,+\eta^2\int\limits_{\Omega}(1-M\lambda)\,\left[(1-M\lambda)^2-\lambda^2\right]\,V^*\,\Psi+$$
$$+\,3\lambda\int\limits_{\Omega}V^*\,(\nabla M\,\cdot\,\nabla\Psi)\;-\mathrm{j}\,\eta\int\limits_{\partial\Omega}A\,(1-M\lambda)^3V^*\,\Psi=0$$

Applying Gauss theorem and boundary conditions one obtains

$$-\int\limits_{\Omega}(1-M\lambda)\,\nabla V^*\,\cdot\,\nabla\Psi\;+\eta^2\int\limits_{\Omega}(1-M\lambda)\,\left[(1-M\lambda)^2-\lambda^2\right]\,V^*\,\Psi+$$
$$+\,3\lambda\int\limits_{\Omega}V^*\,(\nabla M\,\cdot\,\nabla\Psi)\;-\mathrm{j}\,\eta\int\limits_{\partial\Omega}A\,(1-M\lambda)^3\,V^*\,\Psi=0$$

After some manipulations the previous equation is recast as the following

$$a(V,\Psi)\;=a_0(V,\Psi)+\lambda a_1(V,\Psi)+\lambda^2a_2(V,\Psi)+\lambda^3a_3(V,\Psi)=0 \qquad (3.2.9a)$$

where

$$a_0(V,\Psi)=\eta^2\int\limits_{\Omega}V^*\,\Psi\;-\int\limits_{\Omega}\nabla V^*\,\cdot\,\nabla\Psi\;-\mathrm{j}\,\eta\int\limits_{\partial\Omega}A\,V^*\,\Psi \qquad (3.2.9b)$$

$$a_1(V,\Psi)=-\,3\eta^2\int\limits_{\Omega}M\,V^*\,\Psi\;+\int\limits_{\Omega}M(\nabla V^*\,\cdot\,\nabla\Psi\;)+$$
$$+\,3\,\mathrm{j}\,\eta\int\limits_{\partial\Omega}A\,M\,V^*\,\Psi\;+3\int\limits_{\Omega}V^*\,(\nabla M\,\cdot\,\nabla\Psi) \qquad (3.2.9c)$$

$$a_2(V,\Psi)=\eta^2\big(3\int\limits_{\Omega}M^2\,V^*\,\Psi\;-\int\limits_{\Omega}V^*\,\Psi\;\big)-3\,\mathrm{j}\,\eta\int\limits_{\partial\Omega}A\,M^2\,V^*\,\Psi \qquad (3.2.9d)$$

$$a_3(V,\Psi)=-\,\eta^2\big(\int\limits_{\Omega}M^3\,V^*\,\Psi\;-\int\limits_{\Omega}M\,V^*\,\Psi\;\big)+\mathrm{j}\,\eta\int\limits_{\partial\Omega}A\,M^3\,V^*\,\Psi \qquad (3.2.9e)$$

At this point it is worth making some comments. First, notice that the integration by parts has lowered the order of the differential equation by one. Then, formulation (3.2.9a) incorporates the boundary conditions in a natural way, that is the validity of the boundary condition is simply guaranteed by satisfying the variational form. Then, the implicit assumption on the existence of the second derivative in the original strong formulation

(3.2.4) is replaced by a condition of existence of the first derivative in the sense of distributions (generalized functions) in the weak formulation. This fact is of great importance because it allows us to seek approximate solutions within piecewise continuous functions, which belong to $H^1(\Omega)$ but not to $\mathcal{C}^2(\Omega)$.

FEM formulation. Let $\{\Phi_i\}$ be the two-dimensional basis functions for the space $S_h^p(\Omega)$. A finite element approximation for the problem is of the form (cf. equation (3.1.10))

$$\Psi_I(\boldsymbol{a}) = \sum_{i=1}^{N_{\text{glob}}} \hat{\Psi}_i \, \Phi_i(\boldsymbol{a}) \, , \tag{3.2.10}$$

where the coefficients $\hat{\Psi}_i = \Psi(\boldsymbol{a}_i)$ are the unknown values of Ψ at the nodes. Any $V \in S_h^p(\Omega)$ can be written as

$$V(\boldsymbol{a}) = \sum_{j=1}^{N_{\text{glob}}} d_j \, \Phi_j(\boldsymbol{a}) \tag{3.2.11}$$

According to the procedure described in subsection (3.1.2.6), substituting (3.2.10) and (3.2.11) into (3.2.9a), the following algebraic eigenvalue problem is obtained.

$$\left[\mathbf{A}_0 + \lambda\,\mathbf{A}_1 + \lambda^2\,\mathbf{A}_2 + \lambda^3\,\mathbf{A}_3\right] \, \hat{\Psi} = \mathbf{0} \tag{3.2.12a}$$

where

$$\mathbf{A}_0 \quad = \eta^2\mathbf{M}^{(0)} - \mathbf{K}^{(0)} - \mathrm{j}\,\eta\,\mathbf{Z}^{(0)} \, , \tag{3.2.12b}$$

$$\mathbf{A}_1 \quad = -\,3\,\eta^2\mathbf{M}^{(1)} + \mathbf{K}^{(1)} + 3\,\mathrm{j}\,\eta\,\mathbf{Z}^{(1)} + 3\,\mathbf{S} \, , \tag{3.2.12c}$$

$$\mathbf{A}_2 \quad = \eta^2\big(3\,\mathbf{M}^{(2)} - \mathbf{M}^{(0)}\big) - 3\,\mathrm{j}\,\eta\,\mathbf{Z}^{(2)} \, , \tag{3.2.12d}$$

$$\mathbf{A}_3 \quad = -\,\eta^2\big(\mathbf{M}^{(3)} - \mathbf{M}^{(1)}\big) + \mathrm{j}\,\eta\,\mathbf{Z}^{(3)} \, , \tag{3.2.12e}$$

$$M_{ij}^{(k)} = \int_\Omega M^k \, \Phi_j^* \, \Phi_i \, \mathrm{d}\Omega \, , \tag{3.2.12f}$$

$$K_{ij}^{(k)} = \int_\Omega M^k \, \nabla\Phi_j^* \, \cdot \, \nabla\Phi_i \, \mathrm{d}\Omega \, , \tag{3.2.12g}$$

$$Z_{ij}^{(k)} = \oint_{\partial\Omega} A\, M^k \, \Phi_j^* \, \Phi_i \, \mathrm{d}\Gamma \, , \tag{3.2.12h}$$

$$S_{ij} \quad = \int_\Omega \Phi_j^* \, \nabla M \, \cdot \, \nabla\Phi_i \, \mathrm{d}\Omega \, , \tag{3.2.12i}$$

$$\hat{\boldsymbol{\Psi}} \quad = \left[\hat{\Psi}_1,\, \dots\, ,\hat{\Psi}_{N_{\text{glob}}}\right]^T \,. \tag{3.2.12j}$$

The sets of matrices $\left\{\mathbf{M}^{(k)}\right\}_{k=0,\,1,\,2,\,3}$ and $\left\{\mathbf{K}^{(k)}\right\}_{k=0,\,1}$ are Mach-weighted versions of the so-called in literature *mass* and *stiffness* matrices, respectively. Following Gabard & Astley [43], $\left\{\mathbf{Z}^{(k)}\right\}_{k=0,\,1,\,2,\,3}$ and $\mathbf{S}$ are here called *boundary impedance* and *shear coupling* matrices, respectively.

Solving the algebraic eigenvalue problem Equation (3.2.12a) can be expressed as a linear eigenvalue problem of the form

$$\mathbf{A}\boldsymbol{q} = \lambda\mathbf{B}\boldsymbol{q}\,, \tag{3.2.13}$$

where

$$\mathbf{A} = \begin{bmatrix} \mathbf{0} & \mathbf{I} & \mathbf{0} \\ \mathbf{0} & \mathbf{0} & \mathbf{I} \\ -\mathbf{A}_0 & -\mathbf{A}_1 & -\mathbf{A}_2 \end{bmatrix}, \qquad \mathbf{B} = \begin{bmatrix} \mathbf{I} & \mathbf{0} & \mathbf{0} \\ \mathbf{0} & \mathbf{I} & \mathbf{0} \\ \mathbf{0} & \mathbf{0} & \mathbf{A}_3 \end{bmatrix}, \qquad \boldsymbol{q} = \begin{bmatrix} \boldsymbol{u} \\ \lambda\boldsymbol{u} \\ \lambda^2\boldsymbol{u} \end{bmatrix}, \tag{3.2.14}$$

and $\mathbf{0}$ and $\mathbf{I}$ are the square N_{glob} by N_{glob} null and identity matrices, respectively.

The assembling methodology. Calculating the above integrals is the main computation of the finite element method. It is then crucial to adopt a computation methodology that is numerically efficient. For this purpose, consider the mesh $\mathcal{T}_h = \{K_i\}$ of the domain $\overline{\Omega}$ over which the global basis functions $\{\Phi_i\}_{i=1,\dots,N_{\text{glob}}}$ are defined. The idea is to take advantage of the fact that $\operatorname{supp}\Phi_i$ only consists of the elements that contain the i-th node. The integration region is then divided into the elements of the mesh and the integrals (3.2.12f), (3.2.12g), (3.2.12h) and (3.2.12i) are obtained by summing its constituent parts over each element, which are computed separately. For example,

$$M_{ij}^{(k)} \quad = \quad \sum_{e=1}^{N_e} \int\limits_{K_e} M^k\, \Phi_j^*\, \Phi_i \;\mathrm{d}\Omega \;\;, \tag{3.2.15}$$

where N_e is the number of elements. The integrals over each element are nonzero only if nodes i and j lie inside or on the boundary of the e-th element. Making use of the Kronecker's delta $\delta_{i,j}$ and the global-to-local index, this can be mathematically expressed as follows

$$\begin{aligned}\int\limits_{K_e} M^k \, \Phi_j^* \, \Phi_i \, \mathrm{d}\Omega \; &= \delta_{i,n(e,1)}\delta_{j,n(e,1)} M_{1,1}^{(k),e} + \ldots + \delta_{i,n(e,1)}\delta_{j,n(e,N_{\text{en}})} M_{1,N_{\text{en}}}^{(k),e} + \ldots + \\ &+ \delta_{i,n(e,N_{\text{en}})}\delta_{j,n(e,1)} M_{N_{\text{en}},1}^{(k),e} + \ldots + \delta_{i,n(e,N)}\delta_{j,n(e,N_{\text{en}})} M_{N_{\text{en}},N_{\text{en}}}^{(k),e} \qquad (3.2.16)\end{aligned}$$

where N_{en} is the number of element nodes and

$$M_{p,q}^{(k),e} \; = \int\limits_{K_e} M^k \, \Phi_{n(e,q)}^* \, \Phi_{n(e,p)} \, \mathrm{d}\Omega \qquad p,\, q = 1,\, \ldots,\, N_{\text{en}} \qquad (3.2.17)$$

$\left\{M_{p,q}^{(k),e}\right\}_{p,\,q=1,\,\ldots,\,N}$ defines the so-called ***element mass matrix***, corresponding to the e-th element. Each element matrix is computed separately on an element-by-element basis.

3.2.2 Axisymmetric duct: reduction to one-dimensional problem

Variational formulation. If it is assumed that the problem has rotational symmetry, the transversal component of the pressure perturbation, Ψ, can conveniently be represented by a Fourier series expansion in the azimuthal coordinate, θ. Without loss of generality, it is appropriate to seek a solution of the form

$$\Psi(r,\theta) = \psi(r)\, e^{-\mathrm{j}\, m\theta} \,, \qquad (3.2.18)$$

where $\psi(r)$ is the radial component of the pressure perturbation, or radial mode shape,and m is the azimuthal mode number ($m = 0, \pm 1, \pm 2, \ldots$).

This substitution, for a given value of m, into equation (3.2.1a) leads to the following one-dimensional eigenvalue problem for the radial mode shape.

$$\mathcal{L}_m\left[\psi\right] = 0 \tag{3.2.19}$$

where the operator $\mathcal{L}_m$, for each azimuthal mode, m, is defined as

$$\begin{aligned}\mathcal{L}_m\left[\psi\right] \; := \Bigg\{ &(1-M\lambda)\,\frac{\mathrm{d}^2}{\mathrm{d}r^2} + \left[\frac{1-M\lambda}{r} + 2\lambda\,\frac{\mathrm{d}M}{\mathrm{d}r}\right]\frac{\mathrm{d}}{\mathrm{d}r} + \\ &+ (1-M\lambda)\left[\eta^2\left[(1-M\lambda)^2-\lambda^2\right] - \frac{m^2}{r^2}\right]\Bigg\}\,\psi\,. \end{aligned} \tag{3.2.20}$$

Annular duct In the case of annular duct the domain of the operator $\mathcal{L}_m$ is defined as follows

$$\begin{aligned} D\left(\mathcal{L}_m\right) = \Bigg\{ &\psi \in H^1(s,\,1)\,|\, \frac{\mathrm{d}\psi}{\mathrm{d}r} - \mathrm{j}\,\eta\,A_{\text{in}}\,(1-M\lambda)^2\psi = 0 \quad \text{on } r = s\,, \\ &\frac{\mathrm{d}\psi}{\mathrm{d}r} + \mathrm{j}\,\eta\,A_{\text{out}}\,(1-M\lambda)^2\psi = 0 \quad \text{on } r = 1 \Bigg\} \end{aligned} \tag{3.2.21}$$

where $A_{\text{in}} = Z^{-1}(r = s)$ and $A_{\text{out}} = Z^{-1}(r = 1)$ are the specific acoustic admittance values at $r = s$ and $r = 1$, respectively.

The variational formulation of this problem now has the form

$$\begin{aligned}\Big\langle v,\, \mathcal{L}_m\left[\psi\right]\Big\rangle &= a_0'(v,\psi) + \lambda a_1'(v,\psi) + \\ &+ \lambda^2 a_2'(v,\psi) + \lambda^3 a_3'(v,\psi) = 0\end{aligned} \tag{3.2.22a}$$

where

$$\begin{aligned} a_0'(v,\psi) = &\eta^2 \int_s^1 v\,\psi\,r\,\mathrm{d}r \; - \int_s^1 \left(\frac{\mathrm{d}v}{\mathrm{d}r}\frac{\mathrm{d}\psi}{\mathrm{d}r} + \frac{m^2}{r^2}v\psi\right) r\,\mathrm{d}r \; - \\ &- \;\mathrm{j}\,\eta\left[A_{\text{in}}v_{\text{in}}\psi_{\text{in}}s + A_{\text{out}}v_{\text{out}}\psi_{\text{out}}\right] \end{aligned} \tag{3.2.22b}$$

$$a_1'(v,\psi) = \int_s^1 M\left(\frac{\mathrm{d}v}{\mathrm{d}r}\frac{\mathrm{d}\psi}{\mathrm{d}r} + \frac{m^2}{r^2}v\psi\right) r\,\mathrm{d}r \; -$$

$$-3\eta^2\int_s^1 M\,v\,\psi\,r\;\mathrm{d}r\,+$$

$$+\,3\,\mathrm{j}\,\eta\;[A_{\mathrm{in}}\,M_{\mathrm{in}}\,v_{\mathrm{in}}\,\psi_{\mathrm{in}}s+A_{\mathrm{out}}\,M_{\mathrm{out}}\,v_{\mathrm{out}}\,\psi_{\mathrm{out}}]\,+$$

$$+\,3\int_s^1 v\,\frac{\mathrm{d}M}{\mathrm{d}r}\frac{\mathrm{d}\psi}{\mathrm{d}r}\,r\;\mathrm{d}r \tag{3.2.22c}$$

$$a_2'(v,\psi)=\eta^2\big(3\int_s^1 M^2 v\,\psi\,r\;\mathrm{d}r\;-\int_s^1 v\,\psi\,r\;\mathrm{d}r\;\big)$$

$$-\,3\,\mathrm{j}\,\eta\;\big[A_{\mathrm{in}}\,M_{\mathrm{in}}^2\,v_{\mathrm{in}}\,\psi_{\mathrm{in}}s+A_{\mathrm{out}}\,M_{\mathrm{out}}^2\,v_{\mathrm{out}}\,\psi_{\mathrm{out}}\big] \tag{3.2.22d}$$

$$a_3'(v,\psi)=-\,\eta^2\big(\int_s^1 M^3 v\,\psi\,r\;\mathrm{d}r\;-\int_s^1 M\,v\,\psi\,r\;\mathrm{d}r\;\big)+$$

$$+\,\mathrm{j}\,\eta\;\big[A_{\mathrm{in}}\,M_{\mathrm{in}}^3\,v_{\mathrm{in}}\,\psi_{\mathrm{in}}s+A_{\mathrm{out}}\,M_{\mathrm{out}}^3\,v_{\mathrm{out}}\,\psi_{\mathrm{out}}\big] \tag{3.2.22e}$$

and $v_{\mathrm{in}}=v(r=s)$, $v_{\mathrm{out}}=v(r=1)$ and similarly for ψ_{in} and ψ_{out}.

Note that the same expression (3.2.22a) can be obtained from expression (3.2.9a) by considering the following test and trial functions

$$\Psi(r,\theta)\;=\;\psi(r)e^{-\mathrm{j}\,m\theta} \tag{3.2.23a}$$

$$V(r,\theta)\;=\;v(r)e^{-\mathrm{j}\,m\theta}\,. \tag{3.2.23b}$$

FEM formulation. Let $\{\phi_i\}$ be the one-dimensional basis functions for the space $S_h^p([s,1])$. An approximate solution $\psi_I(r)$ can be described by the expansion

$$\psi_I(r)=\sum_{i=1}^{N_{\mathrm{glob}}}\psi_i\,\phi_i(r) \tag{3.2.24}$$

where $\psi_i=\psi(r_i)$. Any $v\in S_h^p([s,1])$ can be written as

$$v(r)=\sum_{i=1}^{N_{\mathrm{glob}}}d_i\,\phi_i(r) \tag{3.2.25}$$

Substituting (3.2.24) and (3.2.25) into (3.2.22a), the finite element approximation for the problem is obtained.

$$\left[\mathbf{A'}_0 + \lambda\,\mathbf{A'}_1 + \lambda^2\,\mathbf{A'}_2 + \lambda^3\,\mathbf{A'}_3\right]\,\hat{\boldsymbol{\psi}} = \mathbf{0} \tag{3.2.26a}$$

where

$$\begin{aligned}
\mathbf{A'}_0 \; &= \eta^2 \mathbf{M}'^{(0)} - \mathbf{K}'^{(0)} - \mathrm{j}\,\eta\,\mathbf{Z}'^{(0)}\;, \\
\mathbf{A'}_1 \; &= -\,3\,\eta^2 \mathbf{M}'^{(1)} + \mathbf{K}'^{(1)} + 3\,\mathrm{j}\,\eta\,\mathbf{Z}'^{(1)} + 3\,\mathbf{S}'\;, \\
\mathbf{A'}_2 \; &= \eta^2\left(3\,\mathbf{M}'^{(2)} - \mathbf{M}'^{(0)}\right) - 3\,\mathrm{j}\,\eta\,\mathbf{Z}'^{(2)}\;, \\
\mathbf{A'}_3 \; &= -\,\eta^2\left(\mathbf{M}'^{(3)} - \mathbf{M}'^{(1)}\right) + \mathrm{j}\,\eta\,\mathbf{Z}'^{(3)}\;, \\
M'^{(k)}_{ij} &= \int_s^1 M^k\,\phi_j\phi_i\,r\;\mathrm{d}r\;, \\
K'^{(k)}_{ij} &= \int_s^1 M^k\left(\frac{\mathrm{d}\phi_j}{\mathrm{d}r}\frac{\mathrm{d}\phi_i}{\mathrm{d}r} + \frac{m^2}{r^2}\phi_j\phi_i\right)\,r\;\mathrm{d}r\;, \\
Z'^{(k)}_{ij} &= \left[A_{\text{in}}\,M^k_{\text{in}}\,\phi_j(s)\,\phi_i(s)\,s + A_{\text{out}}\,M^k_{\text{out}}\,\phi_j(1)\,\phi_i(1)\right]\,, \\
S'_{ij} \; &= \int_s^1 \phi_j\,\frac{\mathrm{d}M}{\mathrm{d}r}\frac{\mathrm{d}\phi_i}{\mathrm{d}r}r\;\mathrm{d}r\;, \\
\hat{\boldsymbol{\psi}} \; &= \left[\hat{\psi}_1,\;\ldots\;,\hat{\psi}_{N_{\text{glob}}}\right]^T\;.
\end{aligned}$$

Element matrices For each element I_e, the element matrices can be calculated

$$M'^{(e,k)}_{pq} = \int_{I_e} M^k \phi_{n(e,q)}\phi_{n(e,p)} r\;\mathrm{d}r\;, \tag{3.2.27}$$

$$K'^{(e,n)}_{pq} = \int_{I_e} M^k\left(\frac{\mathrm{d}\phi_{n(e,q)}}{\mathrm{d}r}\frac{\mathrm{d}\phi_{n(e,p)}}{\mathrm{d}r} + \frac{m^2}{r^2}\phi_{n(e,q)}\phi_{n(e,p)}\right) r\;\mathrm{d}r\;, \tag{3.2.28}$$

$$S'^{e}_{pq} = \int_{I_e} \phi_{n(e,q)}\,\frac{\mathrm{d}M}{\mathrm{d}r}\frac{\mathrm{d}\phi_{n(e,p)}}{\mathrm{d}r}\,r\;\mathrm{d}r\;. \tag{3.2.29}$$

Here p and q are local node numbers, $n(e,\,j)$ is the global-to-local index as defined in Subsection 3.1.2 It is convenient to transform coordinates according to (3.1.16).The formula for a change of variable gives (3.1.16).

$$M'^{(e,n)}_{pq} = \int_{-1}^{1} \left[\hat{M}(\xi)\right]^k N_q(\xi)\, N_p(\xi)\, F(\xi,\, r_i,\, r_j)\, \mathrm{d}\xi \ , \tag{3.2.30}$$

$$K'^{(e,n)}_{pq} = \int_{-1}^{1} \left[\hat{M}(\xi)\right]^k \frac{\mathrm{d}N_q}{\mathrm{d}\xi}\frac{\mathrm{d}N_p}{\mathrm{d}\xi}\, G(\xi,\, r_i,\, r_j)\, \mathrm{d}\xi \ + m^2 \int_{-1}^{1} N_q(\xi)\, N_p(\xi)\, H(\xi,\, r_i,\, r_j)\, \mathrm{d}\xi \ , \tag{3.2.31}$$

$$S'^{e}_{pq} = \int_{-1}^{1} N_q(\xi)\, \frac{\mathrm{d}\hat{M}}{\mathrm{d}\xi}\frac{\mathrm{d}N_p}{\mathrm{d}\xi}\, G(\xi,\, r_i,\, r_j)\, \mathrm{d}\xi \ , \tag{3.2.32}$$

where N_p and N_q are local basis functions on the interval $[-1, 1]$ and

$$\begin{aligned}
\hat{M}(\xi,\, r_i,\, r_j) &= M\left[Q(\xi,\, r_i,\, r_j)\right] = M\left(\frac{r_i + r_j}{2} + \frac{r_j - r_i}{2}\xi\right) \ , & (3.2.33)\\
F(\xi,\, r_i,\, r_j) &= \frac{r_j - r_i}{4}\left[r_i + r_j + (r_j - r_i)\xi\right] \ , & (3.2.34)\\
G(\xi,\, r_i,\, r_j) &= \frac{r_i + r_j + (r_j - r_i)\xi}{r_j - r_i} \ , & (3.2.35)\\
H(\xi,\, r_i,\, r_j) &= G^{-1}(\xi,\, r_i,\, r_j)\ . & (3.2.36)
\end{aligned}$$

These integrals can be obtained by numerical integration.

Cylindrical duct In the case of cylindrical duct the domain of the operator in Equation (3.2.22a) is defined as follows

$$D\left(\mathcal{L}_m\right) = \left\{ \psi \in H^1(0,\, 1)\,|\, \psi = 0 \text{ on } r = 0 \text{ for } m \neq 0, \quad \frac{\mathrm{d}\psi}{\mathrm{d}r} + \mathrm{j}\,\eta\, A_{\text{out}}\,(1 - M\lambda)^2 \psi = 0 \quad \text{on } s = 1 \right\} \tag{3.2.37}$$

The boundary condition on $r = 0$ must be explicitly imposed in the weak form. The space of test and trial functions are therefore

$$\psi = \begin{cases} \{\, \psi \mid \psi \in H^1(0,\, 1)\} & (m = 0) \\ \{\, \psi \mid \psi \in H^1(0,\, 1),\ \psi(0) = 0\,\} & (m \neq 0) \end{cases}$$

$$v = \begin{cases} \{\, v \mid v \in H^1(0,\, 1)\} & (m = 0) \\ \{\, v \mid v \in H^1(0,\, 1),\ v(0) = 0\,\} & (m \neq 0) \end{cases}$$

3.3 The FEM formulation for the convected Helmholtz problem

The present section briefly summarizes key equations for the one-dimensional convected Helmholts problem, which are a particular case of those obtained in the more general formulation of section 3.2.

The strong formulation can be compactly written as

$$\mathcal{L}_m\left[\psi\right] = 0\,, \tag{3.3.1}$$

where the operator $\mathcal{L}_m$ is defined as

$$\mathcal{L}_m\left[\psi\right] := \left\{ \frac{\mathrm{d}^2}{\mathrm{d}r^2} + \frac{1}{r}\frac{\mathrm{d}}{\mathrm{d}r} + \left[\eta^2\left[(1 - M_0\lambda)^2 - \lambda^2\right] - \frac{m^2}{r^2}\right] \right\} \psi\,. \tag{3.3.2}$$

In the case of annular duct, the operator domain is

$$\begin{aligned} D\left(\mathcal{L}_m\right) = \Bigg\{ \psi \in H^1(s,\, 1) \,|\, &\frac{\mathrm{d}u_m}{\mathrm{d}r} - \mathrm{j}\,\eta\, A_{\text{in}}\,(1 - M\lambda)^2\psi = 0 \quad \text{on } r = s\,, \\ &\frac{\mathrm{d}u_m}{\mathrm{d}r} + \mathrm{j}\,\eta\, A_{\text{out}}\,(1 - M\lambda)^2\psi = 0 \quad \text{on } r = 1 \Bigg\}\,. \end{aligned} \tag{3.3.3}$$

Instead, in the case of cylindrical duct, it is

$$D\left(\mathcal{L}_m\right) = \left\{ \psi \in H^1(0,\,1)\,|\,\psi = 0 \text{ on } r = 0 \text{ for } m \neq 0, \right.$$
$$\left. \frac{\mathrm{d}u_m}{\mathrm{d}r} + \mathrm{j}\,\eta\,A_{\text{out}}\,(1 - M\lambda)^2\psi = 0 \quad \text{on } r = 1 \right\}. \tag{3.3.4}$$

Multiplying both sides of equation (3.3.1) by the complex conjugate of an arbitrary complex function, v, and integrating the product over Ω yields, after some manipulations, the variational formulation of this problem

$$a(v,\psi) = \left\langle v,\, \mathcal{L}_\Omega\left[\psi\right] \right\rangle = c_0(v,\psi) + \lambda c_1(v,\psi) + \lambda^2 c_2(v,\psi) = 0 \tag{3.3.5a}$$

where

$$c_0(v,\psi) = \eta^2 \int_s^1 v\psi\, r\, \mathrm{d}r - \int_s^1 \left(\frac{\mathrm{d}v}{\mathrm{d}r}\frac{\mathrm{d}\psi}{\mathrm{d}r} + \frac{m^2}{r^2} v\psi\right) r\, \mathrm{d}r - \tag{3.3.5b}$$

$$- \mathrm{j}\,\eta\left[A_{\text{in}} V_{\text{in}} \psi_{\text{in}} + A_{\text{out}} V_{\text{out}} \psi_{\text{out}}\right], \tag{3.3.5c}$$

$$c_1(v,\psi) = -2M_0\left(\eta^2 \int_s^1 v\,\psi\, r\, \mathrm{d}r - \mathrm{j}\,\eta\left[A_{\text{in}}\, v_{\text{in}}\, \psi_{\text{in}} s + A_{\text{out}}\, v_{\text{out}}\, \psi_{\text{out}}\right]\right),$$

$$c_2(v,\psi) = \eta^2(M_0^2 - 1)\int_s^1 v\,\psi\, r\, \mathrm{d}r - \mathrm{j}\,\eta\, M_0^2\left[A_{\text{in}}\, v_{\text{in}}\, \psi_{\text{in}} s + A_{\text{out}}\, v_{\text{out}}\, \psi_{\text{out}}\right]. \tag{3.3.5d}$$

Let $\{\phi_i\}$ be the one-dimensional basis functions for the space $S_h^p([s,1])$. Substituting an approximate solution $\psi_I(r)$, as described in equation (3.1.10) and any $v \in S_h^p([s,1])$ as written in equation (3.1.25) into (3.3.5a), an algebraic eigenvalue problem for λ is obtained, expressed compactly in the form

$$\left[\mathbf{C}_0 + \lambda\,\mathbf{C}_1 + \lambda^2\,\mathbf{C}_2\right]\hat{\boldsymbol{\psi}} = \mathbf{0} \tag{3.3.6a}$$

where

$$\mathbf{C}_0 = \eta^2\mathbf{M} - \mathbf{K} - \mathrm{j}\,\eta\,\mathbf{Z}, \tag{3.3.6b}$$

$$\mathbf{C}_1 = -2M_0\left(\eta^2\mathbf{M} - \mathrm{j}\,\eta\,\mathbf{Z}\right), \tag{3.3.6c}$$

$$\mathbf{C}_2 = \eta^2 (M_0^2 - 1)\, \mathbf{M} - \mathrm{j}\, \eta\, M_0^2\, \mathbf{Z}\,, \tag{3.3.6d}$$

$$M_{ij} = \int_s^1 \phi_j \phi_i r \; \mathrm{d}r \;, \tag{3.3.6e}$$

$$K_{ij} = \int_s^1 \left(\frac{\mathrm{d}\phi}{\mathrm{d}r} \frac{\mathrm{d}\phi_i}{\mathrm{d}r} + \frac{m^2}{r^2} \phi_j \phi_i \right) r \; \mathrm{d}r \;, \tag{3.3.6f}$$

$$Z_{ij} = \left[A_{\text{in}} \phi_j(s) \phi_i(s)\, s + A_{\text{out}} \phi_j(1) \phi_i(1) \right] \;, \tag{3.3.6g}$$

$$\hat{\boldsymbol{\psi}} = \left[\hat{\psi}_1, \, \ldots \,, \hat{\psi}_{N_{\text{glob}}} \right]^T \;. \tag{3.3.6h}$$

For each element I_e, the element matrices can be calculated

$$M_{pq}^{(e)} = \int_{I_e} \phi_{n(e,q)} \phi_{n(e,p)} r \; \mathrm{d}r \;,$$

$$K_{pq}^{(e)} = \int_{I_e} \left(\frac{\mathrm{d}\phi_{n(e,q)}}{\mathrm{d}r} \frac{\mathrm{d}\phi_{n(e,p)}}{\mathrm{d}r} + \frac{m^2}{r^2} \phi_{n(e,q)} \phi_{n(e,p)} \right) r \; \mathrm{d}r \;,$$

where p and q are the local node numbers, $n(e,\, j)$ is the global-to-local index. Transforming coordinates according to (3.1.16) one obtain

$$M_{pq}^{(e)} = \int_{-1}^1 N_q(\xi)\, N_p(\xi)\, F(\xi,\, r_i,\, r_j) \; \mathrm{d}\xi \;, \tag{3.3.7}$$

$$K_{pq}^{(e)} = \int_{-1}^1 \frac{\mathrm{d}N_q}{\mathrm{d}\xi} \frac{\mathrm{d}N_p}{\mathrm{d}\xi}\, G(\xi,\, r_i,\, r_j) \; \mathrm{d}\xi \; + m^2 \int_{-1}^1 N_q(\xi)\, N_p(\xi)\, H(\xi,\, r_i,\, r_j) \; \mathrm{d}\xi \tag{3.3.8}$$

where N_p and N_q are local basis functions on the interval $[-1, 1]$ and

$$F(\xi,\, r_i,\, r_j) = \frac{r_j - r_i}{4} \left[r_i + r_j + (r_j - r_i)\xi \right] \;, \tag{3.3.9}$$

$$G(\xi,\, r_i,\, r_j) = \frac{r_i + r_j + (r_j - r_i)\xi}{r_j - r_i} \;, \tag{3.3.10}$$

$$H(\xi,\, r_i,\, r_j) = G^{-1}(\xi,\, r_i,\, r_j) \;. \tag{3.3.11}$$

It is possible to evaluate these integrals exactly by symbolic integration (see appendix A).

Equation (3.3.6a) can be expressed as a linear eigenvalue problem of the form

$$\mathbf{A}\boldsymbol{q} = \lambda \mathbf{B}\boldsymbol{q} \, , \tag{3.3.12}$$

where

$$\mathbf{A} = \begin{bmatrix} \mathbf{0} & \mathbf{I} \\ -\mathbf{C}_0 & -\mathbf{C}_1 \end{bmatrix} , \qquad \mathbf{B} = \begin{bmatrix} \mathbf{I} & \mathbf{0} \\ \mathbf{0} & \mathbf{C}_2 \end{bmatrix} , \qquad \boldsymbol{q} = \begin{bmatrix} \boldsymbol{u} \\ \lambda \boldsymbol{u} \end{bmatrix} , \tag{3.3.13}$$

and **0** and **I** are the squareN_{glob} by N_{glob}null and identity matrices, respectively.

3.4 Code verification

3.4.1 Benchmarking

In this subsection, results obtained using the finite element method are compared with some benchmark results to verify the implementation.

3.4.1.1 Case of uniform mean flow

Figure 3.4.1 shows the computed eigenvalues ($\lambda = k_z/\eta$) for the first twelve acoustic eigenmodes, six in each propagation direction and for azimuthal orders $m = 0$ to 3, for a test case with uniform mean flow with Mach number $M = 0.2$ (in the positive direction), with an annular duct having hub-tip-ratio $h = 0.4$. A mesh consisting of 31 nodes and quadratic elements has been used for the FEM calculation. The nodes per wavelength is 22.3, and the (non-dimensional) element size is 0.02. Results in figure 3.4.1(a) are for a rigid duct, and in 3.4.1(b) for a lined duct with specific acoustic impedance $Z = 1.5 - 3\text{j}$. In both examples, the computed eigenvalues may be compared with the 'exact' eigenvalues which are also shown plotted in figure 3.4.1. The ‘exact’ eigenvalues may, in these test cases, be determined from a closed-form analytic solution of the convected wave equation, since the mean flow is uniform. The agreement between the numerical and analytical values is excellent.

3.4.1.2 Case of shear mean flow

Table 3.4.1 and figure 3.4.2 contain results for a shear mean flow. In this example the mean flow is not uniform, due to the inclusion of a boundary layer. The variation of the flow velocity is linear through the boundary layer. Eigenmodes corresponding to azimuthal order $m = 1$ only are shown. A mesh consisting of 75 nodes and linear elements has been used for this calculation. The nodes per wavelength is 55, and the (non-dimensional) element size is 0.008. The propagating modes have been ordered according to increasing values of the imaginary part of the wave number, and are compared to the results of Joshi et al. [62] and also Brooks [23]. The three sets of results compare well for both upstream and downstream propagating modes.

3.4.2 Convergence of the relative error

The purpose of this subsection is to quantify the accuracy of the numerical model by inspecting the convergence of the relative error of the axial wavenumbers, by increasing the number of mesh points. The relative error used here is defined as

$$e = \frac{|\lambda - \lambda_{\text{ref}}|}{|\lambda_{\text{ref}}|} \tag{3.4.1}$$

where λ_{ref} is a reference value obtained numerically with a very high-resolution mesh. The mesh resolution is typically characterized by the number of elements per wavelength

$$n_e = \frac{\lambda_{\text{aco}}}{h} \tag{3.4.2}$$

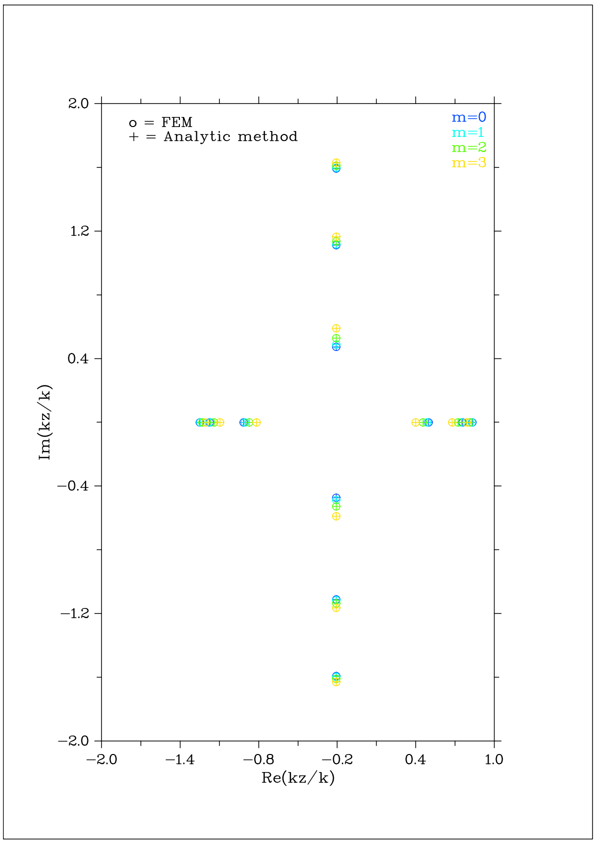

(a) Rigid duct

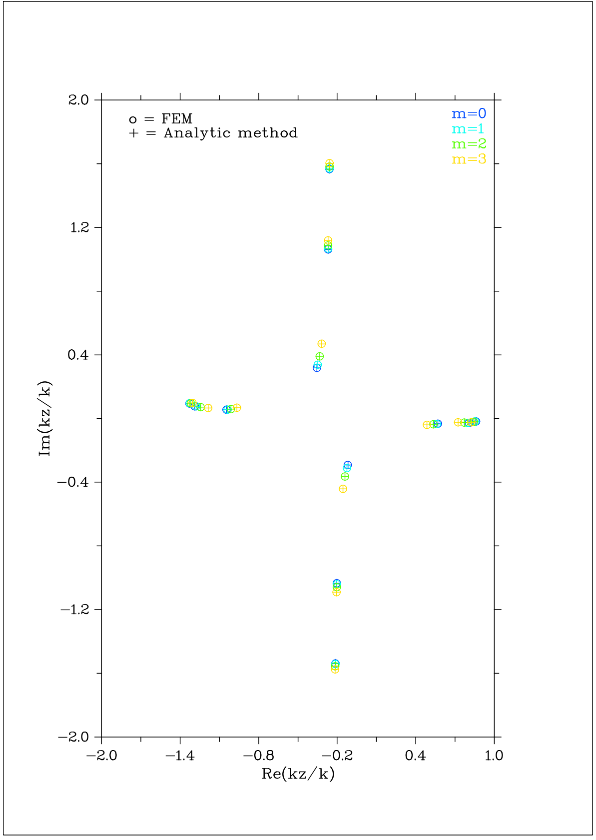

(b) Lined duct

Figure 3.4.1: Comparison between FEM and analytic method. Location of the eigenvalues $\lambda = k_z/\eta$ in the complex plane.

Mode No.	**Joshi et al.**		**Brooks**		**FEM**	
	real	imag.	real	imag.	real	imag.
1+	0.856	-0.020	0.858	-0.020	0.858	-0.020
2+	0.797	-0.026	0.801	-0.027	0.801	-0.027
3+	0.558	-0.034	0.562	-0.034	0.561	-0.034
4+	-0.131	-0.305	-0.125	-0.311	-0.128	-0.311
5+	-0.200	-1.037	-0.205	-1.038	-0.213	-1.039
1-	-1.041	0.054	-1.030	0.056	-1.031	0.057
2-			-1.266	0.069	-1.263	0.069
3-	-1.321	0.080	-1.311	0.081	-1.306	0.080
4-	-0.358	0.328	-0.346	0.336	-0.351	0.335
5-	-0.286	1.059	-0.272	1.063	-0.281	1.064
6-	-0.283	1.558	-0.266	1.562	-0.280	1.565

Table 3.4.1: Eigenvalues $\lambda = k_z/\eta$ for a lined annular duct with hub-to-tip ratio $s = 0.4$, $m = 1$, $\eta = 14.06667$, $Z = 1.5 - 3$j and a linear boundary-layer flow profile. Outside the boundary layer, $M_0 = 0.2$, whilst the (non-dimensional) boundary-layer thickness $\delta = 0.01$. The FEM results are compared to previous results Joshi and Brooks.

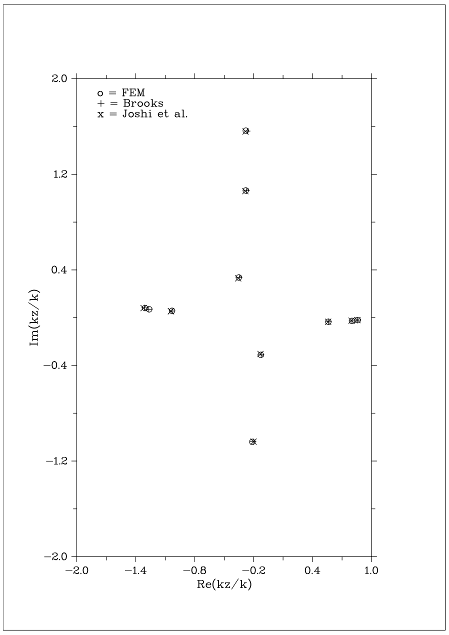

Figure 3.4.2: Location of eigenvalues $\lambda = k_z/\eta$ listed in Table 3.4.1 in the complex plane.

where λ_{aco} is the acoustic wavelength and h is the typical element size in a given mesh. Therefore we define $\eta h = 2\pi/n_e$, where η is the Helmholtz number and h is the non-dimensional element size scaled by the outer duct radius.

Two test cases are considered, which correspond to duct geometries and flow configurations of study 2 in chapter 5 and study 3 in chapter 6. The first test case is that of a lined annular duct with hub-to-tip ratio $s = 0.8$, uniform mean flow $M_0 = 0.5$, non-dimensional specific acoustic impedance $Z = 2 - 3\text{j}$, and Helmholtz number $\eta = 20$. The relative error, e, is plotted as a function of the radial mode order and for different mesh resolutions in figure 3.4.3, and as a function of ηh for a number of prescribed modes in figure 3.4.4.

The second test case is that of a lined cylindrical duct, non-dimensional specific acoustic impedance $Z = 2 + 3.96\text{j}$, and Helmholtz number $\eta = 100$. The mean flow consists of a uniform flow of $M_0 = 0.5$ in the core and a quarter-sine profile in the boundary layer of thickness $\delta = 0.05$. The relative error is plotted as a function of ηh for cut-on modes of azimuthal order $m = 0$, $m = 50$ and $m = 100$ in figure 3.4.5.

As a general trend, the relative error grows as modes of higher radial order are considered. This is expected as the higher the radial order, the resolution of the mode becomes less accurate using the finite element method. Moreover, the relative error reduces systematically for all the modes shown here as ηh is reduced, which can be regarded as a positive verification of the FEM implementation.

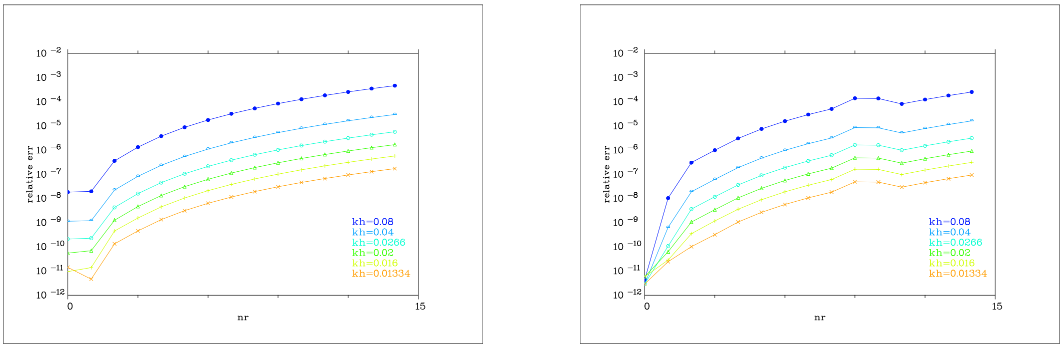

(a) (b)

Figure 3.4.3: Relative error of the calculated axial wavenumbers with different mesh resolutions for the test case of a lined annular duct with uniform flow, $s = 0.8$, $M_0 = 0.5$, $Z = 2 - 3\text{j}$, $\eta = 20$: (a) $m = 0$, negative (upstream) modes, (b) $m = 0$, positive (downstream) modes.

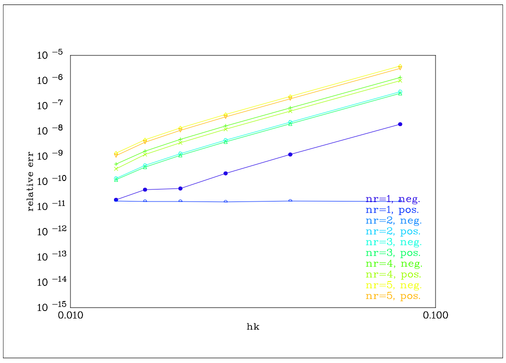

Figure 3.4.4: Convergence of the calculated axial wavenumbers with increased mesh resolution for the test case of a lined annular duct with uniform flow, $s = 0.8$, $M_0 = 0.5$, $Z = 2 - 3\text{j}$, $\eta = 20$. Convergence is shown for positive and negative modes, radial orders $n = 1$ to 5.

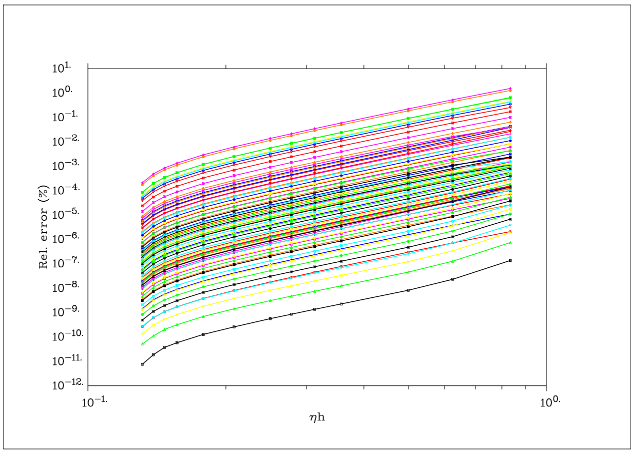

(a) $m = 0$

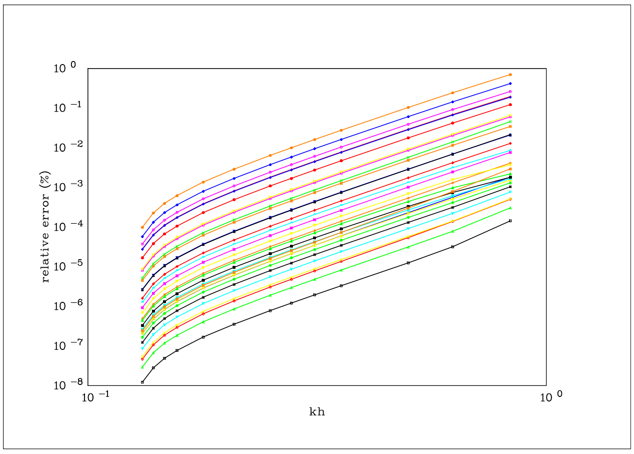

(b) $m = 50$

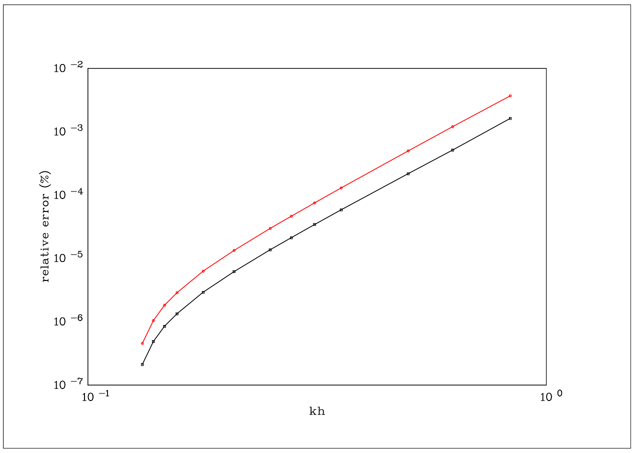

(c) $m = 100$

Figure 3.4.5: Convergence of the calculated axial wavenumbers with increased mesh resolution for the test case of a lined cylindrical duct, $Z = 2 + 3.96\mathrm{j}$, $\eta = 100$. The mean flow consists of a uniform flow of $M_0 = 0.5$ in the core and a quarter-sine profile in the boundary layer of thickness $\delta = 0.05$. Convergence is shown for all cut-on positive and negative modes of azimuthal order: (a) $m = 0$, (b); $m = 50$; (c) $m = 100$.

Chapter 4

The Method of Approximate Equivalent Boundary Condition

This chapter introduces an alternate method to calculate the wavenumber values of small-amplitude pressure modes in an axisymmetric duct with fully developed (axially uniform) unidirectional transversely sheared mean flow parallel to the duct walls.

The method assumes that the mean flow consists of two main regions: (a) uniform core flow; (b) thin but finite boundary layers (of arbitrary profile). This flow assumption, which is necessary to carry out an asymptotic approximation for the acoustic modes, is generally accepted for typical flow engine applications [97].

The method was originally proposed by Eversman & Beckemeyer [39] to determine an 'equivalent' boundary condition for the convected wave equation – which governs the acoustic propagation in the core flow, to be imposed at the edge of core flow region in order to account for the effect of the boundary layer on the propagation of small-amplitude pressure perturbations[1].

The method is extended herein to permit a slip velocity at the duct wall, a feature which is relevant to investigate whether different boundary layer profiles with the same shape

---

[1] The condition was also used to show the validity of the Ingard-Myers boundary condition, which could be resumed from that in the limit of vanishing boundary-layer thickness.

factor affect the propagation of pressure perturbations in a similar way: the shape factor associated with a linear boundary layer profile can be adjusted by varying the mean velocity at the wall.

4.1 Asymptotic expansions and equivalent boundary conditions

In the derivation presented here, the following Pridmore-Brown problem (which is the one-dimensional version of equations 2.5.2 and 2.5.4) is considered:

$$\begin{cases} \psi'' + \left[\dfrac{1}{r} + \dfrac{2\,\lambda\, M\,(r)'}{1-\lambda M\,(r)}\right]\,\psi' + \\ \qquad + \left\{\eta^2\left[(1-M\lambda)^2 - \lambda^2\right] - \frac{m^2}{r^2}\right\}\psi = 0 & \\ \psi' - \jmath\,\eta\,A_{\text{in}}\,\left[1-\lambda M_{\text{in}}\right]^2\psi = 0 & \text{on } r = s, \\ \psi' + \jmath\,\eta\,A_{\text{out}}\,\left[1-\lambda M_{\text{out}}\right]^2\psi = 0 & \text{on } r = 1. \end{cases} \tag{4.1.1}$$

where the dimensionless independent variable, r, is expressed in units of outer radius - a convention adopted throughout the dissertation [2]; s is the hub-to-tip ratio. The prime denotes a derivative to r , $A_{\text{in}} = Z_{\text{spec}}^{-1}$ and $A_{\text{out}} = Z_{\text{spec}}^{-1}$ are the specific acoustic admittance values at $r = s$ and $r = 1$, respectively, and $M_{\text{in}} = M(r = s)$ and $M_{\text{out}} = M(r = 1)$.

The flow profile considered in the present derivation is of the form

$$M(r) = \begin{cases} M_0\,\phi_{\text{in}}(r) & s \leqslant r < r_{\text{in}} = s + \delta_{\text{in}}, \\ M_0 & s + \delta_{\text{in}} \leqslant r \leqslant 1 - \delta_{\text{out}} \\ M_0\,\phi_{\text{out}}(r) & r_{\text{out}} = 1 - \delta_{\text{out}} < r \leqslant 1 \end{cases} \tag{4.1.2}$$

---

[2] Note that in the work by Eversman & Beckemeyer [39] and Eversman [36] the duct height $L = r_{\text{out}} - r_{\text{in}}$ is chosen for nondimensionalization of lengths and distances. Therefore, the Helmoltz number η used in this derivation corresponds to $kL/(1-s)$ in those papers.

in which M_0 is the constant axial mean velocity of the core flow, $\phi_{\text{in}}(r)$ and $\phi_{\text{out}}(r)$ are arbitrary functions for which $\phi_{\text{in}}(s+\delta_{\text{in}}) = \phi_{\text{out}}(1-\delta_{\text{out}}) = 1$, and δ_{in} and δ_{out} are the non-dimensional boundary layer thicknesses at the inner and outer duct walls, respectively. Note that no restrictions are made concerning slip at the wall.

Equation (4.1.1) has singularities at the points $r = r_c$ in the domain of flow where $1 - \lambda M\,(r) = 0$. The study of such singularities, which are commonly referred to as critical layer singularities, is a complex and mathematically very subtle problem (cf., for example, [19, 110, 25]) and it is beyond the scope of the derivation presented here. In the following, it is thus assumed that, for any λ considered, $1 - \lambda M\,(r) \neq 0$.

It is convenient to write equations (4.1.1) in a more suitable form. Making a change of the independent variable, $y = \dfrac{r-s}{1-s}$ and defining $\hat{\psi}\,(y) = \psi\,(r)$ and $\hat{M}\,(y) = M\,(r)$, the problem above becomes

$$\begin{cases} \hat{\psi}'' + \left[\dfrac{1}{y+e} + \dfrac{2\,\lambda\,\hat{M}'\,(y)}{1-\lambda\hat{M}\,(y)}\right]\hat{\psi}' + \\ \qquad + \left\{\eta^2\,(1-s)^2\left[\left[1-\lambda\hat{M}\,(y)\right]^2 - \lambda^2\right] - \dfrac{m^2}{(y+e)^2}\right\}\hat{\psi} = 0, & \\ \hat{\psi}' - \jmath\,\eta\;(1-s)^2\,A_{\text{in}}\;[1-\lambda M_{\text{in}}]^2\,\psi = 0 & \text{on } y = 0, \\ \hat{\psi}' + \jmath\,\eta\;(1-s)^2\,A_{\text{out}}\;[1-\lambda M_{\text{out}}]^2\,\psi = 0 & \text{on } y = 1, \end{cases} \tag{4.1.3}$$

where $e = \dfrac{s}{1-s}$ and m is the circumferential mode number.

Inner expansions for pressure perturbation, $\hat{\psi}$, in the boundary layers close to both the duct inner and outer walls are now considered. Let us obtain, first, asymptotic solutions in the boundary layer region close to the inner wall. To determine an inner solution valid for $0 \leq y \leq \mathcal{O}\,(\delta_{\text{in}})$, let us define $\zeta = \dfrac{y}{\delta_{\text{in}}}$ as the 'stretching' variable, $\xi\,(\zeta) = \hat{\psi}\,(y)$ and $M^*(\zeta) = \hat{M}\,(y)$.

For convenience of notation, let us also introduce the function

$$h(\zeta) = [1 - \lambda\,M^*(\zeta)]^2\ . \tag{4.1.4}$$

The above problem in the neighborhood of $y = 0$ then becomes

$$\begin{cases} \xi'' + \left[\dfrac{\delta_{\text{in}}}{\delta_{\text{in}}\zeta + e} - \dfrac{h'}{h} \right] \xi' \zeta + \\ \qquad + \epsilon_h^2 \left\{ \eta^2 \left(1 - s\right)^2 \left[\gamma_h^2 - \lambda^2 \right] - \dfrac{m^2}{\left(\delta_{\text{in}}\zeta + e\right)^2} \right\} \xi = 0 \\ \xi'(0) - \mathrm{j}\, \delta_{\text{in}} \eta \left(1 - s\right) A_{\text{in}}\, h_{\text{in}}\, \xi(0) = 0 \end{cases} \tag{4.1.5}$$

where

$$h_{\text{in}} = \left[1 - \lambda\, M^*(0)\right]^2 \tag{4.1.6}$$

The inner solution is sought in the form

$$\xi(\zeta) = \xi_0(\zeta) + \delta_{\text{in}}\xi_1(\zeta) + \delta_{\text{in}}^2\xi_2(\zeta) + \mathcal{O}(\delta_{\text{in}}^3)\,, \tag{4.1.7}$$

Substituting the above perturbation series into (4.1.5) and expanding $\left(\delta_{\text{in}}\zeta + e\right)^{-1}$ and $\left(\delta_{\text{in}}\zeta + e\right)^{-2}$ using the property

$$\left(a + b\right)^n = a^n + n\, a^{n-1} b + \frac{n\left(n-1\right)}{2} a^{n-2} b^2 + \ldots \tag{4.1.8}$$

give a sequence of differential problems.

0-th order.

$$\begin{cases} \xi_0'' - 2\, \dfrac{h'}{h}\, \xi_0' = 0 \\ \xi_0(0) = P_0 \\ \xi_0'(0) = 0 \end{cases} \tag{4.1.9}$$

A solution is

$$\xi_0(\zeta) = P_0 \tag{4.1.10}$$

1-st order.

$$\begin{cases} \xi_1'' - 2\,\dfrac{h'}{h}\,\xi_1' = 0 \\ \xi_1(0) = 0 \\ \xi_1'(0) = \mathrm{j}\,\eta\,(1-s)\,A_{\text{in}}\,h_{\text{in}}\,P_0 \end{cases} \tag{4.1.11}$$

A solution is

$$\xi_1(\zeta) = \frac{\mathrm{j}\,\eta\,(1-s)\,A_{\text{in}}}{h_{\text{in}}}\,P_0 \int\limits_0^\zeta h\,(\sigma)\ \mathrm{d}\sigma \tag{4.1.12}$$

2-nd order.

$$\begin{cases} \xi_2'' - 2\,\dfrac{h'}{h}\,\xi_2' + \dfrac{1}{e}\,\mathrm{j}\,\eta\,(1-s)\,A_{\text{in}}\,h\,P_0 = \\ \qquad = -\left\{\eta^2\,(1-s)^2\left[h-\lambda^2\right] - \dfrac{m^2}{e^2}\right\}\,P_0 \\ \xi_2(0) = 0 \\ \xi_2'(0) = \mathrm{j}\,\eta\,(1-s)\,A_{\text{in}}\,h_{in}\,\xi_1(0) \end{cases} \tag{4.1.13}$$

It can be rewritten

$$\begin{cases} \xi_2'' - 2\,\dfrac{h'}{h}\,\xi_2' = \ q(\zeta) \\ \xi_2(0) = 0 \\ \xi_2'(0) = \mathrm{j}\,\eta\,(1-s)\,A_{\text{in}}\,h_{in}\,\xi_1(0) \end{cases} \tag{4.1.14}$$

where

$$q(\zeta) = \left[\beta - h\alpha\right]\,P_0 \tag{4.1.15}$$

$$\alpha = \mathrm{j}\,\frac{\eta\ (1-s)\ A_{\text{in}}}{e} + \eta^2(1-s)^2 \tag{4.1.16}$$

$$\beta_m = \eta^2(1-s)^2\lambda^2 + \frac{m^2}{e^2} \tag{4.1.17}$$

A solution is

$$\xi_2(\zeta) = P_0 \int\limits_0^\zeta h \left\{\beta_m \int\limits_0^\nu \frac{1}{h}\ \mathrm{d}\nu\ - \alpha\sigma\right\}\ \mathrm{d}\sigma \tag{4.1.18}$$

After some manipulation, at the outer edge of the boundary layer, $\zeta = 1$, the following equation, approximated to , is obtained

$$\xi' = \Lambda_m \xi \tag{4.1.19}$$

where

$$\Lambda_m = \frac{(1-\lambda M_0)^2 \left[\mathrm{j}\,\eta\,(1-s)\,A_{\text{in}} + \delta_{\text{in}} \left(\beta_m \int_0^1 \dfrac{1}{h(\nu)}\,\mathrm{d}\nu - \alpha \right) \right]}{1 + \delta_{\text{in}}\mathrm{j}\,\eta\,(1-s)\,A_{\text{in}} \int_0^1 h(\sigma)\,\mathrm{d}\sigma} \tag{4.1.20}$$

By similar means, at the outer edge of the boundary layer close to the duct outer wall the following equation is obtained

$$\Phi' = \tilde{\Lambda}_m \Phi \tag{4.1.21}$$

where

$$\Phi\left(\frac{1-y}{\delta_{\text{out}}}\right) = \hat{\psi}(y) \qquad \text{for } 1 - \mathcal{O}(\delta_{\text{out}}) \le y \le 1 \tag{4.1.22}$$

$$\widetilde{\Lambda}_m = \frac{(1-\lambda M_0)^2 \left[\mathrm{j}\,\eta\,(1-s)\,A_{\text{out}} + \delta_{\text{out}} \left(\widetilde{\beta}_m \int_0^1 \dfrac{1}{\widetilde{h}(\nu)}\,\mathrm{d}\nu - \widetilde{\alpha} \right) \right]}{1 + \delta_{\text{out}}\mathrm{j}\,\eta\,(1-s)\,A_{\text{out}} \int_0^1 \widetilde{h}(\sigma)\,\mathrm{d}\sigma} \tag{4.1.23}$$

$$\tilde{\alpha} = -\mathrm{j}\,\frac{\eta\,(1-s)\,A_{\text{out}}}{1+e} + \eta^2(1-s)^2 \tag{4.1.24}$$

$$\widetilde{\beta}_m = \eta(1-s)^2\lambda^2 + \frac{m^2}{(1+e)^2} \tag{4.1.25}$$

$$\widetilde{h}\left(\frac{1-y}{\delta_{\text{out}}}\right) = \left[1 - \lambda\,\tilde{M}^*\left(\frac{1-y}{\delta_{\text{out}}}\right)\right]^2 \tag{4.1.26}$$

$$\tilde{M}^*\left(\frac{1-y}{\delta_{\text{out}}}\right) = \hat{M}(y) \tag{4.1.27}$$

Within the uniform-flow section, $s + \delta_{\text{in}} \leqslant r \leqslant 1 - \delta_{\text{out}}$, the solutions to equation (4.1.3) are given by $\psi = A\,J_m(\kappa r) + B\,Y_m(\kappa r)$, where $J_m$and Y_m are the Bessel functions of the first and second kind, order m, respectively, and κ is the dimensionless radial wavenumber.

Expressions (4.1.20) and (4.1.23) can be used as boundary conditions for the case of uniform mean flow at $r = s + \delta_{\text{in}}$ and $r = 1 - \delta_{\text{out}}$, respectively. This lead to a linear system of two transcendental eigenvalue equations, whose determinant set to zero provides the eigenvalues, κ,

$$\begin{vmatrix} J'_m\left(\kappa r_{\text{in}}\right) - \mathit{\Lambda}_m J_m\left(\kappa r_{\text{in}}\right) & Y'_m\left(\kappa r_{\text{in}}\right) - \mathit{\Lambda}_m Y_m\left(\kappa r_{\text{in}}\right) \\ J'_m\left(\kappa r_{\text{out}}\right) - \tilde{\mathit{\Lambda}}_m J_m\left(\kappa r_{\text{out}}\right) & Y'_m\left(\kappa r_{\text{out}}\right) - \tilde{\mathit{\Lambda}}_m Y_m\left(\kappa r_{\text{out}}\right) \end{vmatrix} = 0\,. \tag{4.1.28}$$

In the case of a cylindrical duct, only Bessel functions of the first kind, J_m are involved, which are finite on the duct axis. The transcendental eigenvalue equation to solve is

$$J'_m\left(\kappa r_{\text{out}}\right) - \tilde{\mathit{\Lambda}}_m J_m\left(\kappa r_{\text{out}}\right) = 0. \tag{4.1.29}$$

The determination of roots of transcendental functions is a problem commonly encountered in a broad spectrum of engineering applications. There exist a wide variety of root-finding algorithms that are useful for approximating the solution to any desired degree of accuracy. A standard numerical scheme is the Newton-Raphson iteration method, which was employed, for example, by Ko [65]. However the algorithm applied to an eigenvalue problem with multiple roots presents some limitations: convergence to some roots may not be achieved if a nearby starting value is not accurately identified. Recently, Brooks [23] has proposed a robust computational scheme, which uses a combination of tracking techniques of Eversman [37] and Rienstra [108].

It has to be said that, due to the constraints of time, it was not possible to implement a numerical technique, which solves the transcendental determinant equation (4.1.28) or the trascendental equation (4.1.29). In order to obtain anyway some qualitative indication of how closely the method presented here can determine the eigenvalues, λ, a straightforward (though not highly accurate) approach is adopted, which consists of generating a contour plot using computer software. A contour plot displays lines of a constant value (isolines) over a two-dimensional dataset, as in a topographic map. Drawing a contour plot may be useful to find local maxima and minima of real functions of two variables, since, in their proximity, isolines gradually wraps around a hollow core. The accuracy of their determination depends, in general, on the density of the isolines in the surroundings of the maximum or minimum.

The case considered here is that of a cylindrical duct with mean-flow consisting of a uniform flow of Mach number equal to 0.5 in the core and a quarter-sine profile in the boundary layer. The non-dimensional boundary layer thickness is 0.01. The Helmholtz number, η, is equal to 100. $Z = 2 + 3.96\mathrm{j}\,,\ m = 0$. Parameter values are selected to compare results with those obtained previously by the finite element method and presented in study 3 (chapter 6). Figure 4.1.2shows the full set of cut-on modes as a reference. Expressions (4.1.20) and (4.1.23) has been calculated using an off-the-shelf symbolic language manipulator

Figure (4.1.2) showsthe location of the eigenvalues, λ, corresponding to 'cut-on' upstream-propagating acoustic modes determined using the finite element method. Eigenvalues obtained from the perturbation method are the location, in the contour plot, of the minimum points of the following (real) function

$$f(\lambda) = \left| J_m'\left(\kappa r_{\text{out}}\right) - \tilde{\Lambda}_m J_m\left(\kappa r_{\text{out}}\right) \right| \tag{4.1.30}$$

where

$$\kappa(\lambda) = \sqrt{\eta^2\left(1 - M_0\lambda\right)^2 - \lambda^2} \tag{4.1.31}$$

Within the obvious limitations of a visual inspection, the comparison shows a reasonably good agreement of the first dozen of cut-on modes (figure 4.1.1(a)) despite the shear length scale and the acoustic wavelength are comparable. Note that the eigenvalues obtained from the finite element method are very accurate (see convergence study). On the contrary, agreement of higher order cut-on modes of is not as good (see figure 4.1.1(b))

4.2 Summary of the findings

The mathematical technique presented in this chapter provides the basis for a method which could be developed and utilised to evaluate duct modes with a thin boundary layer, based on uniform flow calculations and the notion of equivalent boundary conditions given by analytical expressions. This has the significative advantage that the modes for uniform flow are known analytic solutions of the convected Helmholtz equation, and that greatly simplifies the calculation of the modes. However the associated eigenvalue problem still need to be solved by some numerical technique.

Although the approach was originally proposed by Eversman & Beckemeyer [39], a contribution to new knowledge here is the extension of the method to the case of mean flow with slip at the wall. The advantage of a linear-with-slip profile is that the shape factor can be adjusted to be comparable with other more complicated profile shapes.

A preliminary qualitative comparison between results obtained by this method and the finite element method has been carried out at a very high Helmholtz number. It seems to indicate good agreement, although a more accurate determination of the eigenvalues of equation (4.1.29) would lead to a better assessment. To the best of the author's knowledge, it is the first time that such a comparison has been carried out at very high Helmholtz number.

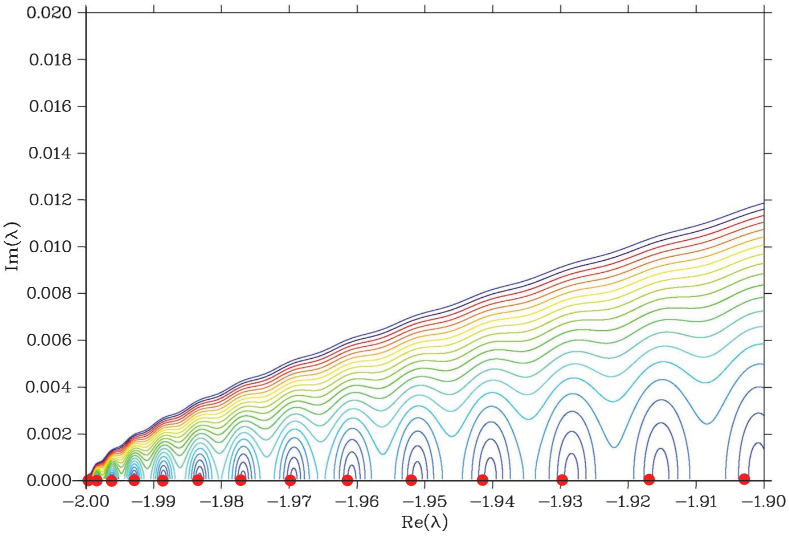

(a)

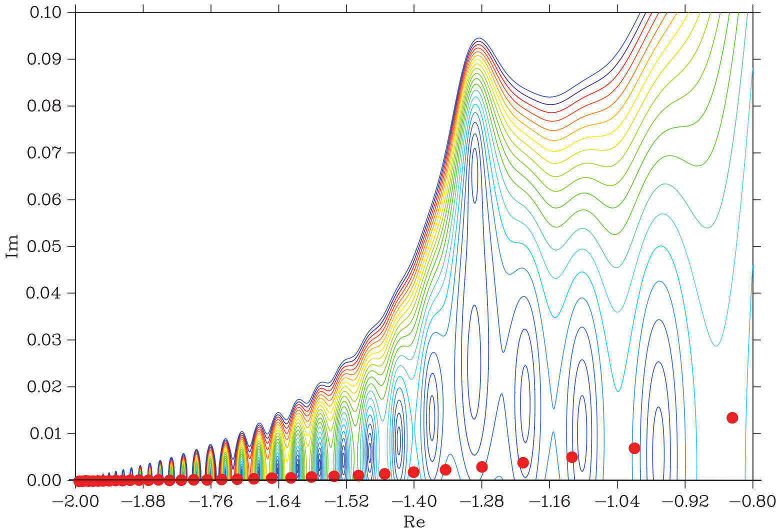

(b)

Figure 4.1.1: Comparison of eigenvalues $\lambda = k_z/\eta$ obtained from perturbation method and the finite element method. Case of a cylindrical duct. The mean-flow consists of a uniform flow of Mach no = 0.5 in the core and a quarter-sine profile in the boundary layer. $\delta_{\text{out}} = 0.01, \eta = 100, Z = 2{+}3.96\text{j}\,, m = 0$. FEM results shown by a red dot. Eigenvalues obtained from perturbation method are the location of the minimum points in the contour plot.

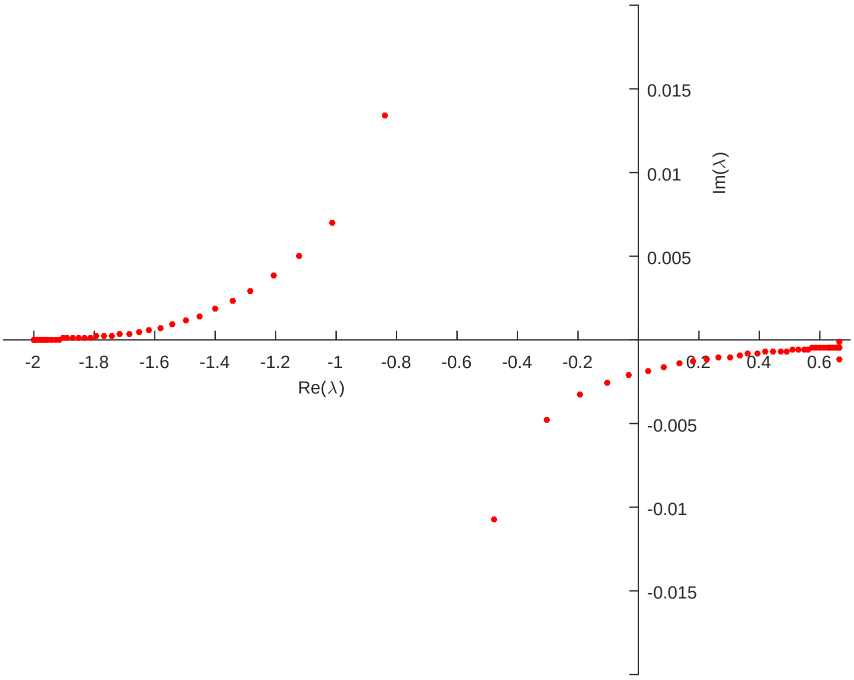

Figure 4.1.2: Location of eigenvalues, λ, in the complex plane corresponding to the full set of cut-on modes, obtained from the finite element method.The case is that of figure 4.1.1.

Chapter 5

Numerical Simulations

This chapter describes examples of numerical simulations, carried out using the numerical analysis tool described in chapter 3 that implements a problem-specific finite element method. The aim is to answer certain questions on the properties of the modal solutions for the sheared mean flow and compare solutions obtained from the Pridmore-Brown equation to those obtained from the convected wave equation.

Study 1 provides evidence of the influence of different shear mean flow profiles on the structure of the modal solutions by comparing the duct modes with different boundary layer profiles.

Of key interest in study 2 is whether boundary layers with similar shape factor (ratio of displacement to momentum thickness) are predicted to have similar pressure modes at high frequencies and, in particular, whether the attenuation determined by the axial decay rates $\mathrm{Im}(\lambda)$ of these modes are comparable. If that is confirmed, at least for a range of non-dimensional boundary layer thicknesses, it would be possible to model any arbitrary boundary layer profile just using a linear boundary layer with slip at the wall, whose shape factor can be adjusted by varying the wall velocity. This investigation was inspired by a paper by Nayfeh et al. [90].

A typical acoustic liner used in aero-engine ducts is formed from a single sandwich panel consisting of a porous facing sheet and a hard-wall backing sheet bonded to a small honeycomb array of air-filled cavities. A simple mathematical model for the locally-reacting acoustic impedance of that type of liner can be built modelling the facing sheet as a single-degree-of-freedom mass-spring-damper system, and the cavities as Helmholtz resonators (see, for example, [109]) . This yields the following expression

$$\tilde{Z}\left(\tilde{\omega}\right) = \left[\tilde{R}_{\mathrm{FS}} + \jmath\,\tilde{\omega}\,\tilde{m} - \jmath\,\rho_0 c_0 \cot\left(\frac{\tilde{\omega}\,\tilde{d}}{c_0}\right)\right] , \tag{5.0.1}$$

where $\tilde{R}_{\mathrm{FS}}$ is the facing sheet resistance, $\tilde{\omega}\,\tilde{m}$ is the facing sheet mass reactance. The term $-\jmath\,\rho_0 c_0 \cot\left(\frac{\tilde{\omega}\,\tilde{d}}{c_0}\right)$ represents the impedance of the air cavity, where $\tilde{d}$ is the cell depth (all dimensional quantities). The same expression, in terms of the nondimensional quantities, may be written as

$$Z\left(\eta\right) = \left[R_{\mathrm{FS}} + \jmath\,\eta\,\frac{\tilde{m}/\rho_0}{\tilde{a}} - \jmath\cot\left(\eta\,d\right)\right] , \tag{5.0.2}$$

where $Z\left(\eta\right) = \tilde{Z}/\rho_0 c_0$ represents the ratio of the specific acoustic impedance of the surface to the characteristic impedance of the medium, $R_{\mathrm{FS}} = \tilde{R}_{\mathrm{FS}}/\rho_0 c_0$, and $d = \tilde{d}/\tilde{a}$ where $\tilde{a}$ is the outer duct radius.

The parameters $\tilde{R}_{\mathrm{FS}}$ and $\tilde{m}$ are typically determined experimentally. They depend on the physical construction of the facing sheet (porosity, thickness and hole size). Moreover, $\tilde{R}_{\mathrm{FS}}$ is generally influenced by the mean grazing flow over the surface and the sound pressure amplitude, and $\tilde{m}$ varies both with $\tilde{R}_{\mathrm{FS}}$ and the grazing flow (see, for example, reference[7]). A discussion of the validity and limitations of this impedance model is however outside of the scope of this work. In all of the numerical simulation presented in this chapter and in chapter 6, the values $R_{\mathrm{FS}} = 2$ and $\tilde{m}/\rho_0 = 2.5\mathrm{cm}$ have been assumed as typical values from aeronautical applications, as affirmed by Rienstra & Darau [110].

However, it is noted that, in reference [110], a low-Mach-number mean flow ($M_0 = 0.17$) was considered. In the work presented here, the same two values have been used for a number of mean flows in a higher-Mach-number flow condition ($M_0 = 0.5$), under the assumption that they would not change significantly. Values of the non-dimensional specific acoustic impedance, Z, were then determined from equation (5.0.2) by inserting the non-dimensional frequency, η, and arbitrary (though typical) values for the quantities $\tilde{a}$ and d .

The numerical simulations results which are presented in this chapter have previously been published in two conference articles: the results of the first and second study have been reported in references [94] and [95], respectively, with the exception of the summary of the findings and the considerations offered in the last section of this chapter. It has to be explained that, since the presentation of paper [2], a coding error in the calculation of the solution of the eigenproblem related to the 1/7th power law shear profile case has been detected and corrected. The error was introduced somehow during code refactoring between the presentation of the first and the second paper. After correction, new sets of data for that particular case have been generated and reported herein. This has resulted in some changes in the interpretation of the results associated to the 1/7th power law shear profile.

5.1 Study 1: Effect of mean flow non-uniformity on the modal structure

An annular duct with hub-to-tip ratio $s = 2/3$ is used for the examples in this section. The duct wall is lined having specific acoustic impedance $Z = 2 - 0.5\mathrm{j}$. The frequency corresponds to Helmholtz number $\eta = 30$. The eigenmodes have been computed for three different mean-flow profiles

1. Uniform flow;
2. Linear boundary-layer of thickness $\delta = 0.03$;
3. 1/7th power law boundary-layer also of thickness $\delta = 0.03$.

The flow profiles for the shear flow test cases are

$$M(r) = \begin{cases} M_0\left(\dfrac{r-s}{\delta}\right)^{1/N} & s \leqslant r < s+\delta, \\ M_0 & s+\delta \leqslant r \leqslant (1-\delta) \\ M_0\left(\dfrac{1-r}{\delta}\right)^{1/N} & (1-\delta) < r \leqslant 1 \end{cases} \tag{5.1.1}$$

where $M_0 = 0.3$ is the core flow Mach number, and N defines the power ($N = 1$ for case (2), $N = 7$ for case (3)). In all three cases a one-dimensional mesh consisting of 75 nodes has been used. The nodes per wavelength is 46.5, and the (non-dimensional) element size is 0.0045. Quadratic element shape functions are used for cases (1) and (3) – uniform flow and 1/7th power law boundary layer flow. Linear element shape functions are used for case (2) – linear boundary layer flow.

Mode No.	**Uniform**		**Linear**		**1/7th power law**	
	real	imag.	real	imag.	real	imag.
1+	0.762254	-0.0298238	0.767216	-0.0429713	0.752477	-0.0385387
2+	0.720099	-0.0666787	0.735697	-0.0857692	0.710757	-0.0959106
3+	0.574907	-0.0867974	0.587065	-0.0985904	0.580324	-0.119471
4+	0.238579	-0.164771	0.236721	-0.176683	0.238334	-0.188594
5+	-0.168087	-0.635233	-0.181914	-0.657412	-0.172457	-0.680591
6+	-0.254177	-1.13849	-0.266665	-1.16711	-0.247567	-1.1805
1-	-1.38066	0.0228141	-1.38276	0.013392	-1.3935	0.0280103
2-	-1.24982	0.120678	-1.25528	0.0746442	-1.31762	0.102902
3-	-1.12519	0.270276	-1.10397	0.184008	-1.19124	0.170892
4-	-0.89105	0.378465	-0.85227	0.288935	-0.891667	0.242585
5-	-0.520351	0.805449	-0.501949	0.725359	-0.498628	0.720267
6-	-0.435734	1.28972	-0.43552	1.19818	-0.432423	1.21014

Table 5.1.1: Eigenvalues λ for a lined annular duct with hub-to-tip ratio $s = 2/3$, $m = 0$, $\eta = 30$, $Z = 2.0 - 0.5\mathrm{j}$ and flow profiles: (1) Uniform flow; (2) Linear boundary-layer; (3) 1/7th power law boundary-layer. Outside the boundary layer, $M_0 = 0.3$, whilst the (non-dimensional) boundary-layer thickness $\delta = 0.03$.

The computed eigenvalues ($\lambda = k_z/\eta$) for the first twelve acoustic eigenmodes, six in each propagation direction and for azimuthal order $m = 0$, are shown in table 5.1.1

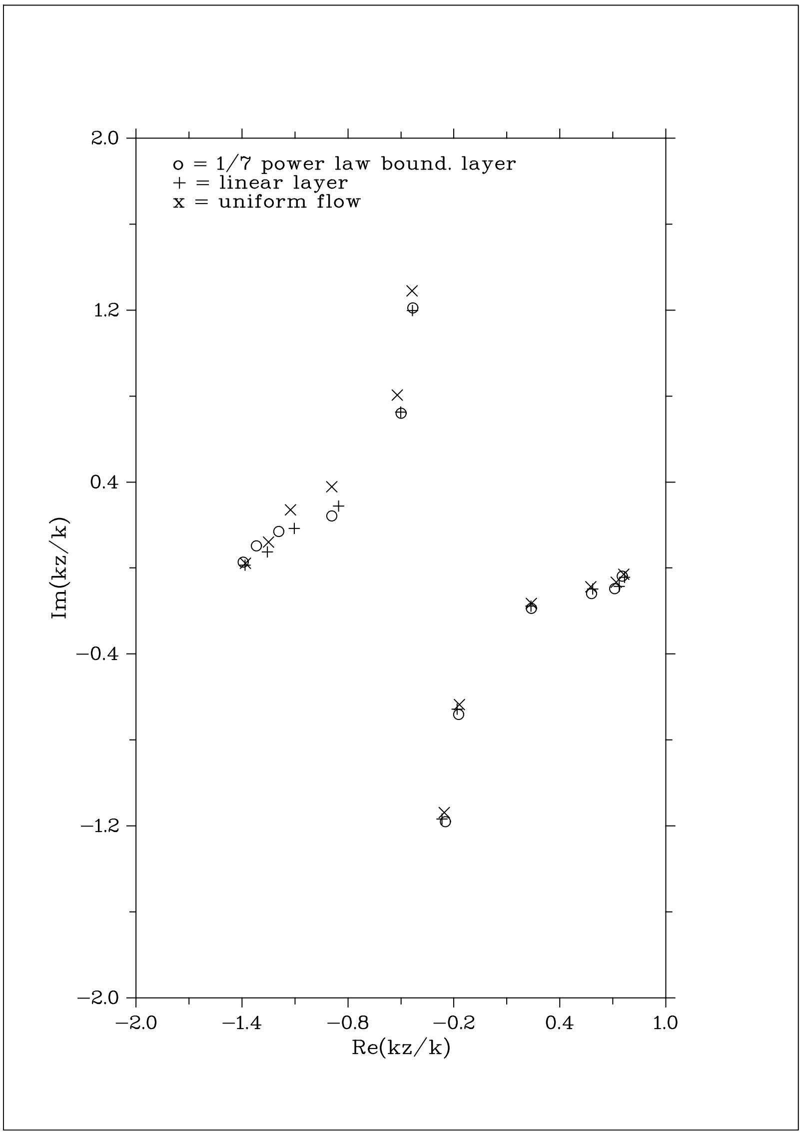

Figure 5.1.1: Location of eigenvalues λ listed in Table 5.1.1 in the complex plane.

and in figure 5.1.1. In figure 5.1.2 the computed eigenvalues are shown plotted (for the 1/7th power law boundary layer). It is seen that there are two families of acoustic modes (propagating in the positive and negative z-direction). There are also a number of modes which have real and positive eigenvalues. These are identified as being modes predominantly convected with the mean flow. The number of the latter depend on the number of nodes in the mesh, since the problem has been discretized. In reality they

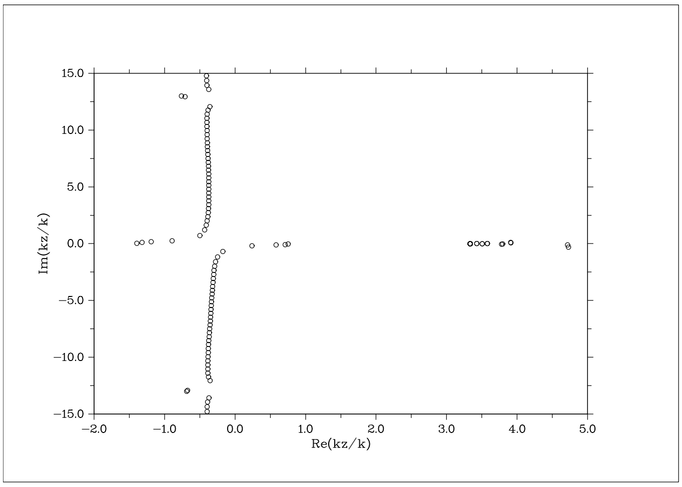

Figure 5.1.2: Location of the computed eigenvalues $\lambda = k_z/\eta$ for the 1/7th power law boundary-layer in the complex plane. The real and positive eigenvalues on the far right of the plot are modes predominantly convected with the mean flow.

may constitute a continuous spectrum [1].

The results illustrate the effect of a boundary layer on sound attenuation compared with a uniform flow. There are small differences in the imaginary part of the axial wave number. The notable differences are for the modes propagating against the flow. For these modes, generally, with uniform flow the axial decay rates are slightly higher compared to the decay rates with a boundary layer. This is because the sheared flow causes the upstream propagating modes to be refracted towards the centre of the duct, leading to lower pressure at the duct walls. The first radial order, which typically will be the least attenuated mode, is seen to be the most affected by the type of flow profile, as shown in figure 5.1.3 where a selection of mode shapes are plotted. This is significant for noise control because it is the least attenuated mode. Higher radial orders appear less affected by a boundary layer.

It is worth noting that the mode shapes are non-symmetric about the mid-point with respect to the duct's height, $H = 1 - s$ (non-dimensional). This is because there is no symmetry in the problem about the duct's mid-point. For example, the mass flow

---

[1] The existence of a continuous spectrum of coupled acoustic-vortical modes in inviscid unidirectional shear mean flows is associated with the presence of a critical layer, that is, a region where the local mean flow velocity is equal to the phase speed of the disturbance. This is a current subject of research in Applied Mathematics. See, for example, references [19][24].

between $r = s$ and $r = s + H/2$ is different to the mass flow between $r = 1 - H/2$ and $r = 1$, owing to the circular geometry.

If the hub-to-tip ratio, s, tends to 1, an approximation of the modal solutions may be obtained by replacing the annulus by a narrow rectangular duct, whose height equals H and width equals the average circumference of the annulus. In this case, with the same lining on each wall, the rectangular duct problem is symmetric, and the mode shapes are symmetric about the mid-point with respect to the duct's height. A study on the approximation of modal solutions in an annular duct using a narrow rectangular duct model at increasing hub-to-tip ratio is provided by Brooks [23].

5.2 Study 2: Use of a linear profile with slip as an approximation to any profile

A rigid and an acoustically-lined annular duct with hub-to-tip ratio $s = 0.8$ are used for the examples in this section. The frequency corresponds to Helmholtz number $\eta = 20$. In the case of the lined duct, results are provided for a locally-reacting acoustic lining with (non-dimensional) specific acoustic impedance $Z = 2 - 3\mathrm{j}$. The eigenmodes have been computed for three different mean-flow profiles: (a) uniform flow; (b) linear boundary-layer; (3) $1/7$th power law boundary-layer. The flow profiles for the shear flow test cases are defined in equation 5.1.1 of section 5.1. The linear boundary layer profile can be adjusted by permitting a slip velocity at the wall. This requires a slight modification:

$$M(r) = \begin{cases} M_0 \left[\dfrac{M_{\text{slip}}}{M_0} + \left(1 - \dfrac{M_{\text{slip}}}{M_0}\right) \dfrac{r - s}{\delta} \right] & s \leqslant r < s + \delta, \\ M_0 & s + \delta \leqslant r \leqslant (1 - \delta) \\ M_0 \left[\dfrac{M_{\text{slip}}}{M_0} + \left(1 - \dfrac{M_{\text{slip}}}{M_0}\right) \dfrac{1 - r}{\delta} \right] & (1 - \delta) < r \leqslant 1 \end{cases} \tag{5.2.1}$$

where M_{slip} is the duct wall Mach number, $0 \leq M_{\text{slip}} \leq M_0$. In all the results the uniform flow is taken to be $M_0 = 0.5$.

For each test case, the eigenvalues, λ, are shown plotted on an Argand diagram. Only the acoustic modes are shown (the continuous spectrum of modes predominantly convected with the mean flow is not shown). Both downstream and upstream propagating modes are shown. Varying the velocity at the duct wall allows the shape factor of the profile to be altered, whilst keeping the boundary-layer thickness fixed. Accordingly, in all the following test cases, each boundary-layer profile has the same thickness δ, but two linear boundary-layer profiles are assessed. One profile has no slip at the wall, whilst the other profile has a slip velocity such that the linear with slip boundary-layer profile has the same shape factor as the $1/7$th power law boundary layer. This allows comparisons to be made between two different profiles having matching thickness and/or matching shape factor as well. Results are provided taking the non-dimensional boundary layer thickness to be $\delta = 0.01$ (1 % of duct outer radius) and $\delta = 0.05$ (5 % of of duct outer radius).

The eigenvalues λ for a rigid and a lined annular duct are shown in figures 5.2.1 and 5.2.2, respectively, for boundary-layer profiles with thickness $\delta = 0.01$, and in figures 5.2.3 and 5.2.4, respectively, for profiles with thickness $\delta = 0.05$. Modes having circumferential order $m = 0$ and $m = 10$ are shown.

Some examples of the pressure mode shapes $\psi(r)$ are plotted in figures 5.2.5 and 5.2.6 for boundary-layer profiles with thickness $\delta = 0.01$, and in figures 5.2.7 and 5.2.8 for boundary-layer profiles with thickness $\delta = 0.05$. These show the positive and negative modes with circumferential order $m = 0$, and radial orders $n = 1$ and 2.

There are several features which can be observed in these results, and warrant further investigation. In figures 5.2.1 to5.2.4 it is seen that the inclusion of a boundary layer alters the eigenvalues, and unsurprisingly there is greater variation with the thicker boundary-layer profile. There are no clear trends evident when comparing the eigenvalues for the different profiles, albeit there is slightly more variation in the values of λ with the upstream propagating modes. Conversely, in the rigid duct, the values of λ for the downstream propagating (cut-on) modes are very similar for each of the different boundary-layer profiles.

The other notable feature in these results is that with the $1/7$th power law boundary layer profile in the lined duct, the upstream propagating cut-on modes have attenuation rate, $\mathrm{Im}(\lambda)$, similar to those of the linear-without-slip profile for $\delta = 0.01$ and of the linear-with-slip profile for $\delta = 0.05$.

In figures 5.2.7 to 5.2.8 there are comparisons of some low-order pressure mode shapes (eigenfunctions $\psi(r)$) with circumferential order $m = 0$. As expected the largest variation in the mode shapes occur for $n = 1$. In the rigid duct, $(m, n) = (0, 1)$ is the plane wave mode in the uniform mean-velocity profile. The inclusion of a boundary layer means that this mode shape is not planar, hence the seemingly large variation in the eigenfunctions for this mode order, which is more evident for the upstream propagating mode and is greater with the thicker boundary-layer profile. There is less variability in radial order $n = 2$, although as already noted the variability is greater with theupstream propagating modes.

Moreover, similarly to the trend noted for the attenuation rate, , it is seen that for these low-order modes in the lined duct the $1/7$th power law boundary layer have similar mode shapes to those of the linear-without-slip boundary layer for $\delta = 0.01$, whilst to those of the linear-with-slip boundary layer for $\delta = 0.01$.

5.3 Summary of the findings

In this chapter, the results of two different studies on the acoustic propagation in annular ducts using the finite element method have been presented. In each study, two different frequencies, annular duct geometries, Mach-number mean flows and surface acoustic impedance values were chosen, which were believed to be representative of modern aero-engine applications. Each study had a different aim, which will be summarised in the following.

The first study aimed to investigate the influence of a finite boundary layer thickness on the mode attenuation rate. A number of key theoretical studies on the effect of the presence of shear flow in the mean boundary layer on the modal solutions were published between late 1960's and early 1970's ([113] [81] [82] [65] [66] [34] [35][117] [89]). At that time, high-bypass-ratio turbofan engines were just about to be developed and the primary interest of acousticians was focussed on relatively low frequencies (corresponding to Helmholtz number less than about 20) . Nevertheless, the limited computing resources available at the time typically allowed the calculation of the least attenuated modes only. Since then, with the very rapid progress of computational capability, there appears to have been less of this type of analysis, probably due to the shift of interest towards the new analysis possibilities associated with applying CFD/CAA methods.

The study carried out here revisited the topic, but considering a higher frequency (corresponding to Helmholtz number η =30), which is an appropriate example for acoustic propagation studies of modern high-bypass-ratio engines.

The analysis quantified the impact of two simple shear boundary-layer profiles which have been often used in the literature: the linear and 1/7th power law profiles. It confirmed, for the particular case considered, the findings of those early studies: a decrease (compared to the uniform flow case) in the attenuation rate of the upstream-propagating modes and an increase of the downstream-propagating ones. A point to be noted from the analysis is that the effect is noticeable only in the case of upstream propagation (a change in the second decimal place of λ for cut-on modes).

The second study offered further examples of the general trend mentioned above. More importantly, it provided an investigation into the presumed dependency of attenuation rate of upstream-propagating modes on the shape factor of a boundary layer. The study provided a comparison of modal solutions for the 1/7th power law and linear-with-slip boundary-layer profile at equal boundary-layer thickness and shape factor for two different values of boundary-layer thickness.

In the case of a lined duct, the numerical analysis revealed notable discrepancies between the corresponding attenuation rate values of cut-on modes. The conclusion drawn from the analysis is that the method of estimating the attenuation rate of (cut-on) upstream propagating modes by approximating an arbitrary boundary layer profile with a convenient linear-with-slip profile having matching thickness and shape factor cannot be generalised to any case. The study provided evidence that, at high frequencies, for the particular case considered of a 1/7th power law boundary layer profile, which is the most relevant one for modelling a turbulent boundary layer, modelling this with a linear-with-slip profile is not appropriate.

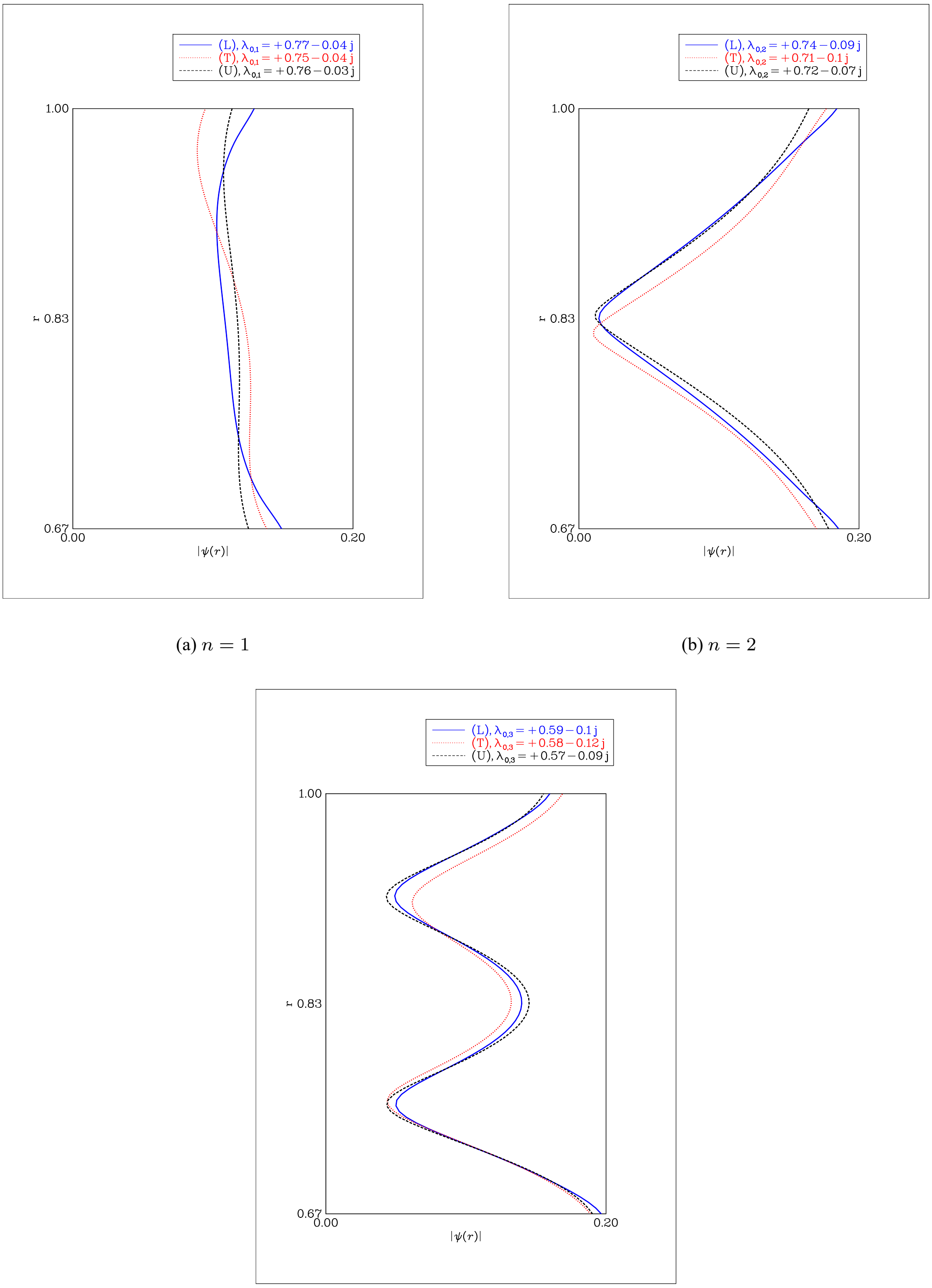

(a) $n = 1$

(b) $n = 2$

(c) $n = 3$

Figure 5.1.3: Mode shapes $\psi(r)$ of upstream-propagating modes listed in Table 5.1.1 corresponding to radial order n =1, 2 and 3. Mode shapes are shown for different flow profiles: (L) linear boundary layer (without slip); (T) 1/7th power law boundary layer; (U) uniform flow.

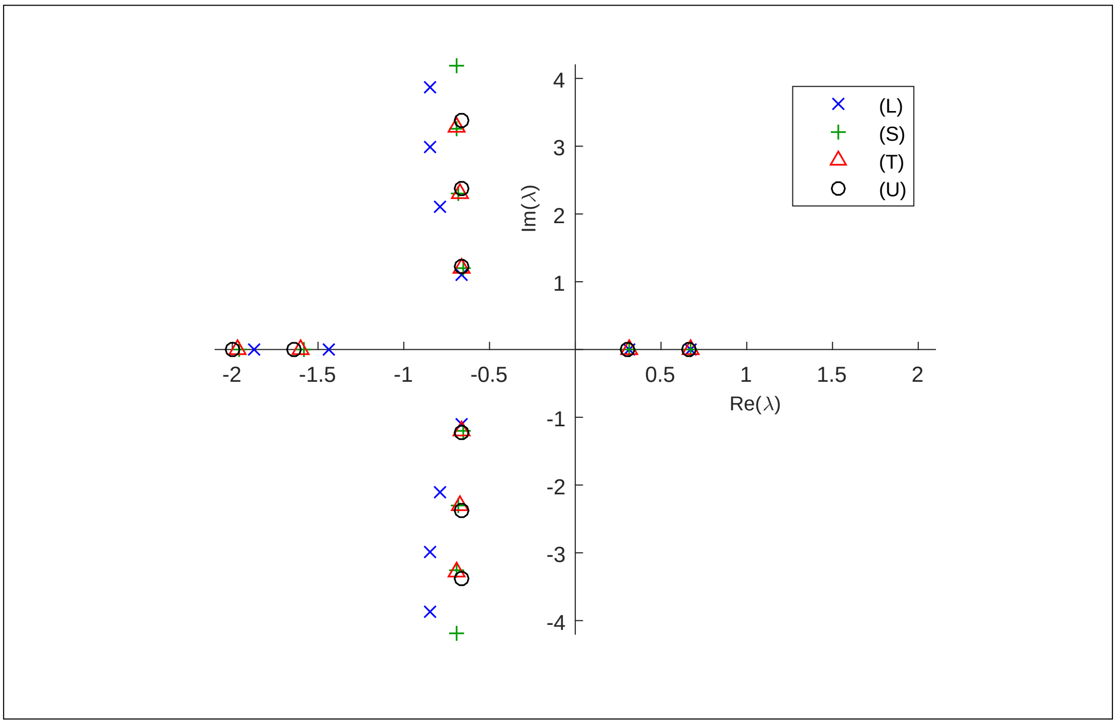

(a) $m = 0$.

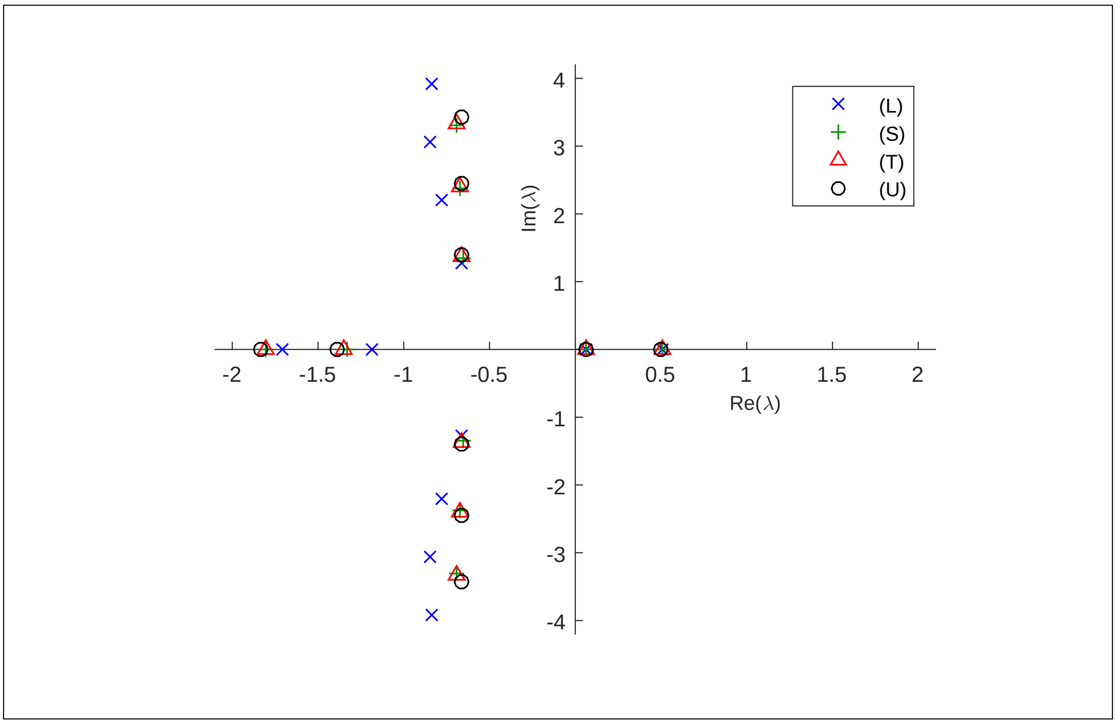

(b) $m = 10$.

Figure 5.2.1: Eigenvalues λ for a rigid annular duct ($s = 0.8$, $M_0 = 0.5$, $\delta = 0.01$,$\eta = 20$) with mean flow profiles: (L) linear boundary layer without slip; (S) linear boundary layer with slip; (T) 1/7th power law boundary layer; (U) uniform flow.

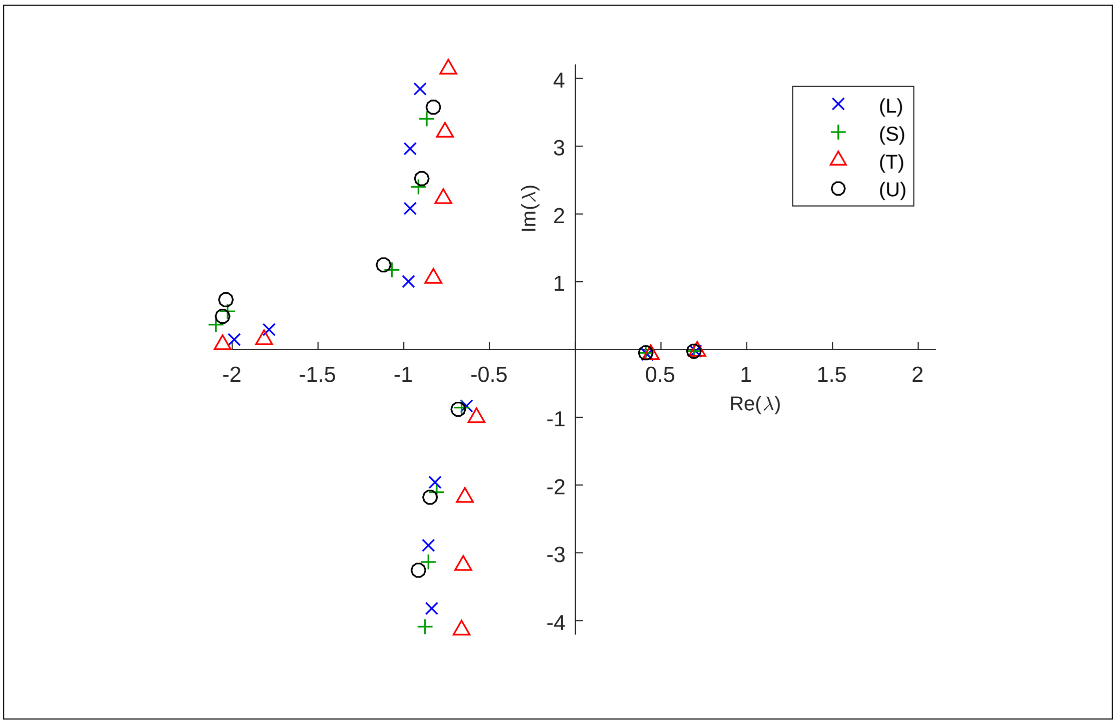

(a) $m = 0$.

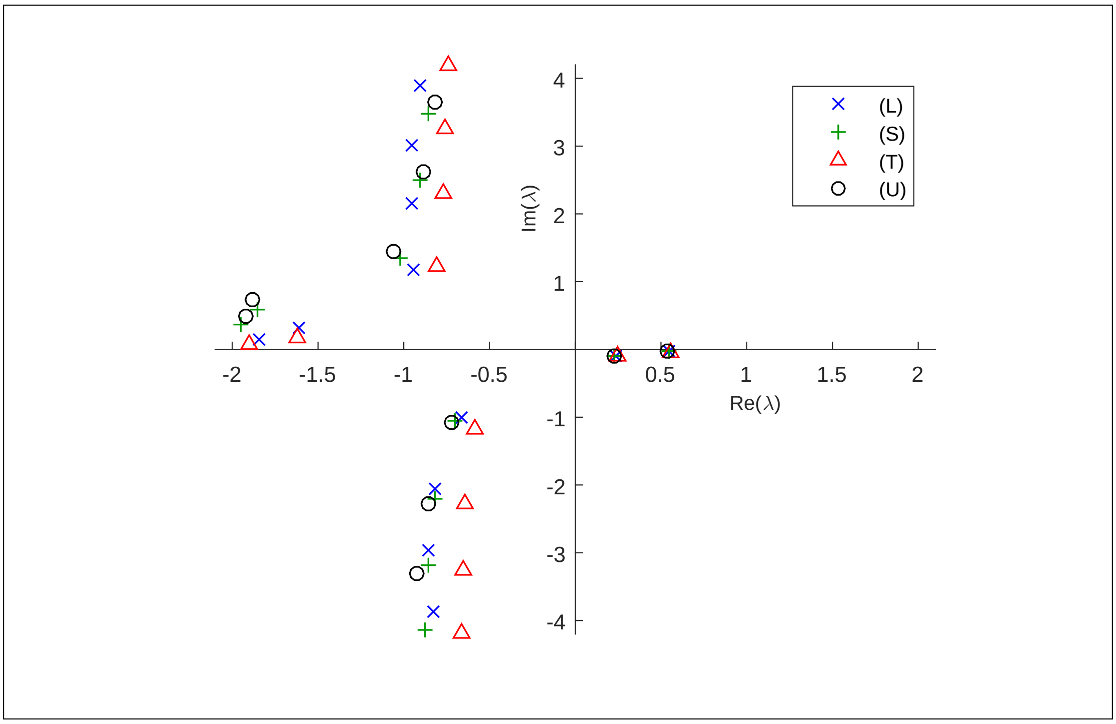

(b) $m = 10$.

Figure 5.2.2: Eigenvalues λ for a lined annular duct ($s = 0.8$, $M_0 = 0.5$, $\delta = 0.01$,$\eta = 20$, $Z = 2 - 3\mathrm{j}$) with mean flow profiles: (L) linear boundary layer without slip; (S) linear boundary layer with slip; (T) 1/7th power law boundary layer; (U) uniform flow.

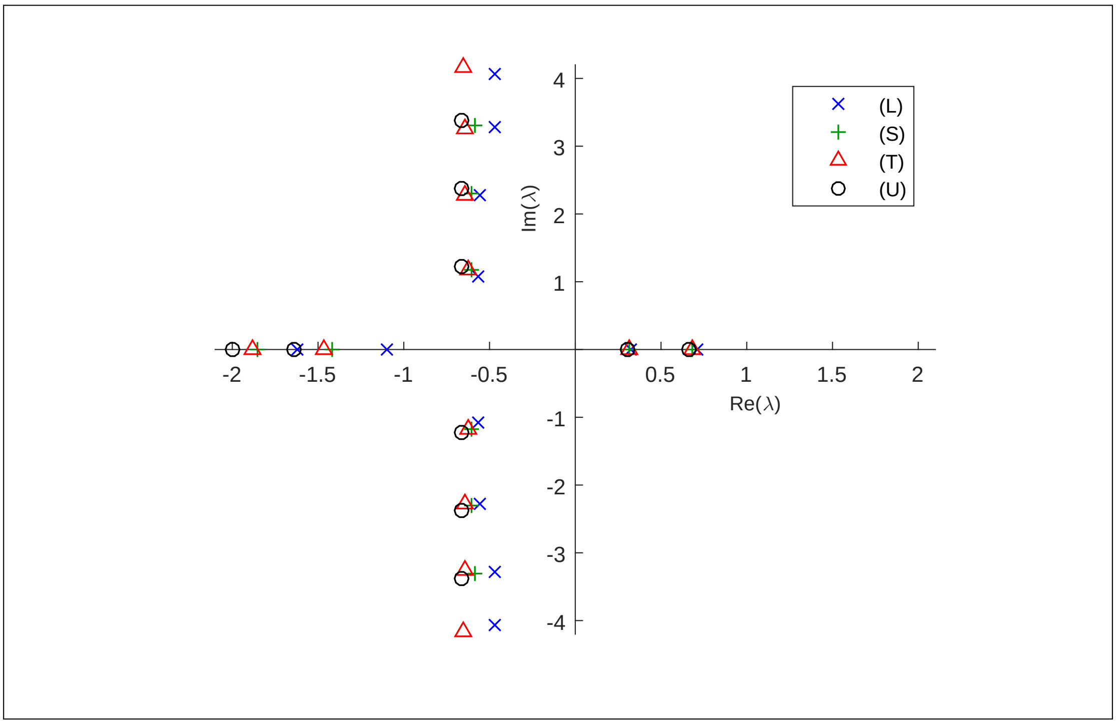

(a) $m = 0$.

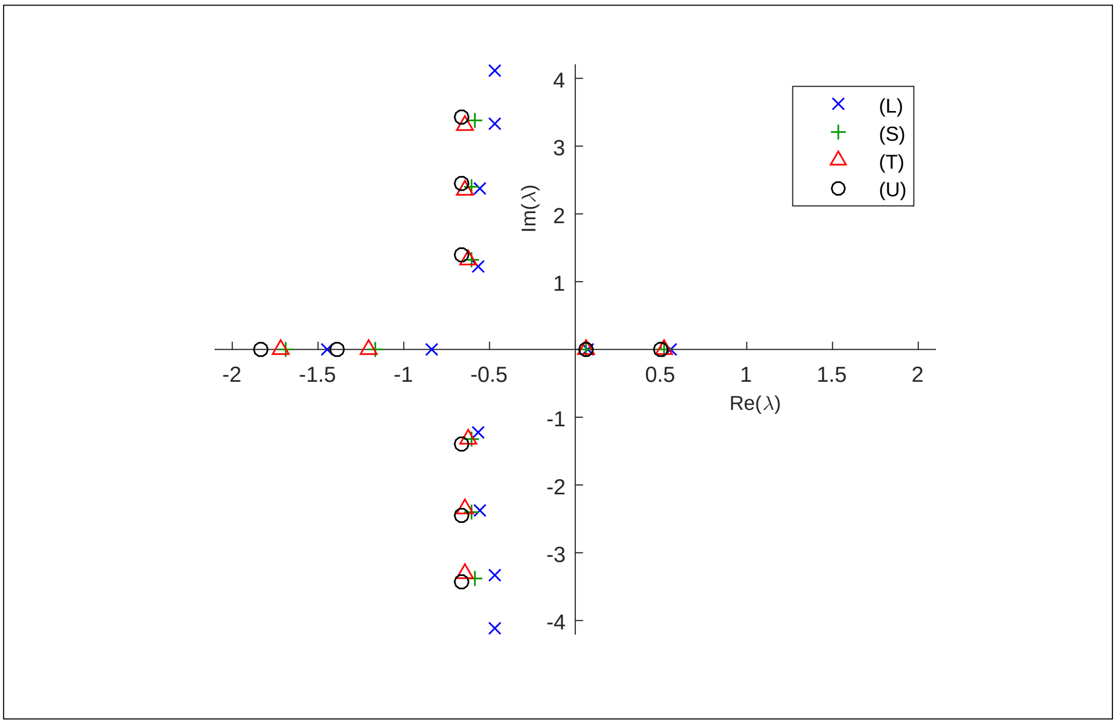

(b) $m = 10$.

Figure 5.2.3: Eigenvalues λ for a rigid annular duct ($s = 0.8$, $M_0 = 0.5$, $\delta = 0.05$,$\eta = 20$) with mean flow profiles: (L) linear boundary layer without slip; (S) linear boundary layer with slip; (T) 1/7th power law boundary layer; (U) uniform flow.

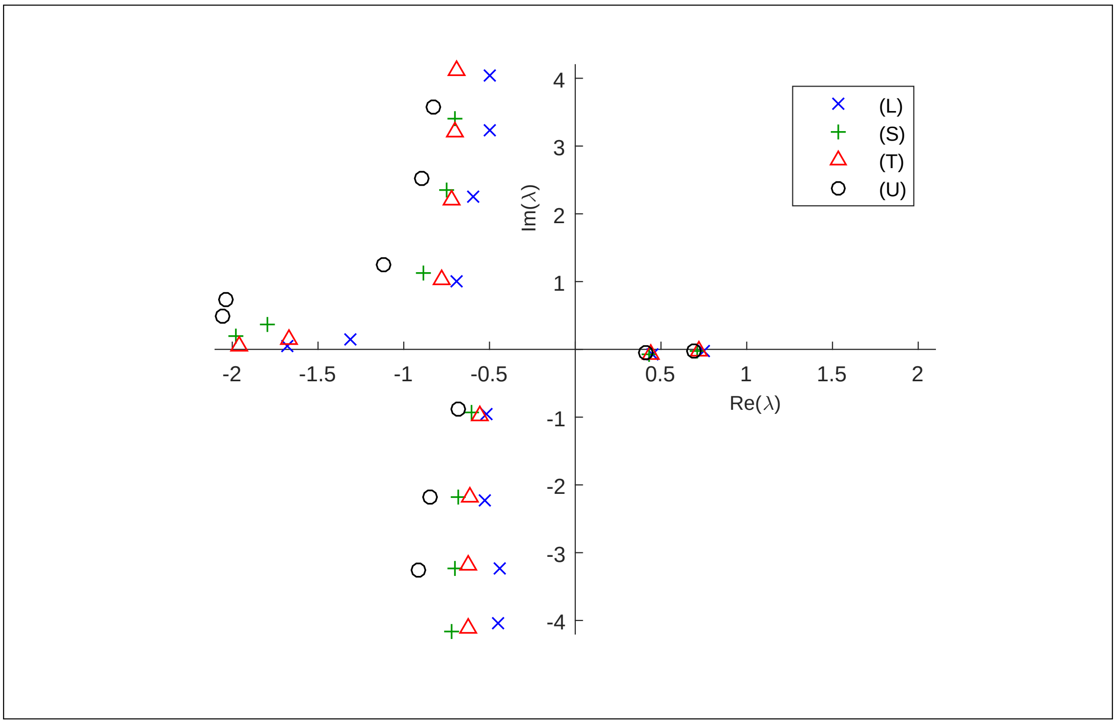

(a)$m = 0$.

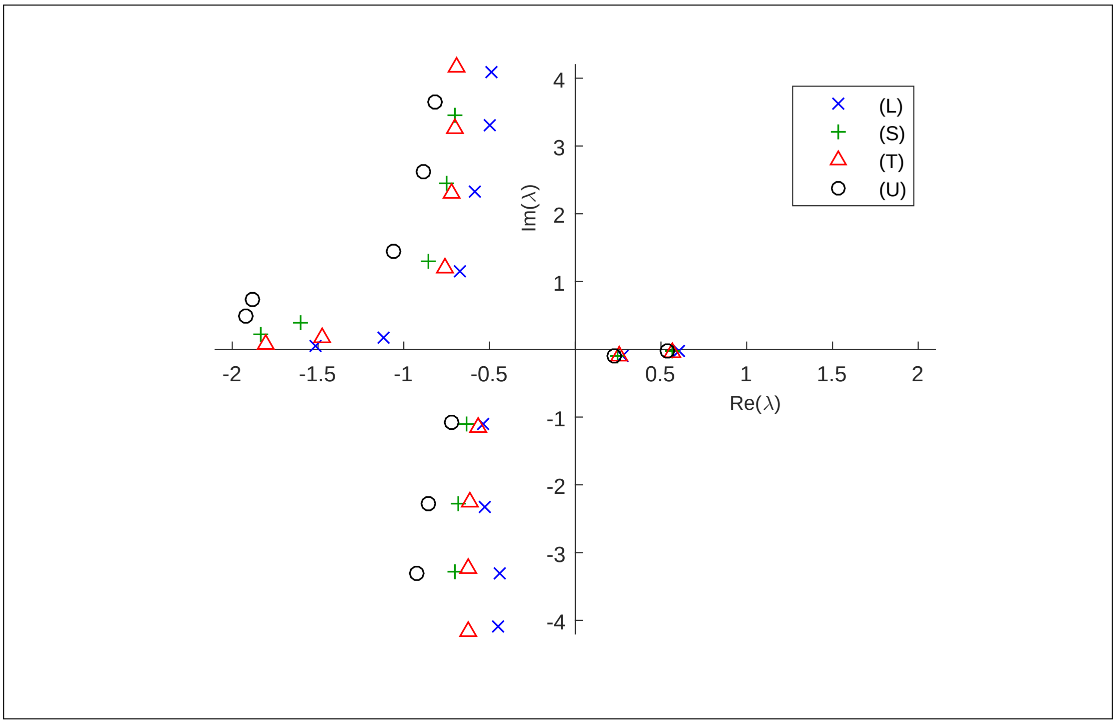

(b) $m = 10$.

Figure 5.2.4: Eigenvalues λ for a lined annular duct ($s = 0.8$, $M_0 = 0.5$, $\delta = 0.05$,$\eta = 20$, $Z = 2 - 3\mathrm{j}$) with mean flow profiles: (L) linear boundary layer without slip; (S) linear boundary layer with slip; (T) 1/7th power law boundary layer; (U) uniform flow.

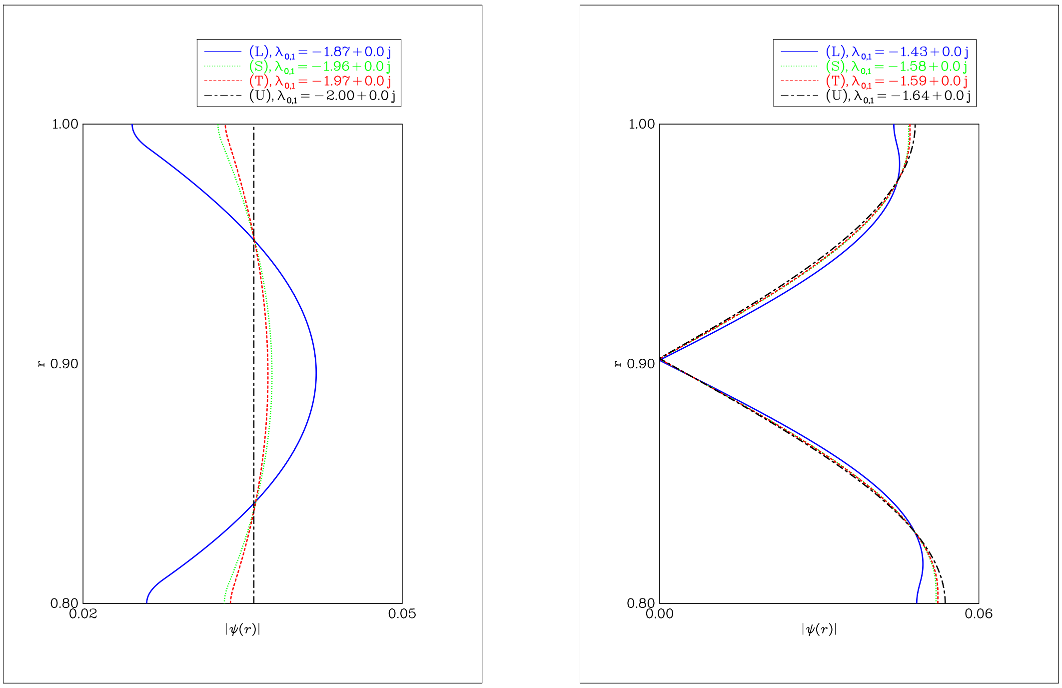

(a) Upstream propagating modes; $n = 1$

(b) Upstream propagating modes; $n = 2$

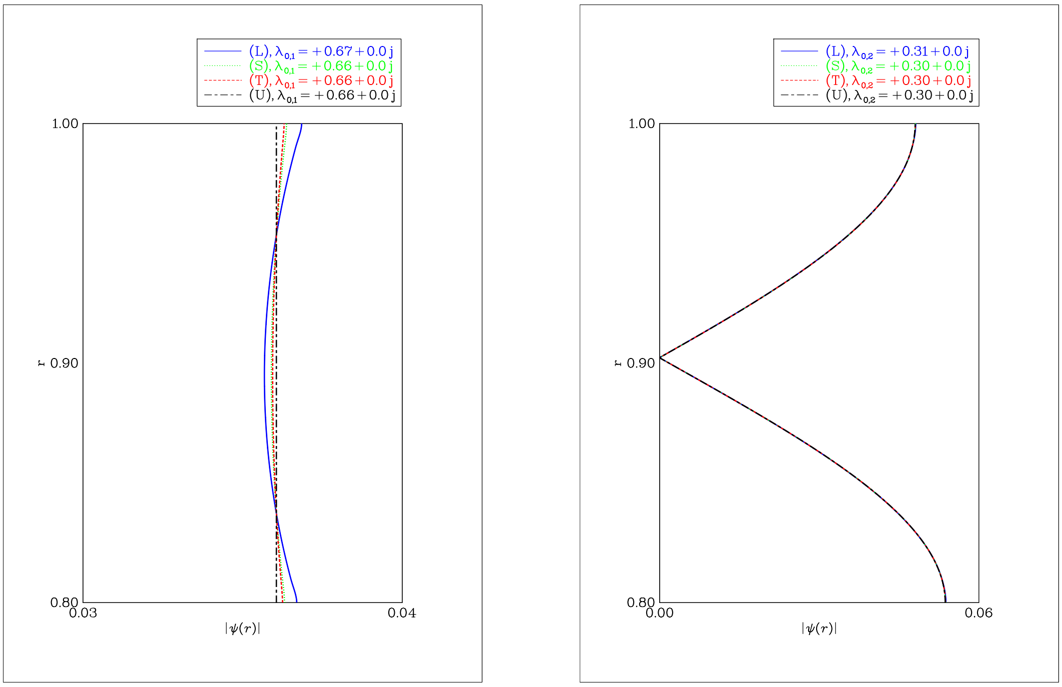

(c) Downstream propagating modes; $n = 1$

(d) Downstream propagating modes; $n = 2$

Figure 5.2.5: Examples of pressure mode shapes $\psi(r)$ for a rigid annular duct ($s = 0.8$, $M_0 = 0.5$, $\delta = 0.01$,$\eta = 20$) for circumferential order $m = 0$. Mode shapes are shown for different flow profiles: (L) linear boundary layer without slip; (S) linear boundary layer with slip; (T) 1/7th power law boundary layer; (U) uniform flow.

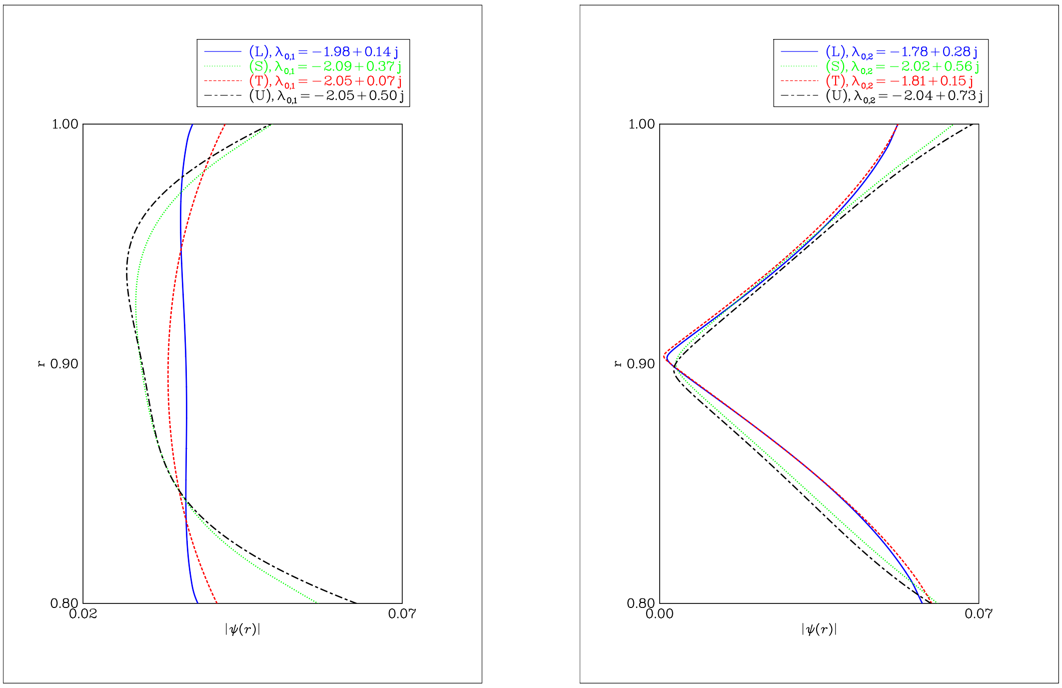

(a) Upstream propagating modes; $n = 1$

(b) Upstream propagating modes; $n = 2$

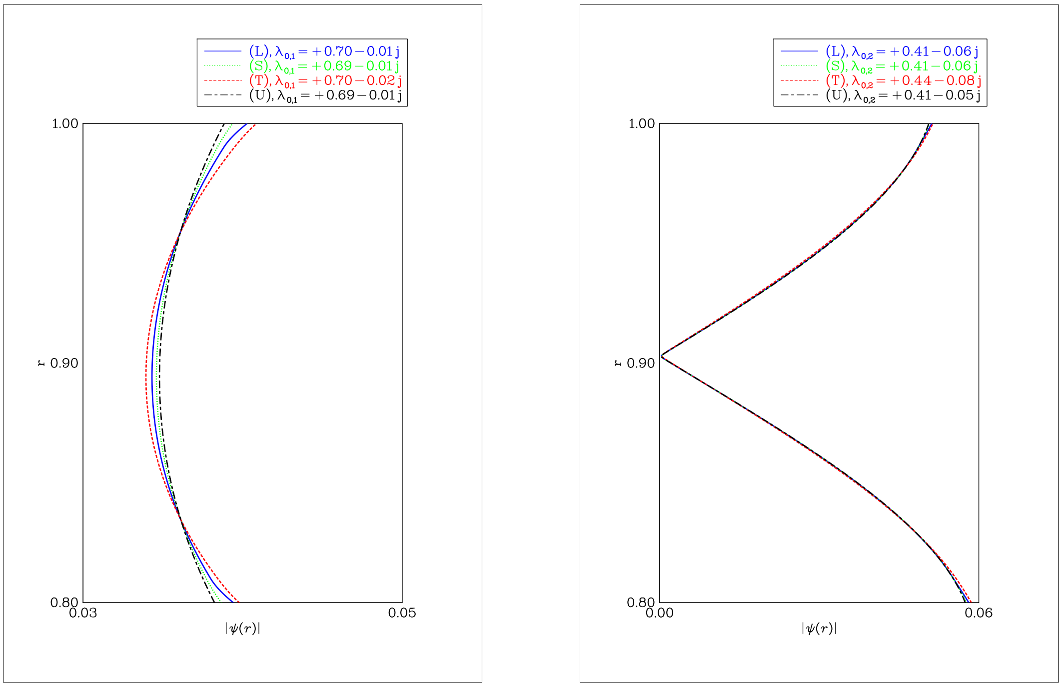

(c) Downstream propagating modes; $n = 1$

(d) Downstream propagating modes; $n = 2$

Figure 5.2.6: Examples of pressure mode shapes $\psi(r)$ for a lined annular duct ($s = 0.8$, $M_0 = 0.5$, $\delta = 0.01$,$\eta = 20$, $Z = 2 - 3\mathrm{j}$) for circumferential order $m = 0$. Mode shapes are shown for different flow profiles: (L) linear boundary layer without slip; (S) linear boundary layer with slip; (T) 1/7th power law boundary layer; (U) uniform flow.

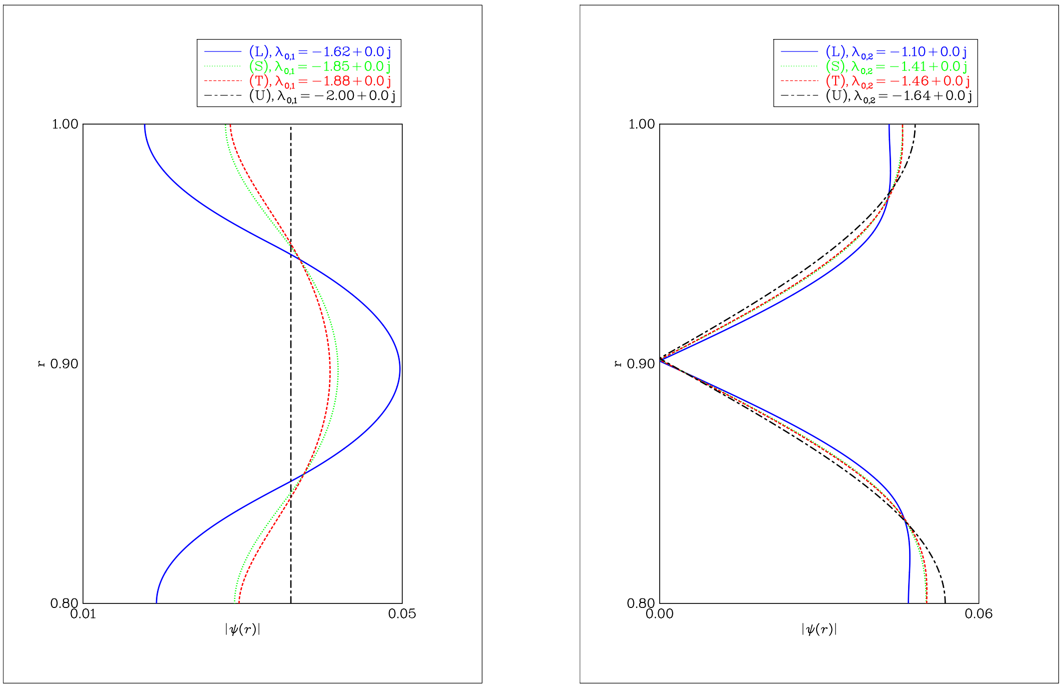

(a) Upstream propagating modes; $n = 1$

(b) Upstream propagating modes; $n = 2$

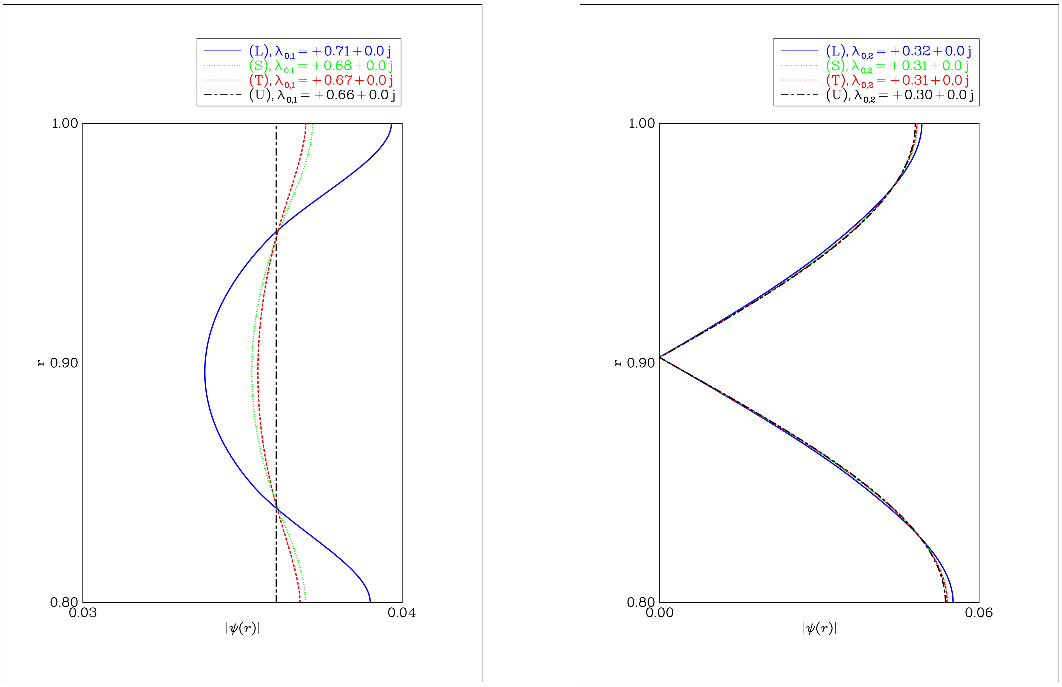

(c) Downstream propagating modes; $n = 1$

(d) Downstream propagating modes; $n = 2$

Figure 5.2.7: Examples of pressure mode shapes $\psi(r)$ for a rigid annular duct ($s = 0.8$, $M_0 = 0.5$, $\delta = 0.05$,$\eta = 20$) for circumferential order $m = 0$. Mode shapes are shown for different flow profiles: (L) linear boundary layer without slip; (S) linear boundary layer with slip; (T) 1/7th power law boundary layer; (U) uniform flow.

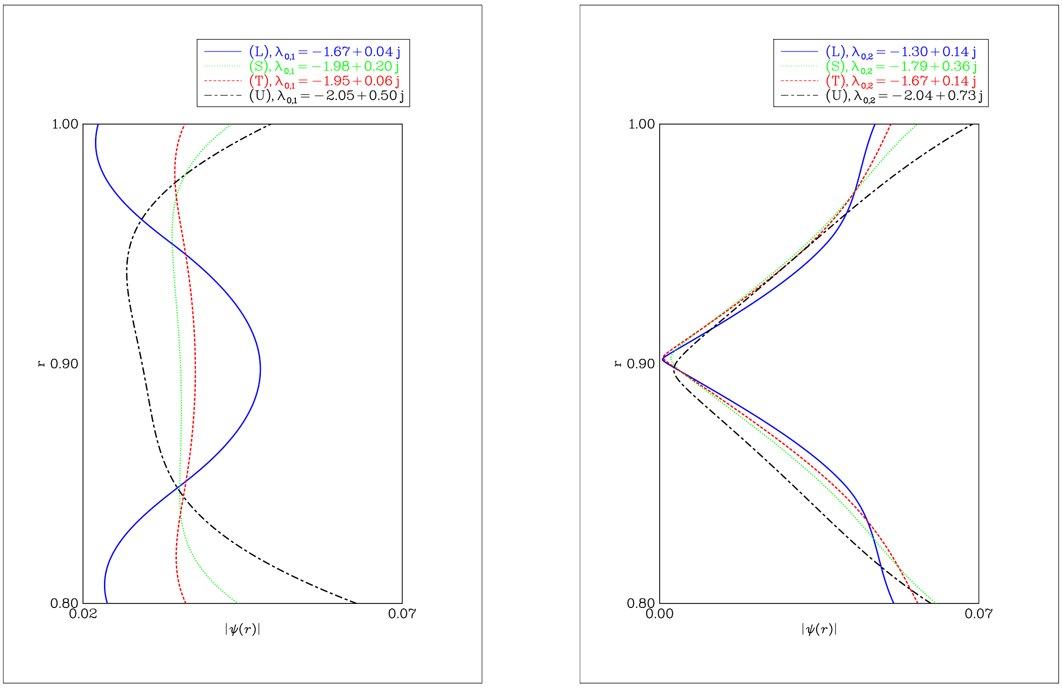

(a) Upstream propagating modes; $n = 1$

(b) Upstream propagating modes; $n = 2$

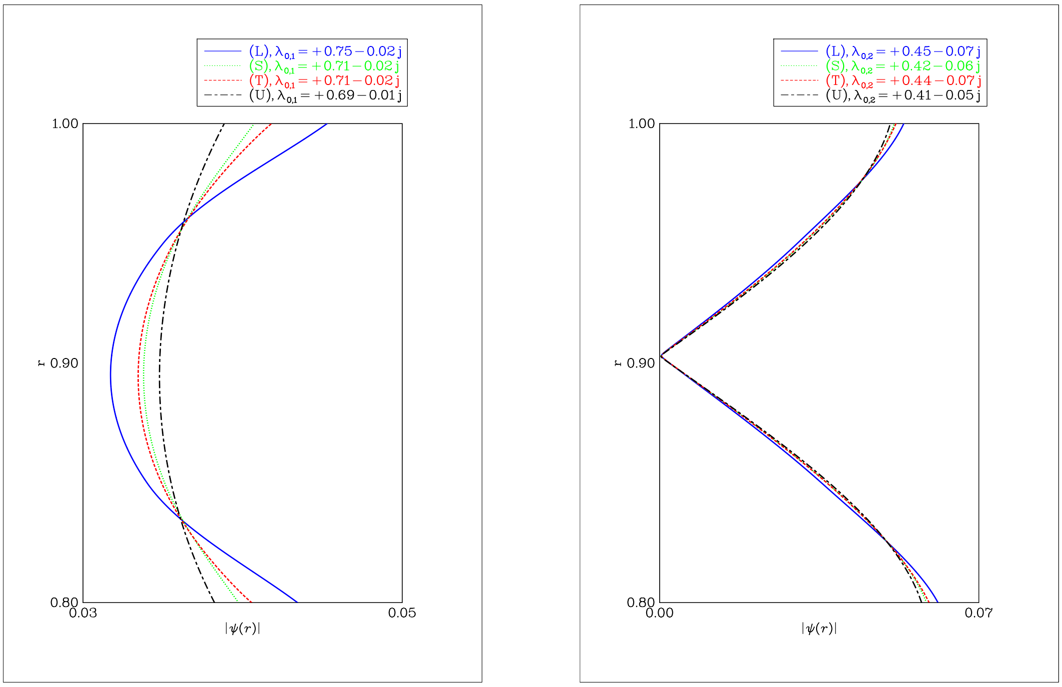

(c) Downstream propagating modes; $n = 1$

(d) Downstream propagating modes; $n = 2$

Figure 5.2.8: Examples of pressure mode shapes $\psi(r)$ for a lined annular duct ($s = 0.8$, $M_0 = 0.5$, $\delta = 0.05$,$\eta = 20$, $Z = 2 - 3\mathrm{j}$) for circumferential order $m = 0$. Mode shapes are shown for different flow profiles: (L) linear boundary layer without slip; (S) linear boundary layer with slip; (T) 1/7th power law boundary layer; (U) uniform flow.

Chapter 6

Practical Application: Effect of Boundary-layer Shielding on High-frequency Sound Transmission

This chapter presents a computation-intensive parametric study that has been carried out using the new proposed finite element implementation described in chapter 3. It is an example of the use of the method in an engineering application to aid the prediction and optimisation of the acoustic impedance of liners used in aero-engine nacelles to mitigate the effects of aircraft engine noise.

As mentioned in chapter 1 on page 1, lining the nacelle with passive acoustic treatments is an effective measure to reduce the emitted noise in the far-field (see recent communications [41],[72]). Ideally, liners must be effective over a wide range of frequencies, reducing both tones and broadband noise at different flow conditions (e.g. at aircraft take-off, climb, cruise, etc.) and satisfy many other requirements and constraints [63]. Liner optimisation is the process of selection of appropriate liner design parameters with respect to requirements and specific noise reduction objectives. Prediction and optimisation of liner performance in fan ducts nowadays relies considerably upon the use of computer simulation of the acoustic field inside the aero-engine ducts for given noise source characteristics [7], and it is concerned with the development of suitable optimization algorithms [8]. In essence, assisting the liner optimisation process is one of the main objectives of the development of models of small-amplitude perturbation propagation in flow ducts.

Historically, early studies focussed on identifying, with respect to a particular duct geometry under consideration, only a small number of least attenuated modes corresponding to a particular frequency (e.g., two modes [116], six modes [65]), and alter the axial attenuation rate of those modes with appropriate choice of the liner's acoustic impedance [116], or trace the change of the axial attenuation rate when varying the frequency[65].

However, the blade passing frequency (BPF) in modern turbofan engines typically corresponds to values of Helmholtz number between 20 and 30. Therefore, the frequency range of interest goes up to values of η of the order of 100, i.e. fourth or fifth harmonic of BPF. At such large Helmholtz number, the number of cut-on modes is of the order of hundreds, so clearly an individual evaluation of the modal attenuation rate for each cut-on mode is not so practical. Moreover, current noise reduction efforts are now increasingly focusing on broadband fan noise, which is commonly modelled by a multi-mode source. Therefore, when dealing with normal mode analysis for modern aircraft engine application, it is necessary to classify hundreds of modes according to their type (acoustic or non-acoustic), direction of propagation (positive or negative travelling waves), and attenuation rate.

Before describing the study in detal, some preliminary background information pertaining to modal sound power transmission in ducts is necessary in order to explain inherent conceptual difficulties in simply adopting a customary transmission loss metric which lead to the introduction of a new cost function.

6.1 Theory of modal sound power transmission in ducts

6.1.1 Case of no mean flow

It is well-known that, for isentropic disturbances in a uniform medium at rest, in a region where acoustic sources are not present, the following law of conservation of acoustic energy holds (cf. [69]),

$$\frac{\partial w}{\partial t} + \nabla \cdot \boldsymbol{j} = 0, \tag{6.1.1}$$

where definitions of energy density [1] associated with an acoustic disturbance,

$$w \triangleq \tfrac{1}{2}\rho_0 \left[\boldsymbol{u}^2 + (\rho_0 c_0)^{-2}\, p^2\right], \tag{6.1.2}$$

and acoustic energy flux density vector

$$\boldsymbol{j} \triangleq p\boldsymbol{u}, \tag{6.1.3}$$

are introduced. The interpretation of equation (6.1.1) is straightforward when integrating over a fixed domain delimited by an oriented surface, S, and applying the divergence theorem,

$$\int_S (\boldsymbol{j} \cdot \boldsymbol{n}_S)\ \mathrm{d}S\ = -\frac{\partial}{\partial t}\int_V w\ \mathrm{d}V \tag{6.1.4}$$

that is, the total net outflow of sound energy per unit time through the surface, S, equals the negative rate of change of the total sound energy within the surface.

Let us introduce the concept of *acoustic intensity* as the time-average acoustic energy flux density vector,

---

[1] Energy per unit volume.

$$\boldsymbol{I} \triangleq \bar{\boldsymbol{j}}, \tag{6.1.5}$$

where the overbar is used to denote a time average operation, and the *time-average power flow across an oriented surface* S with unit normal vector $\boldsymbol{n}_S$ as

$$\overline{W}_S \triangleq \int_S (\boldsymbol{I} \cdot \boldsymbol{n}_S) \ \mathrm{d}S \ , \tag{6.1.6}$$

The following equation holds

$$\nabla \cdot \boldsymbol{I} = 0 \tag{6.1.7}$$

In the study presented here, a semi-infinite duct of uniform cross-section, with a source plane located at the finite end, $z = 0$, is considered. Let us select two cross-sectional oriented surfaces, S_1 and S_2 perpendicular to the duct axial direction, with unit normal vectors pointing in the same direction, and duct wall surface, S_W, between those with unit normal vectors pointing outwards. Based on definition (6.1.6) and property (6.1.7), one then may write

$$\overline{W}_{S_1} - \overline{W}_{S_2} = \overline{W}_{S_W}. \tag{6.1.8}$$

Equation (6.1.8) is perfectly useful to characterize the time average acoustic power absorbed by the duct wall, W_{S_W}. If the left-hand side of the equation is non zero, there is an absorption of energy by the wall.

A convenient metric is the transmission loss, which is typically introduced to quantify the acoustic energy absorbed, and is defined as

$$\triangle\text{SWL} = 10 \ \log_{10}\left(\frac{\overline{W}_{S_1}}{\overline{W}_{S_2}}\right) \ . \tag{6.1.9}$$

In this case, the effect of duct liner design parameters on the overall acoustic energy attenuation can then be determined by comparing time average acoustic powers at two axial locations.

6.1.2 Case of irrotational and homentropic flow

In the case of an irrotational and homentropic[2] flow, a definition of acoustic energy flux density vector, $\boldsymbol{j}$ appears to have gained acceptance, although to some extent arbitrary (cf.[80]). Written in non-dimensional form

$$\boldsymbol{j} = p\boldsymbol{u} + \frac{1}{\rho_0 c_0^2}\boldsymbol{M}p^2 + \rho_\infty\left(\boldsymbol{M}\cdot\boldsymbol{u}\right)\boldsymbol{u} + \frac{1}{c_0^2}\boldsymbol{M}\left(\boldsymbol{M}\cdot\boldsymbol{u}\right)p \tag{6.1.10}$$

The expression was originally introduced by Cantrell & Hart [26]. It has been adopted, among others, by Morfey [80] and Joseph et al. [61].

In the case of a duct with uniform mean flow velocity in the z direction, assuming a monochromatic acoustic field varying in time with frequency ω , the time average acoustic power flow across a cross-sectional surface, S, perpendicular to the duct axial direction is given by

$$\overline{W}_S = \int_S I_z\, dS = \tfrac{1}{2}\int_S \left[\left(1+M^2\right)\mathrm{Re}\left(\hat{p}\hat{u}_z^*\right) + M\left(|\hat{p}|^2 + |\hat{u}_z|^2\right)\right]\, dS \tag{6.1.11}$$

where I_z denotes the axial component of the acoustic intensity, the asterisk denotes the complex conjugate, $\hat{p}$ and $\hat{u}_z$ are the complex pressure amplitude and the axial component of the complex particle velocity, respectively, defined as:

$$p\left(\boldsymbol{x},t\right) \triangleq \mathrm{Re}\left(\hat{p}\left(\boldsymbol{x}\right)\, e^{\mathrm{j}\,\omega\, t}\right), \tag{6.1.12}$$

$$u_z\left(\boldsymbol{x},t\right) \triangleq \mathrm{Re}\left(\hat{u}_z\left(\boldsymbol{x}\right)\, e^{\mathrm{j}\,\omega\, t}\right). \tag{6.1.13}$$

---

[2] Isentropic flow with uniform entropy

.Note that the identities

$$\begin{aligned}\overline{p^2} &= \tfrac{1}{2}|\hat{p}|^2,\\ \overline{u_z^2} &= \tfrac{1}{2}|\hat{u}_z|^2,\\ \overline{pu_z} &= \tfrac{1}{2}\mathrm{Re}\left(\hat{p}\hat{u}_z^*\right),\end{aligned}$$

have been used here.

Since a semi-infinite duct is considered here (that is, no end-termination wave reflections), we consider waves traveling in one direction only. The complex acoustic pressure field, $\hat{p}\,(r,\,\theta,\,z)$, subject to the convected wave equation can be decomposed in terms of travelling modes

$$\hat{p}^+\,(r,\,\theta,\,z) = \sum_{m=-\infty}^{\infty}\sum_{n=1}^{\infty} p_{mn}^+(r,\,\theta,\,z), \quad \text{or} \quad \hat{p}^-\,(r,\,\theta,\,z) = \sum_{m=-\infty}^{\infty}\sum_{n=1}^{\infty} p_{mn}^-(r,\,\theta,\,z). \tag{6.1.14}$$

where $(r,\,\theta,\,z)$ are the non-dimensional radial, azimuthal and axial coordinates, respectively; m and n are the azimuthal and radial orders, respectively, and

$$p_{mn}^{\pm}(r,\,\theta,\,z) = A_{mn}^{\pm}\psi_{mn}^{\pm}(r)\,e^{-\mathrm{j}\,(m\,\theta\pm\lambda_{mn}^{\pm}k\,z)}, \tag{6.1.15}$$

are the positive and negative propagating waves. $\psi_{mn}^{\pm}$ are the transverse (radial) mode shapes, the parameters $\lambda_{mn}^{\pm}$ are the axial wave numbers normalized by the free field wavenumber, k, $A_n^{\pm}$ are the modal amplitudes, which are determined, for example, by the mechanism of noise generation involved at plane $z = 0$.

In a similar way, the axial component of the complex acoustic particle velocity field, $\hat{u}_z\,(r,\,\theta,\,z)$ can be decomposed in term of modes

$$\hat{u}_z^+\,(r,\,\theta,\,z) = \sum_{m=-\infty}^{\infty}\sum_{n=1}^{\infty} u_{z,mn}^+(r,\,\theta,\,z), \quad \text{or} \quad \hat{u}_z^-\,(r,\,\theta,\,z) = \sum_{m=-\infty}^{\infty}\sum_{n=1}^{\infty} u_{z,mn}^-(r,\,\theta,\,z). \tag{6.1.16}$$

Substituting equations (6.1.15) in the linearized Euler momentum balance equation give

$$u_{z,mn}^{\pm} = \gamma_{mn}^{\pm}\,p_{mn}^{\pm}, \tag{6.1.17}$$

where

$$\gamma_{mn}^{\pm} \triangleq \frac{\lambda_{mn}^{\pm}}{1 - M\lambda_{mn}^{\pm}}. \tag{6.1.18}$$

Let us consider modes traveling, say, in the positive z-direction. Only cut-on modes transport energy; let us assume that $N_{(m)}^+$ is the number of cut-on modes for azimuthal order, m.

Substituting equations (6.1.15) and (6.1.17) into (6.1.11), the time average acoustic power, $\overline{W_S^+}$ corresponding to modes travelling in the positive direction would contain $\sum_{m=-\infty}^{\infty}\left(N_{(m)}^+\right)^2$ separate terms, of which $\sum_{m=-\infty}^{\infty} N_{(m)}^+\left[N_{(m)}^+ - 1\right]$ are cross terms. In the case of acoustic hard walls, the mode shape functions are orthogonal and the expression of the time average acoustic power across a cross-sectional surface, S, given in equation (6.1.11) reduce to

$$\overline{W_S^+} = \sum_{m=-\infty}^{\infty}\sum_{n=1}^{N_{(m)}^+} W_{mn}^+ \tag{6.1.19}$$

where the modal elements of the time average acoustic power

$$W_{mn}^+(z = z_S) = \chi_{mn}^+\int_S |p_{mn}(r,\,\theta,\,z_S)|^2\,dS = \chi_{mn}^+|A_{mn}^+|^2 e^{2\,\mathrm{Im}\left(\lambda_{mn}^+\right)k\,z_S} \tag{6.1.20}$$

are found by integrating $I_{z,mn}$ over the cross section of the duct, and

$$\chi^+_{mn} \triangleq \frac{S}{2}\left[\left(1+M^2\right)\mathrm{Re}\left(\gamma^+_{mn}\right) + M\left(1+|\gamma^+_{mn}|^2\right)\right], \tag{6.1.21}$$

It is assumed here that the orthogonal mode shape functions are normalized so that

$$\frac{1}{S}\int_S \psi_{mn}(r)\, e^{\jmath m\theta}\psi^*_{m'n'}(r)\, e^{-\jmath m'\theta}\,\mathrm{d}\theta\; r\;\mathrm{d}r \;= \delta_{mm'}\delta_{nn'}. \tag{6.1.22}$$

where δ_{ij} is the Kronecker delta.

The transmission loss calculated between two cross-sectional surfaces, S_1 and S_2, perpendicular to the axial direction, at a distance L apart is then

$$\triangle\mathrm{SWL} = 10\;\log\left(\frac{\bar{W}_{S_1}}{\bar{W}_{S_2}}\right) = 10\;\log\left(\frac{\sum_{m=-\infty}^{\infty}\sum_{n=1}^{N^+_{(m)}}\chi^+_{mn}|A^+_{mn}|^2}{\sum_{m=-\infty}^{\infty}\sum_{n=1}^{N^+_{(m)}}\chi^+_{mn}|A^+_{mn}|^2 e^{2\,\mathrm{Im}\left(\lambda^+_{mn}\right)\,k\,L}}\right) \tag{6.1.23}$$

In aero-engine liner design studies, the source is typically assumed exciting all possible in-duct modes with equal energy across a discrete set of frequencies, that is,

$$|A^+_{mn}|^2 = c \tag{6.1.24}$$

where c is a constant.

In the case of acoustic soft walls, modes are not orthogonal and the expression of the time average acoustic power, $\overline{W}^+_S$, cannot be simplified as in equation (6.1.19). The $\sum_{m=-\infty}^{\infty} N^+_{(m)}\left[N^+_{(m)}-1\right]$ cross-terms are now present and may be of significant magnitude. A possible approach to calculation is that adopted by Law [70], which consists of splitting the energy contribution equally between the two ± modes that form a cross-term.

6.1.3 Case of an arbitrary mean flow

In the case of rotational mean flows (such as the shear flow) and non-isentropic flows, there is no expression for a conserved acoustic intensity. Therefore, it is not possible to evaluate the overall acoustic energy attenuation through a practical calculation of transmission loss such as equation (6.1.23).

As mentioned in chapter 1, the fundamental difficulty arises from the fact that the mean flow is subject to coupled entropy, vorticity and acoustic perturbations and, in this case, definitions of acoustic energy density and flux carried by disturbances are problematic.

Several energy conservation laws for wave propagation in a moving medium have been proposed by Morfey [80] Möhring [76] Myers [86] [87]. They all propose a generalized form of the conservation law given in equation (6.1.1). For example, Morfey [80] found an identity by separating out the irrotational part of the perturbed flow.

The derivation by Myers [86, 87] of a general equation governing the transport of energy associated with disturbances seems to be most widely accepted. Myers' basic idea was to derive a 'disturbance' energy relation directly from the total fluid energy conservation law (cf. [69]). By purely algebraic manipulation of equations, he obtained an exact energy corollary

$$\frac{\partial w_{\text{exact}}}{\partial t} + \nabla \cdot \boldsymbol{j}_{\text{exact}} = -\mathcal{D}_{\text{exact}}, \tag{6.1.25}$$

where terms w_{exact} and $\boldsymbol{j}_{\text{exact}}$ were identified as energy density and flux, respectively, carried by any disturbance, and dissipation term, $\mathcal{D}_{\text{exact}}$, included all terms excluded from w_{exact} and $\boldsymbol{j}_{\text{exact}}$. No linearization was assumed up to this point, hence the name 'exact'. Note that in the case of irrotational and homentropic flow, $\mathcal{D}_{\text{exact}} = 0$ and equation (6.1.10) is retrieved.

Then, each fluid quantity was expanded to second order (quadratic) approximation[3] in

---

[3] Acoustic energy density in the case of a stagnant medium (equation (6.1.2)) is quadratic to leading order in disturbance quantities.

the perturbed quantities and energy density, flux and dissipation carried by the unsteady disturbances were obtained. The main finding was that the expressions for the 'perturbation' energy density and flux are second order expressions depending only on first order quantities.

Atassi [10] made use of Myers' disturbance energy relation in the particular case of an annular duct with homentropic swirling mean flow and highlighted that "the disturbance field interacts with the mean flow and mean flow gradients to transfer energy between the mean flow and the propagating disturbances".

6.2 Study 3: Investigation of liner acoustic performance at high-frequency in flow ducts

Solutions (eigenmodes) of the eigenvalue problem for the Pridmore-Brown equation have been determined. Among them, only 'predominantly' acoustic cut-on modes have been identified and selected in accordance to the criterion described in chapter 3. Their modal weight (that is, their relative importance) has been determined according to considerations of modal energy coupling between the sound generation and propagation processes at an ideal cross-sectional plane of the duct, as it will be explained below.

In the present study, a fully developed flow in a semi-infinite cylindrical duct is considered (that is, no reflection of sound waves at the duct's end-termination). Flow is assumed to comprise a uniform core flow and a thin boundary layer at lined duct walls. A quarter-sine mean-velocity profile is used to model the boundary layer as, for example, in reference [35].

The acoustically soft-wall condition considered in the study is assumed to be characterised by a locally-reacting acoustic impedance as defined in equation (5.0.2). The values $R_{\text{FS}} = 2$, $\tilde{m}/\rho_0 = 2.5\text{cm}$ and $\hat{a} = 1\text{m}$ have been chosen as typical values from aeronautical applications (see comments at the end of section 1, chapter 5 on page 95).

Table 6.2.1 shows the values of the dimensionless specific acoustic impedance, Z, corresponding to values of dimensionless frequency, η, and dimensionless cell depth of air cavities, d, selected for the parametric study.

	$d = 0.0127$	$d = 0.0254$	$d = 0.0508$
$\eta = 20$	2-3.35j	2-1.3j	2-0.12j
$\eta = 50$	2-0.107j	2+0.94j	2+2.71j
$\eta = 100$	2+2.19j	2+3.96j	2+2.89j

Table 6.2.1: Values of the dimensionless specific acoustic impedance, Z, corresponding to values of dimensionless frequency, η, and dimensionless cell depth of air cavities, d, selected for the parametric study.

To overcome the inability to determine a suitable theoretical expression for the acoustic intensity in a duct in the presence of a sheared mean flow and, consequently, evaluate the transmission loss as a measure of the overall acoustic energy absorbed, a new definition of cost function has been introduced to provide guidance for optimizing the performance of acoustic liners. It is based on the variation in sound pressure level at two arbitrary stations at the duct walls. The change in the sound pressure level is given by

$$\triangle\text{SPL} = 10\ \log_{10}\left(\frac{|\hat{p}^{+}\left(z=0\right)|^{2}}{|\hat{p}^{+}\left(z=L\right)|^{2}}\right)\ , \tag{6.2.1}$$

and similarly,

$$\triangle\text{SPL} = 10\ \log_{10}\left(\frac{|\hat{p}^{-}\left(z=0\right)|^{2}}{|\hat{p}^{-}\left(z=-L\right)|^{2}}\right)\ . \tag{6.2.2}$$

With respect to how to allocate appropriate modal amplitudes, the assumption that has been made here is that, , for each azimuthal order, the sums of the squared pressures at the duct wall of each cut-on mode contribute approximately equally. This is justified following a recent experimental finding by Achunche [1], who studied the modal power distribution required to accurately model fan broadband noise. That is

$$\sum_{n=1}^{N^{+}_{(m=-M)}} |p^{\pm}_{(-M,\,n)}|^2 = \sum_{n=1}^{N^{+}_{(m=0)}} |p^{\pm}_{(0,\,n)}|^2 = \sum_{n=1}^{N^{+}_{(m=M)}} |p^{\pm}_{(M,\,n)}|^2 = c \qquad (6.2.3)$$

where c is a constant.

This assumption enables the cost function given in equation (6.2.1) to be calculated:

$$\begin{aligned} |\hat{p}^{+}\,(z=0)|^2 = \; & \sum_{n=1}^{N^{+}_{(m=-M)}} |p^{+}_{(-M,\,n)}|^2 + \ldots\ldots\ldots \\ & + \sum_{n=1}^{N^{+}_{(m=0)}} |p^{+}_{(0,\,n)}|^2 + \ldots\ldots\ldots \\ & + \sum_{n=1}^{N^{+}_{(m=M)}} |p^{+}_{(M,\,n)}|^2 = (2\,M+1)\,c \end{aligned}$$

$$\begin{aligned} |\hat{p}^{+}\,(z=L)|^2 = \; & \frac{c}{N^{+}_{(m=-M)}} \sum_{n=1}^{N^{+}_{(m=-M)}} e^{2\,\mathrm{Im}\left(\lambda^{+}_{(-M,\,n)}\right)\,k\,L} + \ldots\ldots\ldots \\ & + \frac{c}{N^{+}_{(m=0)}} \sum_{n=1}^{N^{+}_{(m=0)}} e^{2\,\mathrm{Im}\left(\lambda^{+}_{(0,\,n)}\right)\,k\,L} + \ldots\ldots\ldots \\ & + \frac{c}{N^{+}_{(m=M)}} \sum_{n=1}^{N^{+}_{(m=M)}} e^{2\,\mathrm{Im}\left(\lambda^{+}_{(M,\,n)}\right)\,k\,L} \end{aligned}$$

Similarly,

$$\begin{aligned} |\hat{p}^{-}\,(z=0)|^2 = \; & \sum_{n=1}^{N^{-}_{(m=-M)}} |p^{-}_{(-M,\,n)}|^2 + \ldots\ldots\ldots \\ & + \sum_{n=1}^{N^{-}_{(m=0)}} |p^{-}_{(0,\,n)}|^2 + \ldots\ldots\ldots \end{aligned}$$

$$+ \sum_{n=1}^{N^{-}_{(m=M)}} |p^{-}_{(M,\,n)}|^2 = (2\,M+1)\,const\,,$$

and

$$|\hat{p}^{-}\,(z=-L)|^2 = \frac{c}{N^{-}_{(m=-M)}} \sum_{n=1}^{N^{-}_{(m=-M)}} e^{-2\,\mathrm{Im}\left(\lambda^{-}_{(-M,\,n)}\right)\,k\,L} + \ldots\ldots\ldots$$
$$+ \frac{c}{N^{-}_{(m=0)}} \sum_{n=1}^{N^{-}_{(m=0)}} e^{-2\,\mathrm{Im}\left(\lambda^{-}_{(0,\,n)}\right)\,k\,L} + \ldots\ldots\ldots$$
$$+ \frac{c}{N^{-}_{(m=M)}} \sum_{n=1}^{N^{-}_{(m=M)}} e^{-2\,\mathrm{Im}\left(\lambda^{-}_{(M,\,n)}\right)\,k\,L}\,.$$

In the parametric study, five control factors were selected. These factors and their levels are listed in table 6.2.2.

	Levels
Wave propagation direction	downstream (positive), upstream (negative)
Boundary layer thickness, δ (in units of duct radius $\tilde{a}$)	$0^{*)}$ to 0.1 in equally spaced steps of 0.005
Distance between two axial points, L (in units of $\tilde{a}$)	0.5, 1, 2
Cell depth of air cavities, d (in units of duct radius $\tilde{a}$)	0.0127, 0.0254, 0.0508
Helmholtz number, η	20, 50. 100

*) Boundary layer thickness value equal to 0 corresponds to the case of uniform mean flow.

Table 6.2.2: Control factors and their level.

Figures 6.2.1 to 6.2.9 show variation of the performance metric (cost function) defined in equation (6.2.1) for downstream (positive) and upstream (negative) wave propagation direction against a set of boundary layer thickness values in the range between 0.5% and 10% of the duct radius. Boundary layer thickness value equal to 0 corresponds to the case of uniform mean flow.

Results are in agreement with the expected general effect of a shear layer on sound transmission. Sound propagating in the direction of flow (positive modes) is more refracted towards the wall, resulting in a larger acoustic pressure level difference, ΔSPL, between two axial stations compared to a smaller acoustic pressure level difference when the sound is propagating opposite to the flow (negative modes), because in this case more of the sound is refracted away from the wall.

The exception is for the case of Helmholtz number $\eta = 20$, liner configurations corresponding to nondimensional cell parameter $d = 0.0127$ and $d = 0.0254$, dimensionless boundary layer thickness within the range of $\delta = 0.005$ to $\delta = 0.05$ (figures 6.2.1 on the next page and 6.2.2 on page 130).

What is interesting from the results of this study is its quantitative aspect. In the case of sound propagating in the direction of flow, the sound level attenuation does not change significantly as the boundary layer thickens (around one decibel or less), and it is nearly the same for all the three frequencies and the three different liner configurations considered.

On the contrary, in the case of sound propagating opposite to the flow, there is a substantial decrease in the attenuation as the boundary layer thickens, which it is more significant at moderately large Helmholtz number (η = 20) than at very high Helmholtz number (η = 100).

It also has to be noted that, at moderately large Helmholtz number, attenuation decreases as the boundary layer increases in thickness at an approximately comparable rate over the entire range considered ($\delta = 0.005$ to $\delta = 0.1$). On the contrary, at very high Helmholtz number, changes in the attenuation mainly take place within the range of $\delta = 0.005$ to $\delta = 0.03$.

6.3 Summary of parametric study

The aim of the study presented here was to provide an example of how to carry out a performance analysis of acoustic liners by using the finite element code developed in this work. A multi-mode analysis coupled with a cost function calculation based on

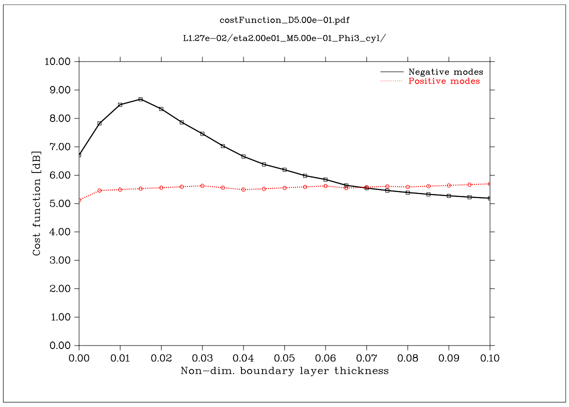

(a) $L = \frac{1}{2}$

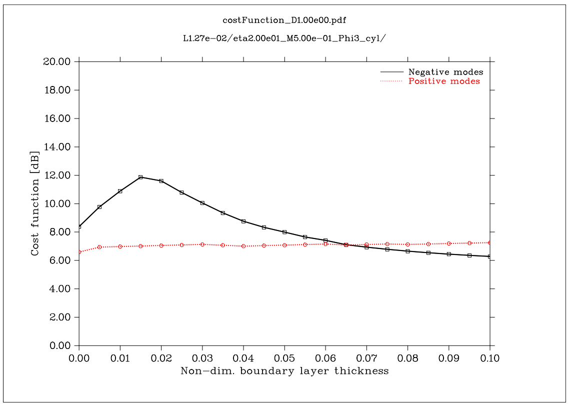

(b) $L = 1$

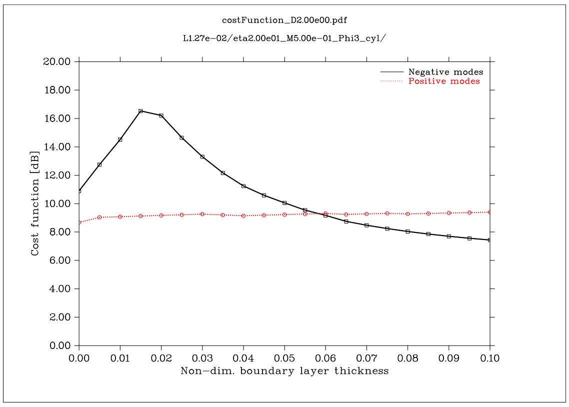

(c) $L = 2$

Figure 6.2.1: ΔSPL between axial points separated by a distance L plotted against boundary-layer thickness, δ (all dimensionless quantities). Liner depth $d = 0.0127$, Helmholtz number $\eta = 20$.

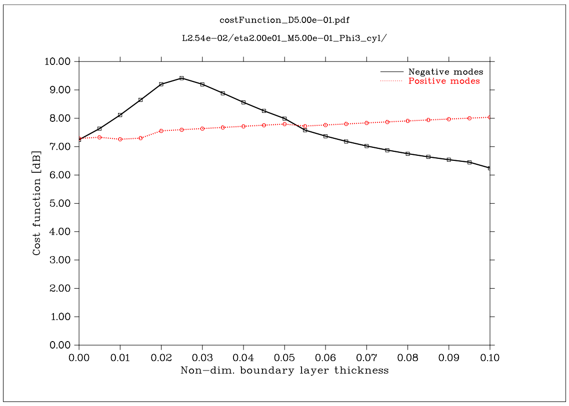

(a) $L = \frac{1}{2}$

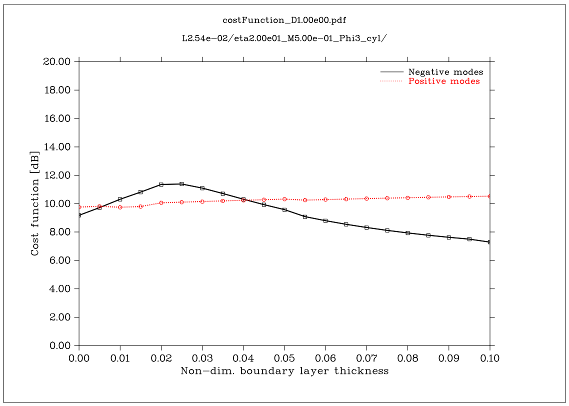

(b) $L = 1$

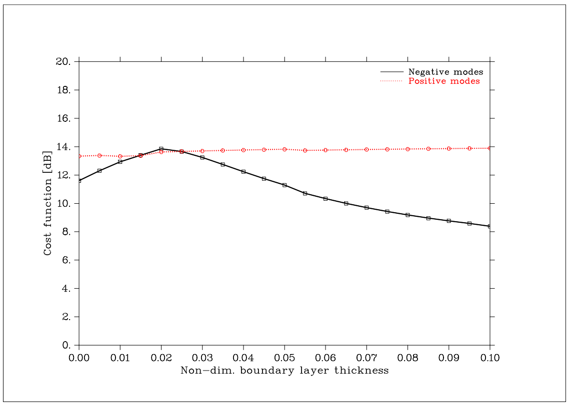

(c) $L = 2$

Figure 6.2.2: ΔSPL between axial points separated by a distance L plotted against boundary-layer thickness, δ (all dimensionless quantities). $d = 0.0254$, $\eta = 20$.

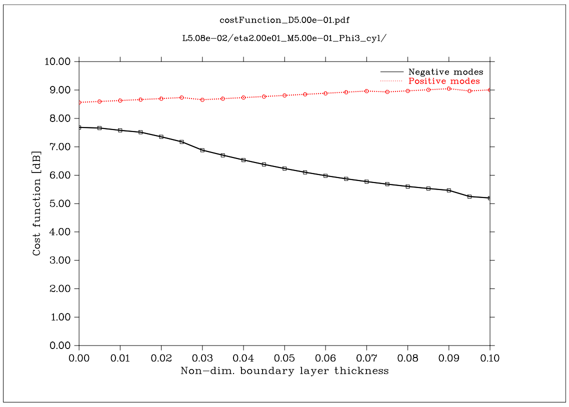

a) $L = \frac{1}{2}$

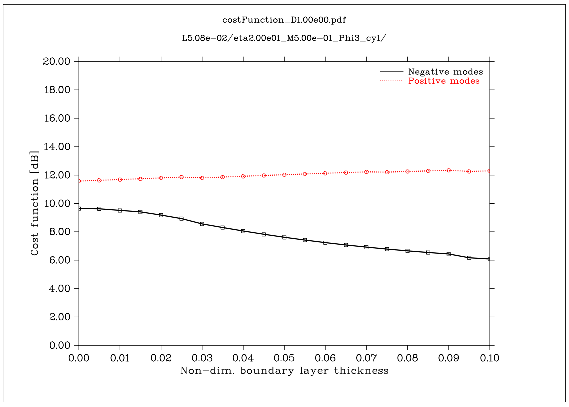

(b) $L = 1$

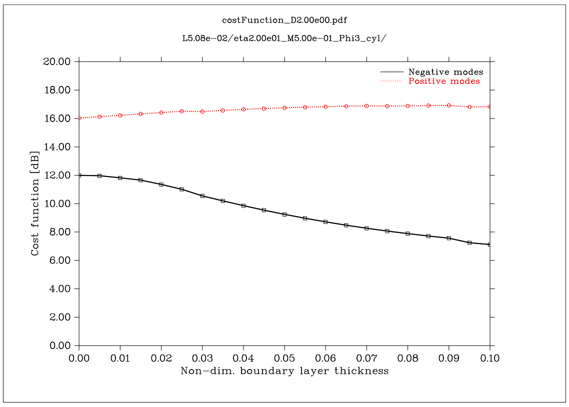

(c) $L = 2$

Figure 6.2.3: ΔSPL between axial points separated by a distance L plotted against boundary-layer thickness, δ (all dimensionless quantities). $d = 0.0254$, $\eta = 20$.

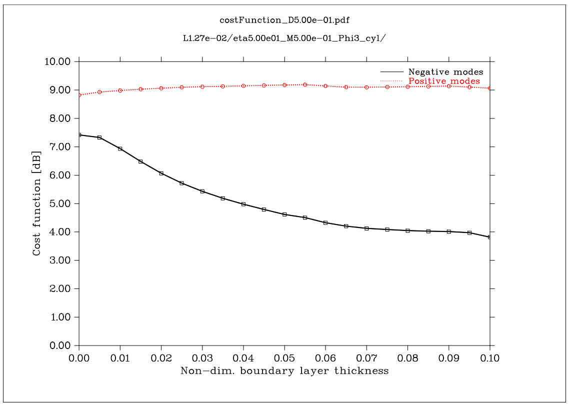

(a) $L = \frac{1}{2}$

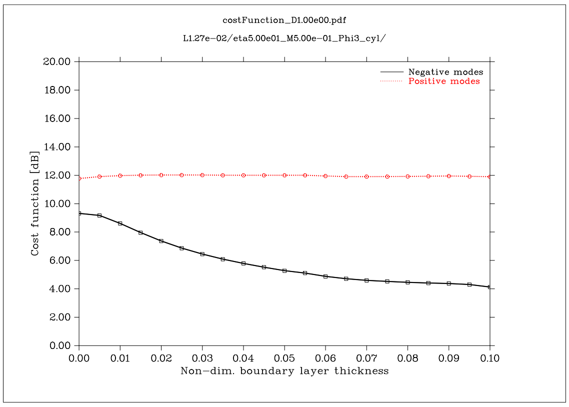

(b) $L = 1$

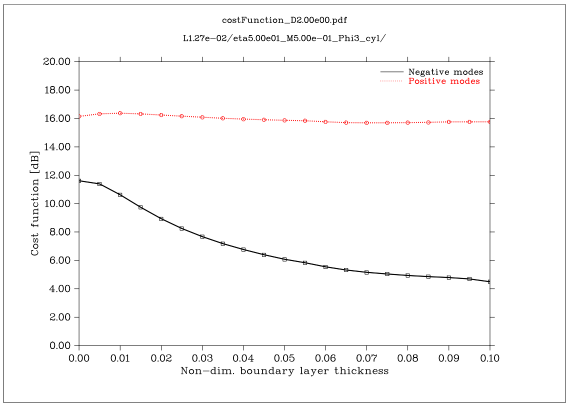

(c) $L = 2$

Figure 6.2.4: ΔSPL between axial points separated by a distance L plotted against boundary-layer thickness, δ (all dimensionless quantities). $d = 0.0127$, $\eta = 50$.

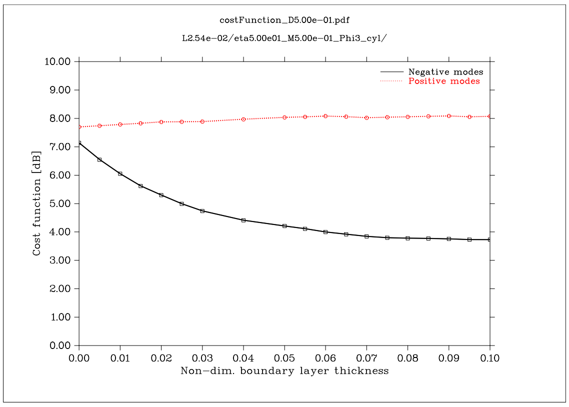

(a) $L = \frac{1}{2}$

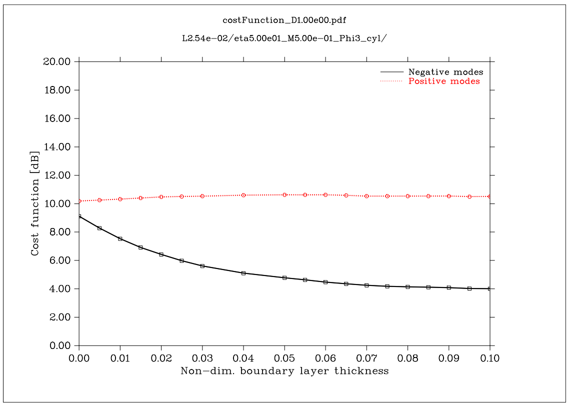

(b) $L = 1$

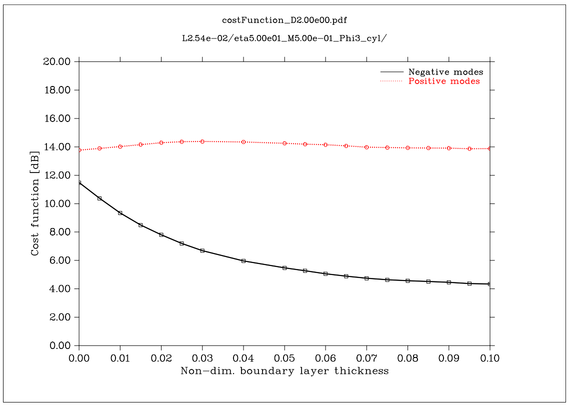

(c) $L = 2$

Figure 6.2.5: ΔSPL between axial points separated by a distance L plotted against boundary-layer thickness, δ (all dimensionless quantities). $d = 0.0254$, $\eta = 50$.

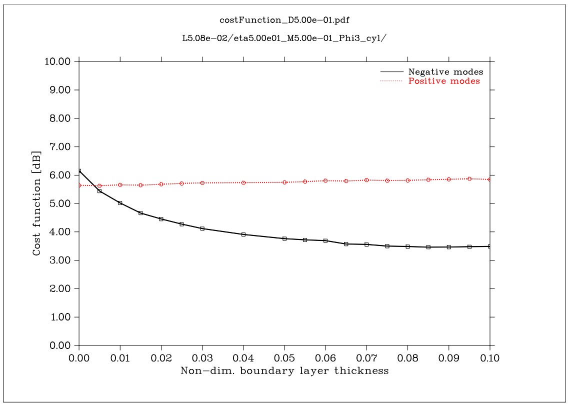

(a) $L = \frac{1}{2}$

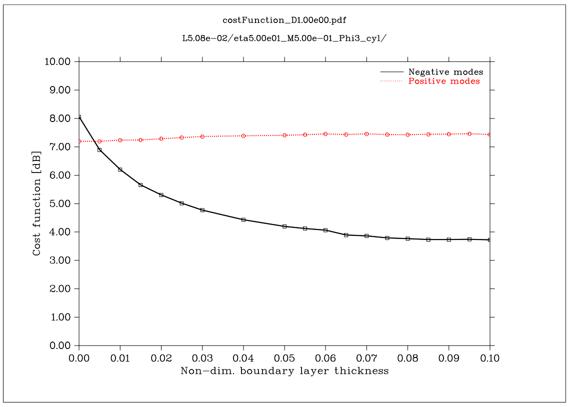

(b) $L = 1$

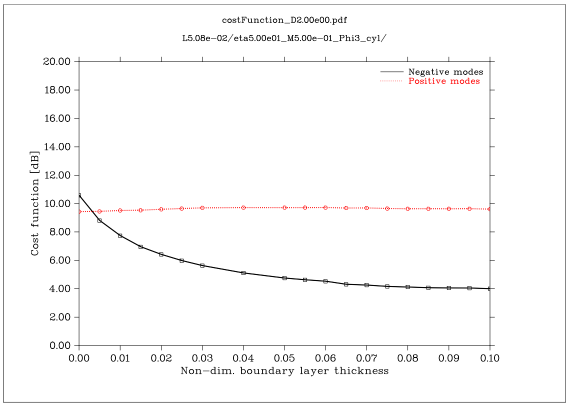

(c) $L = 2$

Figure 6.2.6: ΔSPL between axial points separated by a distance L plotted against boundary-layer thickness, δ (all dimensionless quantities). $d = 0.0254$, $\eta = 50$.

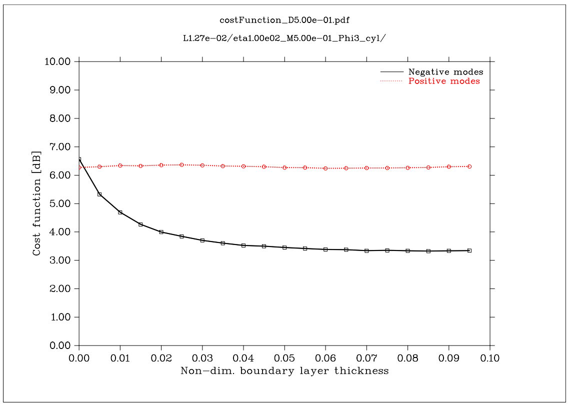

(a) $L = \frac{1}{2}$

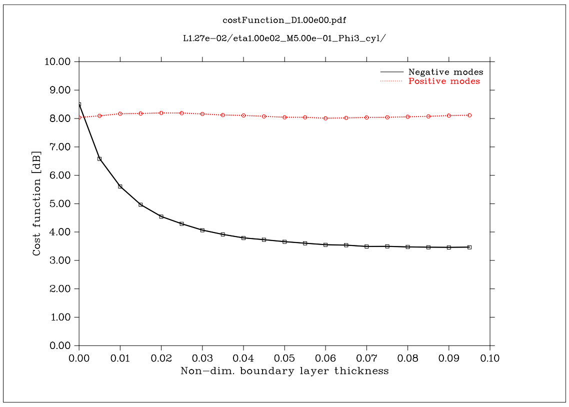

(b) $L = 1$

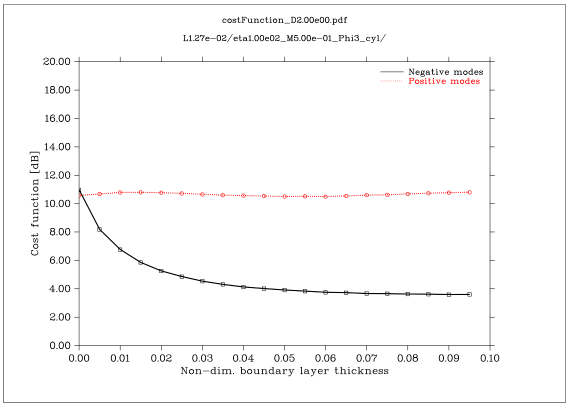

(c) $L = 2$

Figure 6.2.7: ΔSPL between axial points separated by a distance L plotted against boundary-layer thickness, δ (all dimensionless quantities). $d = 0.0127$, $\eta = 100$.

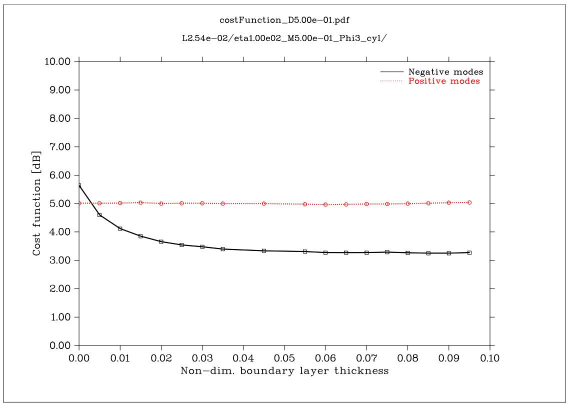

(a) $L = \frac{1}{2}$

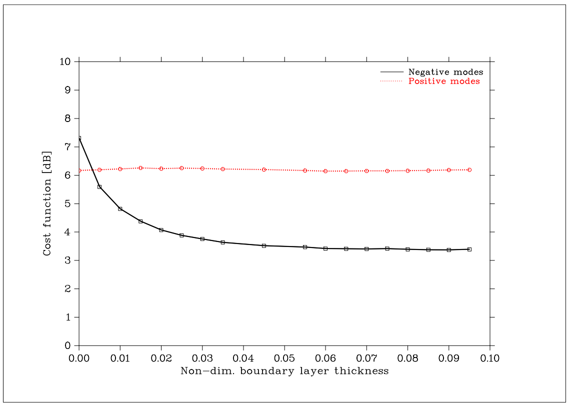

(b) $L = 1$

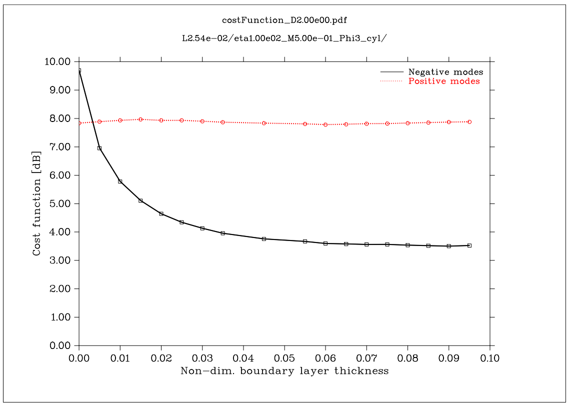

(c) $L = 2$

Figure 6.2.8: ΔSPL between axial points separated by a distance L plotted against boundary-layer thickness, δ (all dimensionless quantities). $d = 0.0254$, $\eta = 100$.

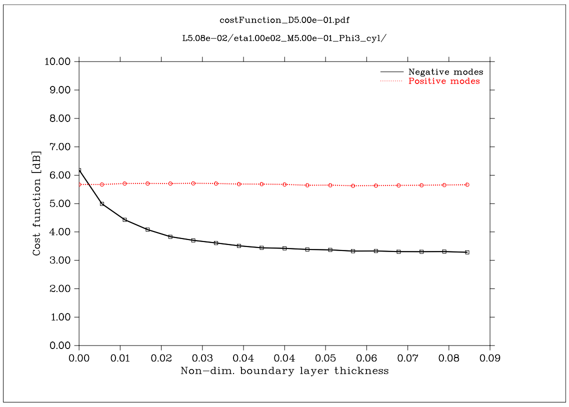

(a) $L = \frac{1}{2}$

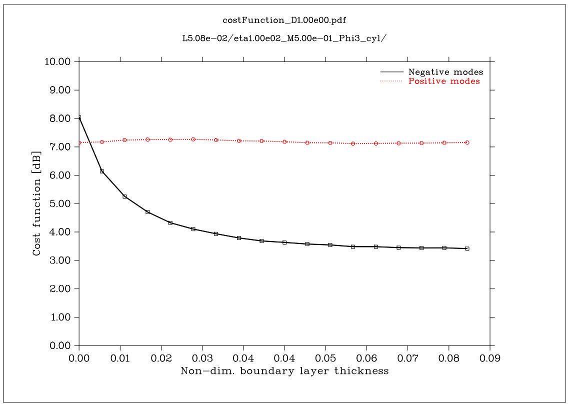

(b) $L = 1$

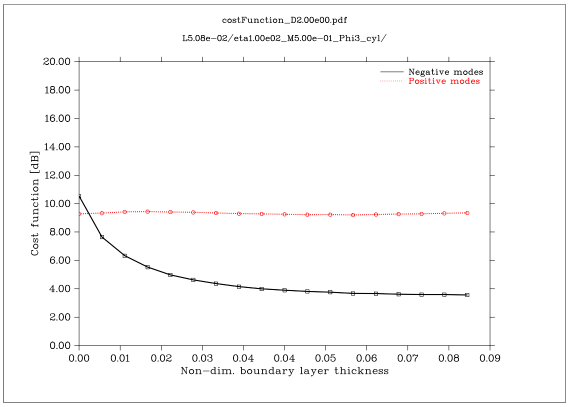

(c) $L = 2$

Figure 6.2.9: ΔSPL between axial points separated by a distance L plotted against boundary-layer thickness, δ (all dimensionless quantities). $d = 0.0254$, $\eta = 100$.

sound pressure level difference at two arbitrary stations at the duct walls provides a simple quantifiable measure of the effect of the boundary-layer thickness on the liner attenuation. A parametric study was conducted at moderately large Helmholtz number (η = 20 and η = 50), and at very high Helmholtz number (η = 100), for a set of liners of different cell depth value, on varying boundary-layer thickness of the sheared mean flow.

It has to be highlighted that, although typically frequencies up to the 5th harmonic of the blade passing frequency are of interest to optimise the acoustic treatment in aero-engine ducts (which correspond to Helmholtz number in excess of 100), to the author's knowledge, there exist no studies in the literature similar to the one presented here, probably because of the difficulty to calculate, at a reasonable computational cost, the large number of modes that are 'cut-on' at high frequencies (in the order of hundreds for η = 100).

In this work, the duct and mean flow have been assumed axisymmetric, and therefore a one-dimensional FEM formulation was possible, which substantially decreases the computational time. This study has then provided a quantifiable measure of the performance of three different liner configurations (based on a simple acoustic impedance model given by (5.0.2)). The main result is that, at very high frequencies (η = 100), for the specific liner configurations considered, the sound pressure level difference, ΔSPL, is significantly affected by the presence of the boundary layer only when the sound is propagating opposite to the flow. Moreover, at the same frequency range and the upstream propagation case, the rate of change of ΔSPL, as a function of the boundary layer thickness, is significant only in a small interval of values (approx. $\delta = 0.005$ and $\delta = 0.03$).

To the author's knowledge, this result is new. Although important assumptions have been made (equal energy for modes of the same azimuthal order), the result is believed to be of interest and relevance to the aerospace sector, specifically associated with the design of aero-engine acoustic linings. Predictions which do not take into account the region of thin sheared mean flow may significantly over-predict the liner attenuation at high frequencies.

Chapter 7

Summary and Concluding Remarks

The aim of the work was to develop fast and efficient analytical and numerical methods, that could be used with (a) high-frequency sound (corresponding to Helmholtz number up to 100), (b) sheared mean flow, (c) acoustically lined ducts, to calculate the transmission of sound in lined flow ducts [http://gtr.rcuk.ac.uk/projects?ref=EP/E065775/1]. The basis for all the work was the Pridmore-Brown equation (modal equation for parallel shear flows) [104][81].

Emphasis on high-frequency sound was motivated by the fact that, in modern high bypass ratio engine design, it has become imperative to carry out high-frequency analysis in order to include several harmonics of the fan's blade passing frequency.

Interest in combining the effect of the acoustic impedance of the lining, and the sheared mean flow,on pressure perturbations in ducts, was motivated by the need to improve the accuracy of current models based on uniform flow and the widely-applied Ingard–Myers boundary condition, in order to foster the optimisation of the design of aero-engine acoustic linings.

The focus was on the efficient implementation of methods that could calculate, with accuracy and at modest computational cost, the large number of modes that are 'cut-on' at high frequencies for use in an engineering context.

To achieve this, the geometry of real inlet and bypass ducts has been simplified. Ducts have been modelled as infinitely long with axisymmetric (circular or annular) cross-section uniform in the axial direction. Wall acoustic linings have been assumed locally reacting and characterized by an impedance independent of axial and azimuthal coordinates. Mean flow has been assumed homentropic and axisymmetric, but not radially uniform. For this axisymmetric geometry, solutions for the pressure perturbation field have been sought by separation of variables, which have yielded an immediate reduction in the dimension of the problem.

Although the focus has been on providing examples where the mean flow, frequency and liner acoustic impedance have been chosen to be representative of a turbofan aircraft engine application, the methods and their associated considerations presented in this work are of general theoretical nature in the field of small-amplitude unsteady fluid motion in ducts, relevant to a number of engineering applications.

7.1 Summary of achievements

The aim of the work has been achieved by the development of two different methods: the finite element method (presented in chapter 3) and the method of approximate equivalent boundary condition (presented in chapter 4).

Since the advent of scientific computation in the early 1970s, the finite element method has been regarded as a flexible and reliable technique to solve mathematical problems. Since then, there appears to have been, within the aeroacoustics community, a progressive interest in applying the technique to solve computational-intensive problems in two or three dimensions with boundary conditions of complex realistic geometries (see, for example, reference [7]) rather than exploiting its computational efficiency and accuracy to solve simpler problems. In this work, the approach was the latter: the finite element method was adopted as a tool capable to provide solutions faster, more efficiently and more accurately than using more traditional numerical schemes, such as the Runge-Kutta method [3] [23].

Surprisingly, to the best of the author's knowledge, no previous publications provide a comprehensive finite element formulation of the one-dimensional Pridmore–Brown equation for the particular case of axisymmetric geometry. Therefore, the obvious first challenge was to obtain a correct formulation within the framework of the finite element mathematical theory [21][54][64]. Chapter 3 provides a comprehensive formulation, useful to be directly translated into computer code. Appendix B offers practical details of the construction of the code.

As a novel contribution, it has been shown that the variational formulation of the one-dimensional Pridmore–Brown problem (equation 3.2.22a) can be obtained either starting from its corresponding strong form (equation 3.2.19) or starting from the variational formulation of the two-dimensional Pridmore–Brown problem (equation 3.2.5) by introducing test and trial functions $\psi(r)e^{-\mathrm{j}m\theta}$ and $v(r)e^{-\mathrm{j}m\theta}$ (equations (3.2.23a) and (3.2.23b), respectively). In order to obtain the latter, complex-valued linear functional and sesquilinear form were introduced to deal with complex functions. An additional contribution was the calculation of the analytical expressions of the mass and stiffness matrix elements, which are reported in Appendix A.

The implementation of the method into a C++ computer program enabled the rapid computation of a large number of modes at very high frequencies (Helmholtz number of the order of 100) at a modest computational cost, even on a standard personal computer. Due to the low CPU time, the code may well be used for optimization of liner properties.

The computer code has been extensively tested and verified by comparison of the eigenmodes with exact analytic solutions in the case of uniform flow, and other solutions reported previously in the case of a boundary layer flow. Convergence of the solutions has been verified. To the best of the author's knowledge, it is the first time that a complete mathematical formulation and code implementation description of the Galerkin's finite element method to solve the Pridmore-Brown problem in axisymmetric ducts has been given.

A significant advantage of the finite element implemenation is its ability to use a finer grid in the vicinity of the duct walls in the regions of strong mean velocity gradients, and a coarser grid in the core flow region, which translates into a lower number of degrees of freedom for an equivalent accuracy, thus a remarkable efficiency of the method, or very accurate solutions inside the boundary layer.

A number of post-processing routines have been developed which classify the modes according to their type (acoustic or non-acoustic), direction of propagation (positive or negative travelling waves), and attenuation rate. This post-processing enables the least attenuated modes to be identified, which are the most significant modes to be targeted for noise control measures.

The second method developed in this work derives asymptotic expansions of the modal solutions in the boundary layer in the limit of vanishing thickness, and uses these to define an ‘equivalent’ boundary condition for the uniform core flow. The problem can then be solved analytically for the uniform flow.

Although most of the mathematical development is similar to that by Eversman & Beckemeyer [39], a certain degree of manipulation was necessary in order to conform to the particular length scaling for dimensionless lengths used throughout this work. This approach potentially offers a very efficient calculation method, as it simply evaluates analytical expressions, although numerical methods are still necessary to solve a trascendental equation. A contribution to new knowledge here is the extension of the method to the case of mean flow with slip at the wall.

A number of numerical examples of the use of the finite element method with parameters representative of an aeronautical application have been provided in three different studies.

In the first study the influence of a relatively thin boundary layer thickness (corresponding to dimensionless boundary layer thickness, δ =0.03) on the mode attenuation (modal structure, in general) for a relatively high frequency (corresponding to Helmoltz numberη =30) has been investigated, thus filling a gap in the literature with respect to this type of investigation with respect to high frequencies. Numerical results have confirmed that, for the particular case considered, only significant effects are observed for upstream propagating modes.

In the second study the dependency of attenuation rate of upstream-propagating modes on the boundary-layer thickness and shape factor only of a boundary layer of an arbitrary mean velocity profile has been investigated. In contrast with general observations by Nayfeh et al. [90], the study has demonstrated that, at high frequencies, in the case of lined duct, approximating a 1/7th power law-without-slip boundary-layer profile with a linear-with-slip profile having matching thickness and shape factor produce dissimilar upstream-propagating modes.

In the third study an example of how to carry out a performance analysis of acoustic liners by using the finite element code developed in this work has been demonstrated.An investigation of the effect of boundary-layer shielding on sound transmission at high frequencies (Helmholtz number up to the order of 100) has been carried out. A new cost function has been defined to provide a quantifiable measure of an acoustic liner's performance for a multi-mode noise source.The main result is that, at very high frequencies (η = 100), for the specific liner configurations considered, the sound pressure level difference, ΔSPL, is affected by the presence of the boundary layer significantly only when the sound is propagating opposite to the flow. Moreover, at the same frequency regime and upstream propagation case, the rate of change of ΔSPL, as a function of the boundary layer thickness, is significant only in a small interval of very thin thickness values. This is a new result which it is believed will be of interest to the aero-engine acoustic liner industry.

7.2 Final considerations

Considering a duct carrying sheared mean flow introduces a new level of complexity to the analysis of the propagation of unsteady pressure modes when compared to the case of uniform flow. Three considerations are worth highlighting here, which outline possible areas of future work.

1. Critical layers arise in shear flows as a mathematical singularity. When solving numerically the Pridmore–Brown equation using the finite element solver, calculations have revealed the existence of a conspicuous set of eigenvalues clustered about the value 1/M. Those modes have been classified as predominantly convected with the mean flow, and they have been filtered out from calculations of acoustic attenuation assuming their contribution to be insignificant. It is however recognised that a better understanding of their mathematical properties is desirable, in particular, how they are represented in a finite element scheme.

2. The concept that, for any arbitrary thin boundary layers with similar shape factor, 'cut-on' modes may have comparable axial decay rates, has not been fully explored. It is author's opinion that, in order to provide stronger evidence to prove or disprove the idea, an extensive parametric study, conducted in a systematic way and possibly with the support of a design of experiments (DoE) methodology, is necessary.

3. There is no expression for a conserved acoustic intensity. Therefore, the transmission loss which, in the case of uniform homentropic flows, can directly quantify the overall acoustic energy absorbed by the liner, cannot be evaluated. A new single-parameter descriptor (cost function) has been defined to evaluate the in-duct sound attenuation. How effectively it can be used in a practical design optimisation procedure for acoustic linings has to be explored.

Appendix A

Exact Integration of The Mass and Stiffness Matrices

Case of linear basis functions

$$\begin{aligned}
M_{11}^{(e)} &= \frac{1}{12}\left(-3x_i^2 + 2x_i x_j + x_j^2\right) \\
M_{12}^{(e)} = M_{21}^{(e)} &= \frac{1}{12}\left(-x_i^2 + x_j^2\right) \\
M_{22}^{(e)} &= \frac{1}{12}\left(-x_i^2 - 2x_i x_j + 3x_j^2\right)
\end{aligned}$$

$$\begin{aligned}
K_{11}^{(e)} &= \frac{-(x_i - x_j)\left(x_i + m^2 x_i + x_j - 3m^2 x_j\right) + 2m^2 x_j^2 \mathrm{Log}\left[\frac{x_j}{x_i}\right]}{2(x_i - x_j)^2} \\
K_{12}^{(e)} = K_{21}^{(e)} &= -\frac{\left(-1 + m^2\right)\left(x_i^2 - x_j^2\right) + 2m^2 x_i x_j \mathrm{Log}\left[\frac{x_j}{x_i}\right]}{2(x_i - x_j)^2} \\
K_{22}^{(e)} &= \frac{(x_i - x_j)\left(\left(-1 + 3m^2\right) x_i - \left(1 + m^2\right) x_j\right) + 2m^2 x_i^2 \mathrm{Log}\left[\frac{x_j}{x_i}\right]}{2(x_i - x_j)^2}
\end{aligned}$$

Case of quadratic basis functions

$$M_{11}^{(e)} = \frac{1}{60}\left(-7x_i^2 + 6x_i x_j + x_j^2\right)$$

$$
\begin{aligned}
M_{12}^{(e)} = M_{21}^{(e)} &= \frac{1}{15} x_i(-x_i + x_j) \\
M_{22}^{(e)} &= -\frac{4}{15}\left(x_i^2 - x_j^2\right) \\
M_{23}^{(e)} = M_{32}^{(e)} &= \frac{1}{15} x_j(-x_i + x_j) \\
M_{33}^{(e)} &= \frac{1}{60}\left(-x_i^2 - 6x_i x_j + 7x_j^2\right)
\end{aligned}
$$

$$
\begin{aligned}
K_{11}^{(e)} &= \frac{1}{6}\left(\frac{11x_i}{-x_i + x_j} + \frac{3x_j}{-x_i + x_j} - \right. \\
&\quad \left. - \frac{m^2\left(x_i^4 - 6x_i^3 x_j - 10x_i x_j^3 + 15x_j^4 - 6x_j^2(x_i + x_j)^2 \mathrm{Log}\left[\frac{x_j}{x_i}\right]\right)}{(x_i - x_j)^4}\right) \\
K_{12}^{(e)} = K_{21}^{(e)} &= \frac{2}{3(x_i - x_j)^4}\left((x_i - x_j)\left(8x_i^3 + \left(-14 + m^2\right) x_i^2 x_j + \right.\right. \\
&\quad \left. + 2\left(2 + 5m^2\right) x_i x_j^2 + \left(2 + m^2\right) x_j^3\right) + \\
&\quad \left. + 6m^2 x_i x_j^2 (x_i + x_j) \mathrm{Log}\left[\frac{x_j}{x_i}\right]\right) \\
K_{22}^{(e)} &= \frac{4}{3}\left(\frac{12x_i}{-x_i + x_j} + \frac{4x_j}{-x_i + x_j} - \right. \\
&\quad \left. - \frac{m^2\left(x_i^4 - 8x_i^3 x_j + 8x_i x_j^3 - x_j^4 - 12x_i^2 x_j^2 \mathrm{Log}\left[\frac{x_j}{x_i}\right]\right)}{(x_i - x_j)^4}\right) \\
K_{23}^{(e)} = K_{32}^{(e)} &= \frac{4x_j}{3x_i - 3x_j} - \\
&\quad - \frac{2m^2 x_i\left((x_i - x_j)\left(x_i^2 + 10x_i x_j + x_j^2\right) + 6x_i x_j (x_i + x_j) \mathrm{Log}\left[\frac{x_j}{x_i}\right]\right)}{3(x_i - x_j)^4} \\
K_{33}^{(e)} &= \frac{1}{6}\left(\frac{3x_i}{-x_i + x_j} + \frac{11x_j}{-x_i + x_j} + \right. \\
&\quad \left. + \frac{m^2\left(15x_i^4 - 10x_i^3 x_j - 6x_i x_j^3 + x_j^4 + 6x_i^2(x_i + x_j)^2 \mathrm{Log}\left[\frac{x_j}{x_i}\right]\right)}{(x_i - x_j)^4}\right)
\end{aligned}
$$

Appendix B

FEM Code Implementation

This section is devoted to describe the specific practical details of the construction of the code which implements the method. In the following we will refer to such implementation with the acronym AMADO (Acoustic Mode Analysis in Ducts with flOw).

This section is organized as follows. Section B.1 presents a state of the art of finite element programming, in order to give insight on best practices in program design to ensure a robust, reliable and calculation-efficient solution as well as save development time. Section B.2 first introduces the overall initial requirements for the implementation explaining the reasoning behind them. Then, it presents a sneak overview of the general organization of the software highlighting the rationale for certain design choices. It demonstrates how the object-oriented approach yields advantages over procedural (e.g. FORTRAN) programming methods and discusses the adoption of a number of design patterns. Finally, it highlights key elements in the design of the classes (the building blocks of object oriented programming), and it provides comments on selected parts of the code (code extracts).

B.1 State of the art of finite element programming

The FEM has traditionally been programmed in procedural programming languages such as FORTRAN, and some early textbooks on the FEM provide examples of computer implementation written in this language. Since the introduction of the object-oriented paradigm in the early 1990s, which since then became all pervasive in computing, a number of articles on applying this programming style to the FEM have been published. Some of the first papers on the subject are by Dubois-Pelerin et al. [32] and Mackie [73]. Both papers contain thorough discussions on how the finite element programming could benefit from this new programming style.

The main benefits that are highlighted in the first paper can be summarized as follows. First, implementing algebraic entities (such as a vector and a matrix) and fundamental entities of the FEM (such as a node and an element) as new types (objects) is a natural extension of mathematical thinking, which leads to self-descriptive software. Then, the fact that objects can encapsulate their associated data and manage their own state and actions encourages to apply a distributed (decentralized) control programming style, which improves the overall code mainteinability. Finally, the high degree of coding modularity which can be reached offers the possibility of testing parts of the code independently.

The second paper stresses that the finite element method is by its very nature a modular numerical tool and demonstrates how the richer data structures of the object-oriented programming enables a high degree of modularity. Moreover, it explains how features such as inheritance and virtual methods allow software to be substantially altered without major changes to the existing code.

Since then, a number of papers have been published dealing with the issue of how to design classes in order to ensure maximum flexibility and software reuse. For example, in related papers by Mackie [74, 75] a proposal of design of the basic objects of the finite element method like the element and the node are meticulously described. In a paper by Dubois-Pelerin & Pegon [31] two classes of objects, namely problem and domain, which encapsulate the relevant procedures of FEM are proposed to set up an adequate data organization in order to overcome the complexity which arise when programming the FEM.

B.2 Software design

B.2.1 Overall objectives

In scientific computing coding bugs could easily lead to erroneous conclusions. Therefore, software *quality* - defined here as the capability of the software to produce correct results - has been of major concern at all stages of software development. It has been achieved by focussing on code understability, mainteinability and adopting a modular test strategy, as it will be explained later. Since the overall goal of this study was to provide fast and efficient methods at high frequencies and, at such frequencies, the FEM requires operations on large matrices and vectors, *numerical efficiency* has been regarded of primary importance. Moreover, *portability* of the code has also been of concern. Portability relates to the use of a standard programming language common to many software/hardware environments. Initially, the application ran on a laptop running Microsoft Windows XP operating system. Later on, it has been ported on a cluster running Red Hat Enterprise Linux.

B.2.2 Required functionalities

AMADO implements the FEM for certain combinations of problem options:

- the convected Helmholtz equation and the Pridmore-Brown equation,
- rigid and lined wall boundary conditions,
- annular and cylindrical duct geometries,

- linear and quadratic Lagrange basis functions,
- numeric and symbolic (where possible) integration schemes,
- a number of mean-velocity profiles.

AMADO imports data obtained using a Runge-Kutta integration scheme and compare them with those calculated using FEM.

B.2.3 Design concepts

The object-oriented programming style has been adopted for the development of the AMADO software because it has been evaluated as the most suitable programming paradigm in order to achieve the overall objectives defined above. This sub-section explains in some details the rationale of this choice.

B.2.3.1 Objects to enhance modularity

In programming it is widely recognized that an effective way to manage complex projects is to break them down into a collection of sub-problems (modules). In procedural programming (such as legacy FORTRAN scientific programming [1]), modularity is obtained by organizing the code into separate procedures. Data structures (e.g., arrays) and procedures are separate entities, which interact only when data are passed to a specific procedure. Therefore, there always exists a main routine which stores and passes data to the appropriate procedures. This is called a *central control*-style of programming. When the problem becomes larger and more complex it is increasingly difficult to define and maintain an appropriate global data structure in the main routine which minimizes software dependencies among procedures. The program may easily become heavy with details of storage and a large number of 'if-then' conditions. Keeping software dependencies

---

[1] FORTRAN90 and FORTRAN2003 support object-based programming. See [77].

to a minimum among procedures becomes very challenging. More likely, software dependencies rise and the code becomes more error-prone because changes to any part of the program are likely to have some impact on other parts of the program.

The object-oriented programming overcomes this problem. Since its introduction in the late eighties, it “has become recognized as the almost unique successful paradigm for creating complex software” [103]. Every procedure can be associated to a data structure in an object. Instead of being concerned to write a main routine that passes adequate data to any procedure, focus is on defining objects which intrinsecally link data structures (attributes) and procedures (operations). Objects store information and perform some calculations on their attributes; they provide access to another objects or even create new objects. This leads to a *decentralized control*-style of programming (see, for example, [32]). A program then consists of objects which know how to relate to each other. Defining classes (of objects) is a natural extension of thinking to abstract objects and this enables the writing of a more readable code. The challenge is to make good use of this capability, that is a suitable decomposition of the system into classes and the definition of their operations.

Typically, data is embedded within objects, which means that objects can ’hide’ their own data. They can pass data to each other, but only through their interfaces. This is called *information hiding*. This control over access to data helps to build robust code because changes within a class do not require changes to the rest of the code (provided that the interface to the class is maintained unchanged). Moreover, separating “the incidental details of the implementation (e.g., the layout of the data used to store an object of the type) from the properties essential to the correct use of it (e.g., the complete list of functions that can access the data)” [112, Chap. 10] encorages conceptual integrity which leads to a better understability of the code.

It is helpful, at this point, to make an example: the implementation of a data structure associated with a one-dimensional mesh. It will be shown how the complex mathematical structure of a mesh can be clearly implemented with the use of classes and how its associated data can be accessed and manipulated much easier when using an object-oriented approach rather than a programming language in which only arrays are available, such as legacy FORTRAN.

The one-dimensional mesh data structure. A one-dimensional mesh consists of nodes and elements inter-connected. The information associated with a node include its cartesian coordinates, its global node index, whether it is located inside the domain or on the domain boundaries, whether or not a Dirichlet condition is enforced there, what are the elements it belongs to. Figure B.2.1(a) depicts a one-dimensional mesh and the information associated with it; two examples of global numbering are considered.

An example of data structure implementation using arrays only is presented in figure B.2.1(b). A list of the x-coordinates that define each node of the mesh is stored in a $N_{\text{glob}} \times 1$ array *coordsOfNodes*, where N_{glob} is the total number of nodes. This array is used to associates each node global index with its x-coordinate: the order of the nodes in this array reflects the node global numbering scheme. Each element (interval) is defined by its endpoints. A table of global indices corresponding to the left-hand side and right-hand side endpoints, respectively, for each interval are stored in a $N_{\text{e}} \times 2$ matrix *elements* (where N_{e} is the total number of elements). This table is implemented as a matrix of pointers into *coordsOfNodes*, that is, a matrix of variables which contain the address to the corresponding x-coordinate variable located at that address in memory. Finally, a $N_b \times 1$ array and a $N_d \times 1$ array, which contain the global indices of the nodes which lies on the boundary and the indices of the nodes which a Dirichlet condition applies to, respectively, can be defined. It is to be noted that the information on a single node is obtained by accessing each array by the appropriate index location. The information is spread over a number of arrays and the data structure hardly reflects the structure of the mathematical object. Moreover, it becames very challenging to maintain this structure when adding more nodal points to the elements in order to make use of Lagrange polynomials of higher order as shape functions.

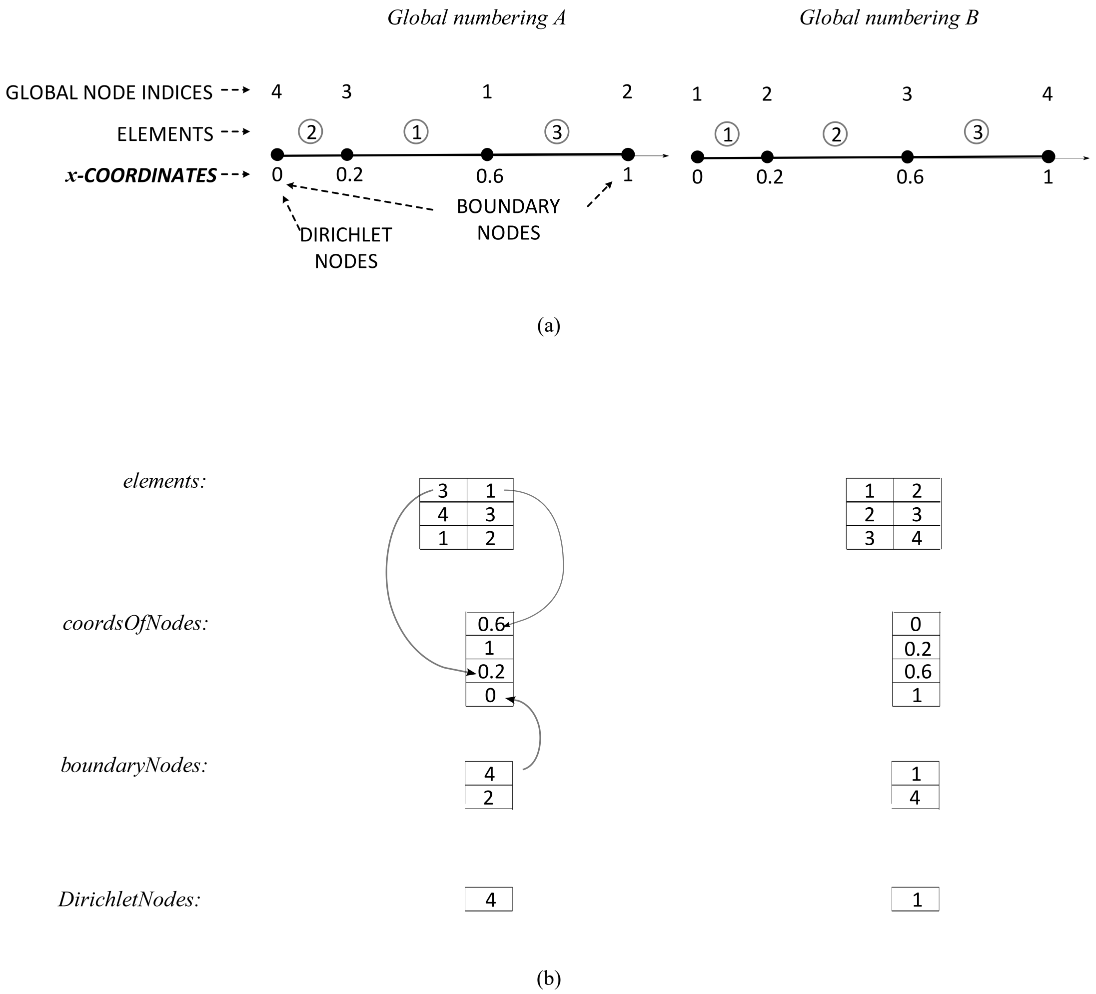

Figure B.2.1: The diagram represents: (a) two examples of global numbering associated with same one-dimensional mesh; (b) an implementation of a data structure using arrays only for the two examples of global numbering above. The solid arrows graphically represent pointers.

On the contrary, an object-oriented approach encorages to think about the objects that are actually used in the mathematical framework, such as mesh, element and node. A mesh is a collection of related data: it can be implemented as an object *Mesh*, which represents an aggregation of objects of class *Element*. Similarily, each *Element* consists of an aggregation of objects of class *Node*. Any objects of class *Node* contains all the required information. The manipulation of data can then be carried out by invoking specific methods of the class. For example, to get the Cartesian coordinates associated to a node called, say, *aNode* the following method can be defined

```
aNode.getCoordinates()
```

```
1  // solving the Algebraic Eigenvalue Problem (quadratic)
2      // -------------------------------------------------------
3      AA.resize(dim, dim);
4      BB.resize(dim, dim);
5  
6      vector<double> x_coord;
7      for (unsigned int i = 0; i < noNodes; i++)
8      {
9          for (unsigned int h = 0; h < noNodes; h++)
10         {
11             AA(i,h) = zeroMatrix(i,h);
12             BB(i,h) = idMatrix(i,h);
13             AA(i, h + noNodes) = idMatrix(i,h);
14             BB(i, h + noNodes) = zeroMatrix(i,h);
15             AA(i + noNodes, h) = -1.0 * matrixCoeffs[0](i,h);
16             BB(i + noNodes, h) = zeroMatrix(i,h);
17             AA(i + noNodes, h + noNodes) = -1.0 * matrixCoeffs[1](i,h);
18             BB(i + noNodes, h + noNodes) = matrixCoeffs[2](i,h);
19         }
20         x_coord.push_back( pMesh_1d->getNodes()[i].getCoord()[0] );
21     }
22     genEig(x_coord);
```

Figure B.2.2: Code extract from *EigPrb _1d _ax _uni _cal* .

An example of the use of this method is provided in line 20 of the code extract of figure B.2.2.

The classes used to implement the mathematical structure of a mesh in AMADO using the object-oriented programming paradigm and their relationshipsare depicted in figure B.2.3, where the UML2 graphical notation has been used[2]. The arrow with the filled diamond represents the UML2 'composition' relationship: objects of class *Element* are part of objects of class *Mesh*. The symbol '1' stands for a single-valued multiplicity: an element has only one mesh as owner, as the definition of composition implies. The arrow with the empty diamond represents the UML2 less strictly defined 'aggregation' relationship: objects of class *Node* are part of objects of class *Element*, but a node can have one element - this is the case of the endpoints of the domain - or two elements. Therefore the symbol '1:2' is used. The simbol '*' is an indication of multivalued multiplicity: any mesh has many elements, as well as any element has many nodes (at least two).

---

[2] For a description of the UML2 conventions, see, for example, reference [16].

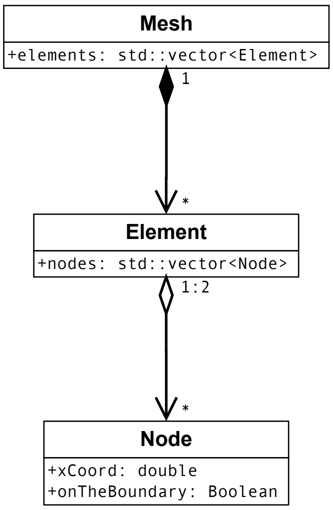

Figure B.2.3: The relationship of classes used to implement a one-dimensional mesh using the object-oriented approach.

B.2.3.2 Organizing around change: the convenience of class hierarchies

The object-oriented programming style supports *class hierarchies* (*inheritance*), which promote code reuse and facilitates code extension at a later time. Abstract classes may be used to define the overall structure of the hierarchy and implement methods that are common to all derived classes, which are lower in the hierarchy. This feature has been particularly convenient for the way the AMADO code has been developed and validated, as explained in the following examples.

The EigPrb_1d family. The *EigPrb_1d* and *Mode_1d* class families implement the finite element computations and the ordering of the modes. Figure B.2.6 shows an UML2 class diagram describing their hierarchy, properties, methods and relationships. The*EigPrb_1d* abstract class contains the method *arrangeModes()*, which is common to all its derived classes. One level lower in the hierarchy, the*EigPrb_1d_axi* abstract class contains the method *solve()*, which computes the generalised eigenexpansion. The derived classes *EigPrb_1d_axi_cal_uni* and *EigPrb_1d_axi_cal_she* implement the computation of the global matrices for the convected Helmholtz problem and the Pridmore-Brown problem, respectively. The former was implemented first, and it was validated against exact solutions. The latter was added at a later time and, with this code development approach, no changes to code written previously were necessary.

The use of abstract container classes. The routines that handle vectors and matrices has been written at a level of abstraction sufficient to allow almost any existing C++ vector/matrix class library to be used [3]. These routines do not need to know which storage model is used. The code is then easy to read (a sort of MATLAB script). In this way, suitable, "highly tuned" vector/matrix class libraries (such as those dealing efficiently with sparse matrices) were implemented at a later time in a flexible manner.

B.2.4 Key elements in the design

B.2.4.1 The model-analysis separation design

There are three main steps a finite element code has to perform

- creating a mesh on the domain Ω
- assembling the global matrices
- solving the algebraic eigenvalue problem

The benefits of decomposing a finite element program into the modelling of the problem domain (that is, the generation of the mesh) and the finite element analysis are thoroughly discussed by Heng & Mackie [51]. These authors reckon that with no clear distinction between domain modelling- and analysis-related code " a finite element system can quickly become too large and complicated to maintain efficiently". They consider

---

[3] C++ *per se* does not provide matrix functionality. On the other hand, thanks to the object-oriented programmability of C++ vector and matrix classes can be implemented. Many libraries provide vector and matrix classes which include fundamental operations.

```
1  int main(int argc, char* argv[])
2  {
3  ...
4  // Creating mesh
5  // --------------
6  Mesh_1d AxiMesh(p,
7            is_hardWalledCase,
8            coordsOfVertices_fileName,
9            bndVerticesAndAdm_fileName,
10           mesh_completeDirPath,
11           elements_fileName);
12
13 // Solving the cubic eigenvalue problem
14 // ------------------------------------
15 EigPrb_1d_axi_cal_she AxiCalShe(is_hardWalled,
16           cHelmholtzNo,
17           coreMachNo,
18           nMax,
19           m,
20           & AxiMesh,
21           meanVelocityProfileTypeNo,
22           bLThickness_in,
23           bLThickness_out,
24           slipVelocity_in,
25           slipVelocity_out);
26
27 // pointer to object of class 'EigPrb_1d_axi'
28 EigPrb_1d_axi_cal * pEigPrb_1d_axi_cal_she = & AxiCalShe;
29
30 // polymorphism
31 pEigPrb_1d_axi_cal_she->solve();
32
33 ...
34
35 return 0;
36 }
```

Figure B.2.4: Outline of the *main* function.

the separation a best practice in order to make both mainteinance and subsequent extensions of the software easier because any change in the code of one subsystem will have reduced impact on the other (in other words, the coupling between the two subsystems is reduced). They name this design pattern *model-analysis separation*.

Figure B.2.4 shows the very essence of the code, which is split into: (a) generation of the mesh (line 6) and (b) analysis-related code (line 15 to end). Figure B.2.5 shows the hierarchy and interactions of classes that are used to represent the problem domain. The hierarchy and interactions of classes which are used to implement the finite element computations and store the computation results are depicted in figure B.2.6.

B.2.4.2 The assembling procedure

The assembling is carried out by scanning the elements of the mesh. When an element with nodes i, j is encountered, the corresponding element A_{ij} in the global element

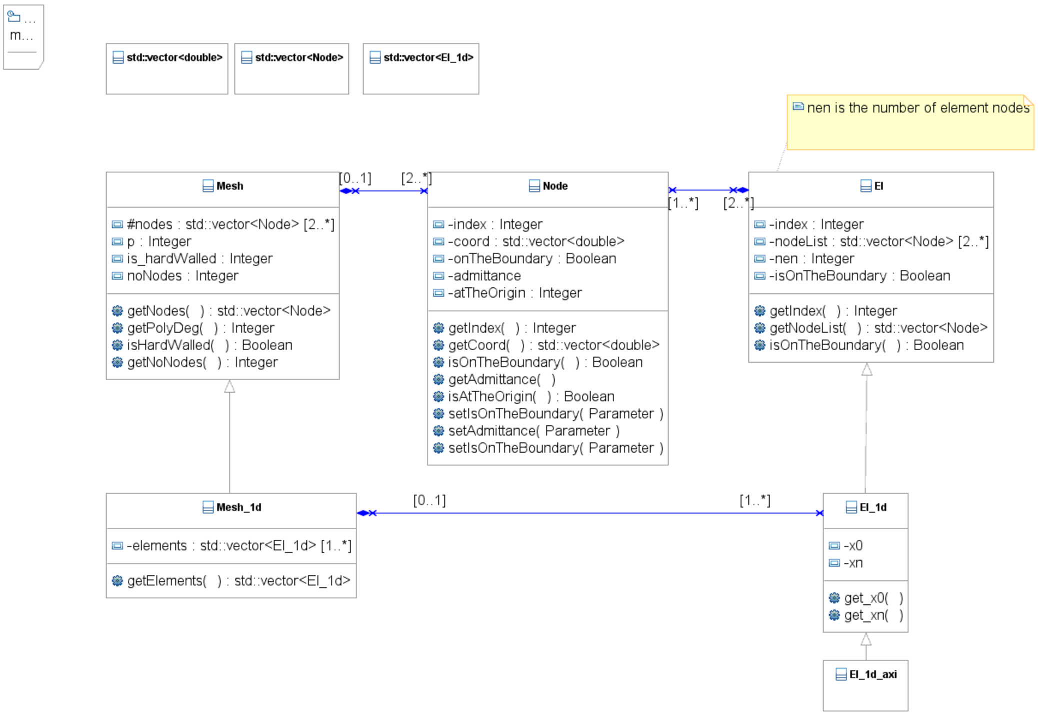

Figure B.2.5: UML2 class diagram showing the hierarchy of the *Mesh*, *Node*, and *Element* class families, their properties and methods and their relationships.

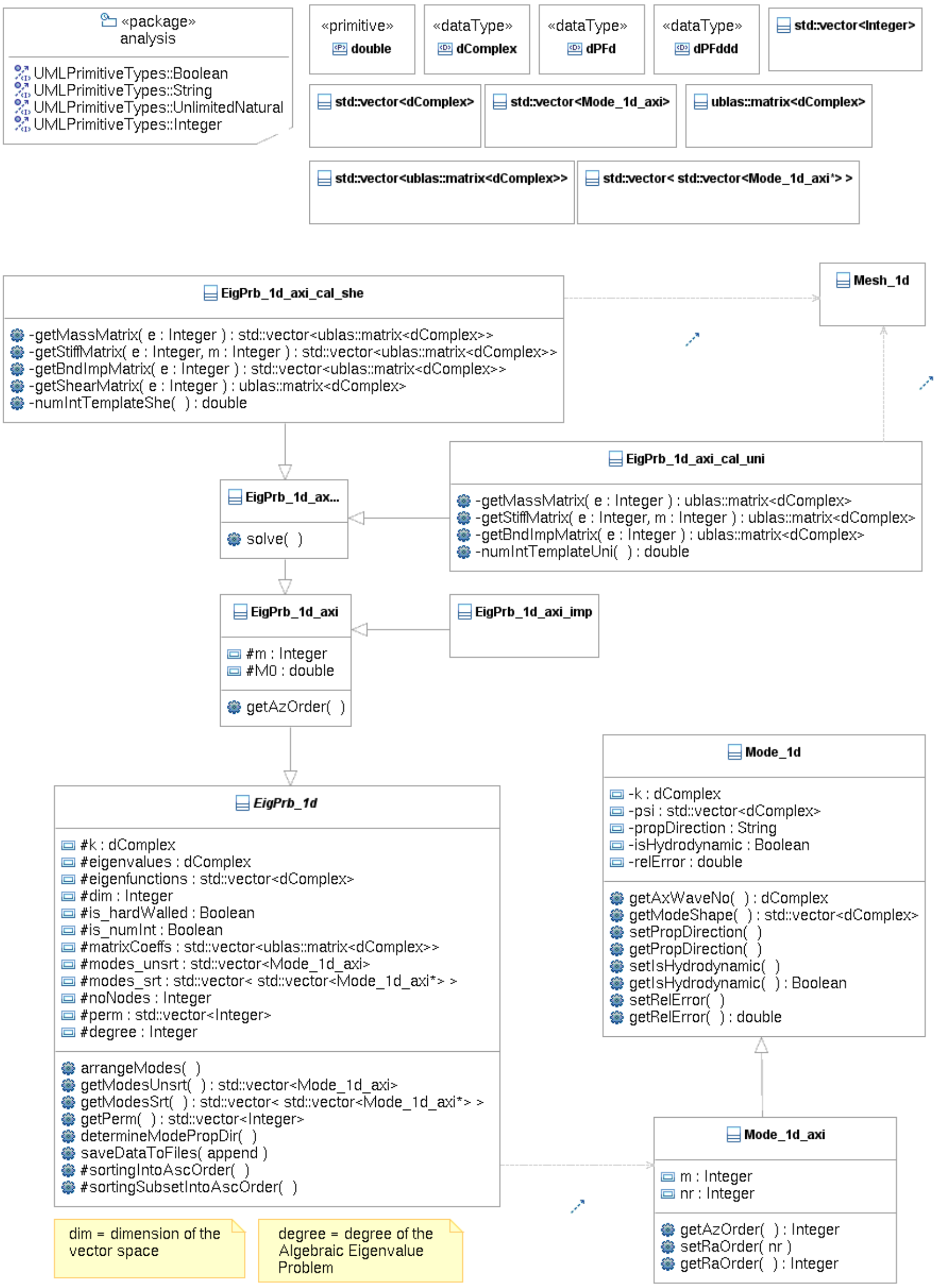

Figure B.2.6: UML2 class diagram showing the hierarchy, properties, methods and relationships of the *EigenPrb_1d* and *Mode_1d* class families. The abbreviations used in the class names correspond to: 1d, one-dimensional; axi, axisymmetric; imp, imported results from .csv file; cal, calculated results; uni, case of uniform mean flow (convected Helmholtz problem); she, case of sheared mean flow (Pridmore-Brown problem).

```
Initialize $K$ to the zero matrix
for $e = 1, 2, \dots, N_{\text{e}}$
    for $p = 1, 2, \dots, N_{\text{en}}$
        Find $i = n(e, p)$
        for $q = 1, 2, \dots, N_{\text{en}}$
            Find $j = n(e, p)$
            Compute $K^e_{p,q}$ and add it to $K_{ij}$
            If $i \neq j$, add it to$K_{ji}$.
```

Figure B.2.7: Pseudo-code fragment showing the element-oriented algorithm for computing K(case of the convected Helmholtz problem).

```
// Assembling C0, C1 and C2
// ------------------------------
ne = pMesh_1d->getElements().size();

for (int e = 0; e < ne; e++)
{
        ublas::matrix<dComplex> M = this->getMassMatrix(e);
        ublas::matrix<dComplex> K = this->getStiffMatrix(e, m);
        ublas::matrix<dComplex> Z = this->getBndImpMatrix(e);
        nen = pMesh_1d->getElements()[e].getNodeList().size();

        for (int p = 0; p < nen; p++)
        {
                int i = pMesh_1d->getElements()[e].getNodeList()[p].getIndex();

                for (int q = 0; q < nen; q++)
                {
                        int j = pMesh_1d->getElements()[e].getNodeList()[q].getIndex();

                        matrixCoeffs[0](i,j) += pow(k,2) * M(p,q) - K(p,q);
                        matrixCoeffs[1](i,j) += -2 * M0 * pow(k,2) * M(p,q);
                        matrixCoeffs[2](i,j) += pow(k,2) * ( pow(M0,2) - 1 ) * M(p,q);

                        if ( pMesh_1d->getElements()[e].isOnTheBoundary() )
                        {
                                matrixCoeffs[0](i,j) += -imUnit * k * Z(p,q);
                                matrixCoeffs[1](i,j) += -2 * M0 * ( -imUnit * k * Z(p,q) );
                                matrixCoeffs[2](i,j) += pow(M0,2) * ( -imUnit * k * Z(p,q) );
                        }
                }
        }
}
```

Figure B.2.8: Implementation of the assembling procedure (case of the convected Helmholtz problem).

matrices are incremented by the corresponding contribution from the integral over element. The procedure for assembling the global matrix K is described by the pseudo-code fragment of figure B.2.7. The code implementation of the assembling procedure for all global matrices in the case of the convected Helmholtz problem is provided in figure B.2.8.

B.2.4.3 Mode ordering

A robust sorting algorithm for modes has been implemented. The modes are first identified as upstream or downstream propagating modes based on their group velocity. If this is positive, then it is downstream propagating mode, whereas if it is negative, it is upstream propagating mode. The evaluation of the group velocity is carried out by implementing an algorithm proposed by Moinier & Giles [78]. Then, downstream modes are classified as predominantly acoustic in nature or predominantly convected with the mean flow according to the location of their axial wavenumber in the complex plane. The code implementation strategy for ordering the modes is outlined in figure B.2.9. It is based on the use of vectors of vectors using the C++ Standard Template Library [99]. The use of permutation arrays has replaced the practice of copying columns of tables of data when sorting on multiple fields.

Finally, modes in each of the categories are sorted according to the increasing magnitude of the absolute value of the imaginary part of the axial wavenumber, which is proportional to the attenuation rate. In the case of modes whose axial wavenumber has zero imaginary part(pure acoustic modes which occur with uniform flow only), sorting is according to the decreasing magnitude of the absolute value of the real part of the axial wavenumber. A flow diagram of the algorithm used to sort modes whose axial wavenumber has zero imaginary part is shown in figure B.2.10. The algorithm's input variables *vec1_sort* and *vec2* are the array containing the absolute value of the imaginary part of the axial wavenumber, sorted according to the increasing magnitude, and the array containing the inverse of the absolute value of the real part of the axial wavenumber, respectively.

B.2.4.4 About the computation of the generalized eigenexpansion

In the IMSL Library User's Guide [92] a description of the algorithm used to compute the generalized eigenexpansion is provided. 'The function *imsl _c _geneig* uses the QZ

Figure B.2.9: Outline of the code implementation strategy for ordering the modes.

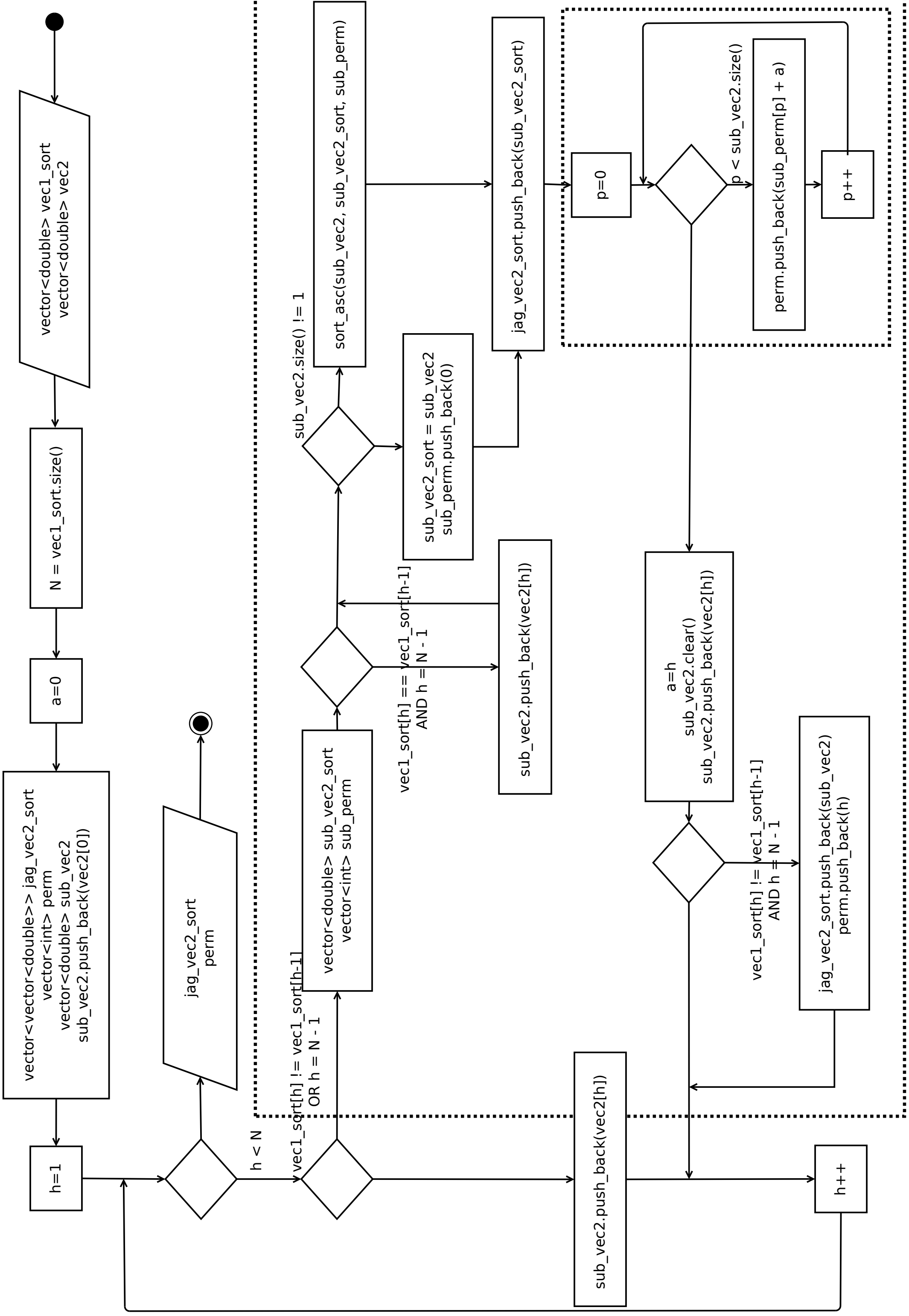

Figure B.2.10: Flow diagram explaining the algorithm used to sort modes whose axial wavenumber has zero imaginary part. The function *sort_asc(sub_vec2, sub_vec2_sort, sub_perm)* sorts the elements of the array *sub_vec2* into ascending order, storing the sorted array in *sub_vec2_sort* and the resulting permutation in *sub_perm*.

algorithm to compute the eigenvalues and eigenvectors of the generalized eigensystem $Ax = \lambda Bx$, where A and B are complex matrices of order n. The eigenvalues for this problem can be infinite, so α and β are returned instead of λ. If β is nonzero, $\lambda = \alpha/\beta$. The first step of the QZ algorithm is to simultaneously reduce A to upper-Hessenberg form and B to upper-triangular form. Then, orthogonal transformations are used to reduce A to quasi-upper-triangular form while keeping B upper triangular. The generalized eigenvalues and eigenvectors for the reduced problem are then computed. The function *imsl _c _geneig* is based on the QZ algorithm due to Moler & Stewart [79].

B.2.4.5 Other implementation features

1. The computational kernel, which handles the algebraic calculations including the generalized non-hermitian eigenproblem solver, has been implemented in a way that switching from a solver to another one does not require major code modification. The solver *imsl_z_geneig* in IMSL C Math library [92] was the initial choice due to its extensive documentation and installation support. However, this is proprietary software. Other solvers are available as free software for Unix-like platforms.

2. Input and output data are stored in ’self-describing’ ASCII files, i.e. files that include metadata annotations, which may be parsed by external application programs at a later time.

3. Output filesare organized in a hierarchical tree of directories where calculation results corresponding to some set of input parameters are stored in folders with a unique name. For this purpose, the C++ Boost.Filesystem library has been included in the solution to provide a portable mechanism for representing paths in C++ programs irrespective of the platform used (Windows or Unix).

4. Data visualization has been decoupled from the ’CPU-critical’ C++ code for a more efficient management of computer memory and more flexible inspection of

results. It has been implemented using Python and the scientific plotting library DISLIN. The Python scripting programming style has demonstrated to be a very convenient tool here for traversing directory trees in search for the appropriate data files.

Bibliography

[1] Achunche, I. M. (2010). *Acoustic optimisation and prediction of sound propagation in turbofan engine ducts*. PhD thesis, University of Southampton.

[2] Agency, E. P. (1971). *Public Hearings On Noise Abatement And Control Manufacturing And Transportation Noise*. Number 905R71107B. Chicago, Illinois: U.S. Environmental Protection Agency.

[3] Astley, R., Vjt, H., Nj, B., & Mcalpine, K. A. (2006). Acoustic scattering by an axially-segmented turbofan inlet duct liner at supersonic fan speeds. *Journal Of Sound And Vibration*, 294(4-5), 780–806.

[4] Astley, R. J. & Eversman, W. (1978). Finite-element method for transmission in non-uniform ducts without flow: comparison with method of weighted residuals. *Journal of Sound and Vibration*, 57(3), 367–388.

[5] Astley, R. J. & Eversman, W. (1979). Finite-element formulation of the eigenvalue problem in lined ducts with flow. *Journal of Sound and Vibration*, 65(1), 61–74.

[6] Astley, R. J. & Eversman, W. (1981). Acoustic transmission in non-uniform ducts with mean flow, part ii: the finite element method. *Journal of Sound and Vibration*, 74(1), 103–121.

[7] Astley, R. J., Sugimoto, R., & Mustafi, P. (2011). Computational aero-acoustics for fan duct propagation and radiation. current status and application to turbofan liner optimisation. *Journal of Sound and Vibration*, 330(16), 3832–3845.

[8] Astley, R. J., Sugimoto, R., Mustafi, P., Kewin, M., & Achunche, I. (2010). Liner optimisation for turbofan ducts-towards a fully automated approach. In *16th AIAA/CEAS Aeroacoustics Conference, AIAA-2010-3826, Stockholm, Sweden* (pp. 7–9).

[9] Atassi, H. M. (1997). Aeroacoustics of nonuniform flows. *AIAA Paper*, (pp. 97–0378).

[10] Atassi, O. V. (2003). Computing the sound power in non-uniform flow. *Journal of sound and vibration*, 266(1), 75–92.

[11] Batchelor, G. K. (2000). *An introduction to fluid dynamics*. Cambridge university press.

[12] Bayliss, A. & Turkel, E. (1982). Far field boundary conditions for compressible flows. *Journal of Computational Physics*, 48(2), 182–199.

[13] Bender, C. M. & Orszag, S. A. (1999). *Advanced Mathematical Methods for Scientists and Engineers I*. Springer Science & Business Media.

[14] Bers, A. (1983). Space-time evolution of plasma instabilities-absolute and convective. In *Basic plasma physics. 1*. North-Holland.

[15] Boden, H. (2012). *Recent Advances in IC-Engine Exhaust and Intake System Acoustic Source Characterization*. Technical report, SAE Technical Paper.

[16] Booch, G., Rumbaugh, J., & Jacobson, I. (2005). *Unified Modeling Language User Guide, The (2Nd Edition) (Addison-Wesley Object Technology Series)*. Addison-Wesley Professional.

[17] Brambley, E. J. (2009). Fundamental problems with the model of uniform flow over acoustic linings. *Journal of Sound and Vibration*, 322(4-5), 1026–1037.

[18] Brambley, E. J. (2011). Well-posed boundary condition for acoustic liners in straight ducts with flow. *AIAA journal*, 49(6), 1272–1282.

[19] Brambley, E. J., Darau, M., & Rienstra, S. W. (2012). The critical layer in linear-shear boundary layers over acoustic linings. *Journal of Fluid Mechanics*, 710, 545–568.

[20] Brambley, E. J. & Peake, N. (2008). Stability and acoustic scattering in a cylindrical thin shell containing compressible mean flow. *Journal of Fluid Mechanics*, 602, 403–426.

[21] Brenner, S. & Scott, R. (2007). *The Mathematical Theory of Finite Element Methods*. Springer New York.

[22] Briggs, R. J. (1964). *Electron-stream interactions with plasmas, Res. Monograph No. 29*. MIT Press, Cambridge, Massachusetts.

[23] Brooks, C. J. (2007). *Prediction and control of sound propagation in turbofan engine bypass ducts*. PhD thesis, University of Southampton.

[24] Campos, L. & Serrao, P. (2013). On the discrete and continuous spectrum of acoustic-vortical waves. *International Journal of Aeroacoustics*, 12(7-8), 743–781.

[25] Campos, L. M. B. C., Legendre, C., & Sambuc, C. (2014). On the acoustics of an impedance liner with shear and cross flow. In *Proceedings of the Royal Society of London A: Mathematical, Physical and Engineering Sciences*, volume 470 (pp. 20130732).: The Royal Society.

[26] Cantrell, R. H. & Hart, R. W. (1964). Interaction between sound and flow in acoustic cavities: Mass, momentum, and energy considerations. *The Journal of the Acoustical Society of America*, 36(4), 697–706.

[27] Chu, B.-T. & Kovásznay, L. S. G. (1958). Non-linear interactions in a viscous heat-conducting compressible gas. *Journal of Fluid Mechanics*, 3(05), 494–514.

[28] Coleman, G. N. & Sandberg, R. D. (2010). *A primer on direct numerical simulation of turbulence-methods, procedures and guidelines*. Technical report, University of Southampton.

[29] Doak, P. E. (1973). Fundamentals of aerodynamic sound theory and flow duct acoustics. *Journal of Sound and Vibration*, 28(3), 527–561.

[30] Doak, P. E. & Vaidya, P. G. (1970). Attenuation of plane wave and higher order mode sound propagation in lined ducts. *JOURNAL OF SOUND AND VIBRATION*, 12(2), 201–&.

[31] Dubois-Pelerin, Y. & Pegon, P. (1998). Linear constraints in object-oriented finite element programming. *Computer Methods in Applied Mechanics and Engineering*, 154(1-2), 31–39.

[32] Dubois-Pelerin, Y., Zimmermann, T., & Bomme, P. (1992). Object-oriented finite-element programming .1. governing principles. *Computer Methods In Applied Mechanics And Engineering*, 98(2), 291–303.

[33] Eversman, W. (1970). Effect of mach number on tuning of an acoustic lining in a flow duct. *Journal of the Acoustical Society of America*, 48(2), 425–&.

[34] Eversman, W. (1971). Effect of boundary layer on the transmission and attenuation of sound in an acoustically treated circular duct. *The Journal of the Acoustical Society of America*, 49(5A), 1372–1380.

[35] Eversman, W. (1972). Representation of a 1n power law boundary layer in the sheared flow acoustic transmission problem. *Journal of Sound and Vibration*, 24(4), 459–469.

[36] Eversman, W. (1973). Approximation for thin boundary layers in the sheared flow duct transmission problem. *The Journal of the Acoustical Society of America*, 53(5), 1346–1350.

[37] Eversman, W. (1975). Computation of axial and transverse-wave numbers for uniform 2-dimensional ducts with flow using a numerical-integration scheme. *Journal Of Sound And Vibration*, 41(2), 252–255.

[38] Eversman, W. (1991). Theoretical models for duct acoustic propagation and radiation. In H. Hubbard (Ed.), *Aeroacoustics Of Flight Vehicles: Theory And Practise, Volume 2: Noise Control*. NASA.

[39] Eversman, W. & Beckemeyer, R. J. (1972). Transmission of sound in ducts with thin shear layers—convergence to the uniform flow case. *The Journal of the Acoustical Society of America*, 52(1B), 216–220.

[40] Fisher, M. J., Mcalpine, A., & Tester, B. J. (2007). ”buzz-saw” noise: A comparison of modal measurements with an improved prediction method. *Journal Of Sound And Vibration*, 306, 419–443.

[41] Fournier, G. (2011). *Report on the First Scientific Workshop*. Technical report, European Aviation Noise Research Network (X-NOISE).

[42] Gabard, G. (2013). A comparison of impedance boundary conditions for flow acoustics. *Journal of Sound and Vibration*, 332(4), 714–724.

[43] Gabard, G. & Astley, R. J. (2008). A computational mode-matching approach for sound propagation in three-dimensional ducts with flow. *Journal of Sound and Vibration*, 315(4-5), 1103–1124.

[44] Gogate, G. R. & Munjal, M. L. (1996). Sound propagation in ducts with bulk reacting lining in the presence of laminar mean flow. *Journal of the Acoustical Society of America*, 99(3), 1779–1782.

[45] Goldstein, M. E. (1976). *Aeroacoustics*, volume 1. New York, McGraw-Hill International Book Co.

[46] Goldstein, M. E. (1978). Unsteady vortical and entropic distorsions of potential flows round arbitrary obstacles. *Journal of Fluid Mechanics*, 89(DEC), 433–468.

[47] Goldstein, M. E. (1979). Scattering and distortion of the unsteady motion on transversely sheared mean flows. *Journal of Fluid Mechanics*, 91(APR), 601–632.

[48] Goldstein, M. E., Afsar, M. Z., & Leib, S. J. (2013). *Structure of the Small Amplitude Motion on Transversely Sheared Mean Flows*. Technical report, National Aeronautics and Space Administration (NASA).

[49] Golubev, V. V. & Atassi, H. M. (1998). Acoustic-vorticity waves in swirling flows. *Journal of Sound and Vibration*, 209(2), 203–222.

[50] Hall, K. C. & Crawley, E. F. (1989). Calculation of unsteady flows in turbomachinery using the linearized euler equations. *AIAA Journal*, 27(6), 777–787.

[51] Heng, B. C. P. & Mackie, R. I. (2009). Using design patterns in object-oriented finite element programming. *Computers & Structures*, 87(15), 952–961.

[52] Huerre, P. & Monkewitz, P. A. (1985). Absolute and convective instabilities in free shear layers. *Journal of Fluid Mechanics*, 159, 151–168.

[53] ICAO (2013). *ICAO Environmental Report 2013 - Aviation and Climate Change*. Technical report, International Civil Aviation Administration (ICAO).

[54] Ihlenburg, F. (2006). *Finite Element Analysis of Acoustic Scattering*. Springer New York.

[55] Ihlenburg, F. & Babuska, I. (1995a). Dispersion analysis and error estimation of galerkin finite element methods for the helmholtz equation. *International Journal for Numerical Methods in Engineering*, 38(22), 3745–3774.

[56] Ihlenburg, F. & Babuska, I. (1995b). Finite element solution of the helmholtz equation with high wave number part i: The h-version of the fem. *Computers and Mathematics with Applications*, 30(9), 9–37.

[57] Ihlenburg, F. & Babuska, I. (1997). Finite element solution of the helmholtz equation with high wave number .2. the h-p version of the fem. *SIAM Journal on Numerical Analysis*, 34(1), 315–358.

[58] Ingard, U. (1959). Influence of fluid motion past a plane boundary on sound reflection, absorption, and transmission. *Journal of the Acoustical Society of America*, 31, 1135–1136.

[59] Jones, A. D. (1984). Modelling the exhaust noise radiated from reciprocating internal combustion engines - a literature review. *Noise Control Engineering Journal*, 23(1), 12–31.

[60] Jones, M. G., Parrott, T. L., & Watson, W. R. (2003). Comparison of acoustic impedance eduction techniques for locally-reacting liners. *AIAA paper*, 3306, 2003.

[61] Joseph, P., Morfey, C. L., & Lowis, C. R. (2003). Multi-mode sound transmission in ducts with flow. *Journal of sound and vibration*, 264(3), 523–544.

[62] Joshi, M. C., Kraft, R. E., & Son, S. Y. (1982). Analysis of sound propagation in annular ducts with segmented treatment and sheared flow. In *AIAA 20th Aerospace Sciences Meeting, January 11-14, Orlando, Florida*.

[63] Kempton, A. (2011). Acoustic liners for modern aero-engines. In *15th CEAS-ASC Workshop and 1st Scientific Workshop of X-Noise EV*.

[64] Knabner, P. & Angerman, L. (2010). *Numerical Methods for Elliptic and Parabolic Partial Differential Equations*. Springer New York.

[65] Ko, S. H. (1971). Sound attenuation in lined rectangular ducts with flow and its application to reduction of aircraft engine noise. *Journal of the Acoustical Society of America*, 50(6), 1418–&.

[66] Ko, S. H. (1972). Sound attenuation in acoustically lined circular ducts in the presence of uniform flow and shear flow. *Journal of Sound and Vibration*, 22(2), 193–210.

[67] Kousen, K. A. (1999). *Eigenmodes of Ducted Flows With Radially-Dependent Axial and Swirl Velocity Components*. Technical report, National Aeronautics and Space Administration (NASA).

[68] Kovasznay, L. S. G. (1988). Turbulence in supersonic flow. *Journal of the Aeronautical Sciences (Institute of the Aeronautical Sciences)*, 20(10).

[69] Landau, L. D. & Lifshitz, E. M. (1987). *Fluid mechanics, 2nd*. Pergamon Press, Oxford, sect.

[70] Law, T. R. (2008). *Multi-segmented liner optimisation for mixed exhaust aero-engines*. PhD thesis, University of Cambridge.

[71] Legendre, C. (2015). *On the interactions of sound waves and vortices*. LULU Press.

[72] Leylekian, L., Lebrun, M., & Lempereur, P. (2014). An overview of aircraft noise reduction technologies. *AerospaceLab*, (6), p. 1–15.

[73] Mackie, R. I. (1992). Object oriented programming of the finite-element method. *International Journal For Numerical Methods In Engineering*, 35(2), 425–436.

[74] Mackie, R. I. (1997). Using objects to handle complexity in finite element software. *Engineering with Computers*, 13(2), 99–111.

[75] Mackie, R. I. (1999). Object-oriented finite element programming-the importance of data modelling. *Advances in Engineering Software*, 30(9-11), 775–782.

[76] Möhring, W. (1971). Energy flux in duct flow. *Journal of Sound and Vibration*, 18(1), 101–109.

[77] Metcalf, M., Reid, J. K., & Cohen, M. (2004). *Fortran 95/2003 Explained*, volume 416. Oxford University Press Oxford.

[78] Moinier, P. & Giles, M. B. (2005). Eigenmode analysis for turbomachinery applications. *Journal of Propulsion And Power*, 21(6), 973–978.

[79] Moler, B. C. & Stewart, G. W. (1973). Algorithm for generalized matrix eigenvalue problems. *Siam Journal on Numerical Analysis*, 10(2), 241–256.

[80] Morfey, C. L. (1971). Acoustic energy in non-uniform flows. *Journal of Sound and Vibration*, 14(2), 159–170.

[81] Mungur, P. & Gladwell, G. M. L. (1969). Acoustic wave propagation in a sheared fluid contained in a duct. *Journal of Sound and Vibration*, 9(1), 28–48.

[82] Mungur, P. & Plumblee, H. E. (1969). Propagation and attenuation of sound in a soft-walled annular duct containing a sheared flow. *NASA Special Publication*, 207, 305.

[83] Munjal, M. L. (2014). *Acoustics of Ducts and Mufflers*. Wiley.

[84] Murray, P. B., Ferrante, P., & Scofano, A. (2005). Manufacturing process and boundary layer influences on perforate liner impedance. *AIAA Paper*, 2849, 2005.

[85] Myers, M. K. (1980). On the acoustic boundary-condition in the presence of flow. *Journal of Sound and Vibration*, 71(3), 429–434.

[86] Myers, M. K. (1986). An exact energy corollary for homentropic flow. *Journal of Sound and Vibration*, 109(2), 277–284.

[87] Myers, M. K. (1991). Transport of energy by disturbances in arbitrary steady flows. *Journal of Fluid Mechanics*, 226, 383–400.

[88] Myers, M. K. & Chuang, S. L. (1984). Uniform asymptotic approximations for duct acoustic modes in a thin boundary-layer flow. *AIAA Journal*, 22, 1234–1241.

[89] Nayfeh, A. H. (1973). Effect of the acoustic boundary layer on the wave propagation in ducts. *The Journal of the Acoustical Society of America*, 54(6), 1737–1742.

[90] Nayfeh, A. H., Kaiser, J. E., & Shaker, B. S. (1974). Effect of mean-velocity profile shapes on sound transmission through two-dimensional ducts. *Journal of Sound and Vibration*, 34(3), 413–423.

[91] Nayfeh, A. H., Kaiser, J. E., & Telionis, D. P. (1975). Acoustics of aircraft engine-duct systems. *AIAA Journal*, 13(2), 130–153.

[92] Numerics, V. (2006). *ISML C Numerical Library, Volume 1: C Math Library User's Guide*. Visual Numerics Inc.

[93] Oertel, H., Erhard, P., Asfaw, K., Etling, D., Muller, U., Riedel, U., Sreenivasan, K. R., & Warnatz, J. (2010). *Prandtl-essentials of fluid mechanics*, volume 158. Springer Science & Business Media.

[94] Olivieri, O., McAlpine, A., & Astley, R. J. (2009). Numerical calculation of pressure modes at high frequencies in lined ducts with a shear flow. In *EURONOISE 2009* Edinburgh, UK.

[95] Olivieri, O., McAlpine, A., & Astley, R. J. (2010). Determining the pressure modes at high frequencies in lined ducts with a shear flow. In *16th AIAA/CEAS Aeroacoustics Conference* Stockholm, Sweden.

[96] Organisation, I. C. A. (2006). *Convention on International Civil Aviation*. International Civil Aviation Organisation, ninth edition edition.

[97] Peake, N. & Parry, A. B. (2012). Modern challenges facing turbomachinery aeroacoustics. *Annual Review of Fluid Mechanics*, 44, 227–248.

[98] Pierce, A. (2007). Basic linear acoustics. In *Springer Handbook of Acoustics* (pp. 25–111). Springer.

[99] Plauger, P. J., Lee, M., Musser, D., & Stepanov, A. A. (2000). *C++ Standard Template Library*. Prentice Hall PTR.

[100] Plumblee, H. E. & Dean, P. D. (1973). Sound measurements within and in the radiated field of an annular duct with flow. *Journal of Sound and Vibration*, 28(4), 715–IN1.

[101] Powell, J. S. & Clemans, A. (2000). *NASA subsonic jet transport noise reduction research*. Technical report, National Aeronautics and Space Administration (NASA).

[102] Pozrikidis, C. (2014). *Introduction to Finite and Spectral Element Methods Using MATLAB, Second Edition*. Taylor & Francis.

[103] Press, W. H. (2007). *Numerical Recipes 3rd Edition: The Art of Scientific Computing*. Cambridge University Press.

[104] Pridmore-Brown, D. C. (1958). Sound propagation in a fluid flowing through an attenuating duct. *The Journal of the Acoustical Society of America*, 30(7), 670–670.

[105] Rice, E. J. (1968). Attenuation of sound in soft walled circular ducts. *NASA TM X-52442*.

[106] Rice, E, J. (1979). Optimum wall impedance for spinning modes - correlation with mode cutoff ratio. *Journal Of Aircraft*, 16(5), 336–343.

[107] Rice, T. G., Heidmann, E. J., & Sofrin, M. F. (1979). Modal propagation angles in a cylindrical duct with flow and their relation to sound radiation. In *17th Aiaa Aerospace Sciences Meeting , New Orleans, La.*

[108] Rienstra, S. W. (2003). A classification of duct modes based on surface waves. *Wave Motion*, 37(2), 119–135.

[109] Rienstra, S. W. (2006). Impedance models in time domain, including the extended helmholtz resonator model. *AIAA paper*, 2686, 2006.

[110] Rienstra, S. W. & Darau, M. (2011). Boundary-layer thickness effects of the hydrodynamic instability along an impedance wall. *Journal of Fluid Mechanics*, 671, 559–573.

[111] Rienstra, S. W. & Hirschberg, A. (2015). *An Introduction to Acoustics*. Eindhoven University of Technology.

[112] Stroustrup, B. (2013). *The C++ Programming Language*. Pearson Education.

[113] Tack, D. H. & Lambert, R. F. (1965). Influence of shear flow on sound attenuation in a lined duct. *The Journal of the Acoustical Society of America*, 38(4), 655–666.

[114] Tam, C. K. W. & Auriault, L. (1998). The wave modes in ducted swirling flows. *Journal of Fluid Mechanics*, 371, 1–20.

[115] Tam, C. K. W. & Webb, J. C. (1993). Dispersion-relation-preserving finite difference schemes for computational acoustics. *Journal of computational physics*, 107(2), 262–281.

[116] Tester, B. J. (1973a). The propagation and attenuation of sound in lined ducts containing uniform or 'plug' flow. *Journal of Sound and Vibration*, 28(2), 151–203.

[117] Tester, B. J. (1973b). Some aspects of 'sound' attenuation in lined ducts containing inviscid mean flows with boundary layers. *Journal of Sound and Vibration*, 28(2), 217–245.

[118] Thomas, R. H., Gerhold, C. H., Farassat, F., Santa Maria, O. L., Nuckols, W. E., & DeVilbiss, D. W. (1995). Far field noise of the 12 inch advanced ducted propeller simulator. *AIAA Paper*, (95-0722).

[119] Tyler, J. M. & Sofrin, T. G. (1962). *Axial flow compressor noise studies*. Technical report, SAE Technical Paper.

[120] Unruh, J. F. & Eversman, W. (1972). Utility of galerkin method for acoustic transmission in an attenuating duct. *Journal Of Sound And Vibration*, 23(2), 187–&.

[121] Verdon, J. M. (1992). Linearized unsteady aerodynamics for turbomachinery aeroelastic applications. *Journal de Physique III*, 2(4), 481–506.

[122] Verdon, J. M. (1993). Review of unsteady aerodynamic methods for turbomachinery aeroelastic and aeroacoustic applications. *AIAA journal*, 31(2), 235–250.

[123] Vilenski, G. G. & Rienstra, S. W. (2005). Acoustic modes in a ducted shear flow. *Proceedings of the 11th AIAA/CEAS Aeroacoustics Conference, Monterey, California, May 23-25*.

[124] Vilenski, G. G. & Rienstra, S. W. (2007a). Numerical study of acoustic modes in ducted shear flow. *Journal of Sound and Vibration*, 307(3-5), 610–626.

[125] Vilenski, G. G. & Rienstra, S. W. (2007b). On hydrodynamic and acoustic modes in a ducted shear flow with wall lining. *Journal of Fluid Mechanics*, 583, 45–70.

[126] Vo, P. T. & Eversman, W. (1978). A method of weighted residuals with trigonometric basis functions for sound transmission in circular ducts. *Journal of Sound and Vibration*, 56(2), 243–250.